

1995

Bubble and elutriation control in fluidized beds with electric fields

Jiun-Shen Wang
Iowa State University

Follow this and additional works at: <https://lib.dr.iastate.edu/rtd>

 Part of the [Chemical Engineering Commons](#), [Industrial Engineering Commons](#), and the [Mechanical Engineering Commons](#)

Recommended Citation

Wang, Jiun-Shen, "Bubble and elutriation control in fluidized beds with electric fields " (1995). *Retrospective Theses and Dissertations*. 10735.
<https://lib.dr.iastate.edu/rtd/10735>

This Dissertation is brought to you for free and open access by the Iowa State University Capstones, Theses and Dissertations at Iowa State University Digital Repository. It has been accepted for inclusion in Retrospective Theses and Dissertations by an authorized administrator of Iowa State University Digital Repository. For more information, please contact digirep@iastate.edu.

INFORMATION TO USERS

This manuscript has been reproduced from the microfilm master. UMI films the text directly from the original or copy submitted. Thus, some thesis and dissertation copies are in typewriter face, while others may be from any type of computer printer.

The quality of this reproduction is dependent upon the quality of the copy submitted. Broken or indistinct print, colored or poor quality illustrations and photographs, print bleedthrough, substandard margins, and improper alignment can adversely affect reproduction.

In the unlikely event that the author did not send UMI a complete manuscript and there are missing pages, these will be noted. Also, if unauthorized copyright material had to be removed, a note will indicate the deletion.

Oversize materials (e.g., maps, drawings, charts) are reproduced by sectioning the original, beginning at the upper left-hand corner and continuing from left to right in equal sections with small overlaps. Each original is also photographed in one exposure and is included in reduced form at the back of the book.

Photographs included in the original manuscript have been reproduced xerographically in this copy. Higher quality 6" x 9" black and white photographic prints are available for any photographs or illustrations appearing in this copy for an additional charge. Contact UMI directly to order.

UMI

**A Bell & Howell Information Company
300 North Zeeb Road, Ann Arbor, MI 48106-1346 USA
313/761-4700 800/521-0600**



**Bubble and elutriation control in fluidized beds
with electric fields**

by

Jiun-Shen Wang

A Dissertation Submitted to the
Graduate Faculty in Partial Fulfillment of the
Requirement for the Degree of
DOCTOR OF PHILOSOPHY

Department: Mechanical Engineering

Major: Mechanical Engineering

Approved:

Signature was redacted for privacy.

In Charge of Major Work

Signature was redacted for privacy.

For the Major Department

Signature was redacted for privacy.

For the Graduate College

Iowa State University
Ames, Iowa

1995

UMI Number: 9531802

UMI Microform 9531802

Copyright 1995, by UMI Company. All rights reserved.

**This microform edition is protected against unauthorized
copying under Title 17, United States Code.**

UMI

**300 North Zeeb Road
Ann Arbor, MI 48103**

TABLE OF CONTENTS

LIST OF TABLES	v
LIST OF FIGURES	vi
NOMENCLATURE	xiv
1. INTRODUCTION	1
1.1 Previous Study	3
1.1.1 Bubble control	3
1.1.2 Elutriation	8
1.2 Present Research	9
2. EXPERIMENT SETUP AND PROCEDURES	11
2.1 Generation and Measurement of Electric Fields	11
2.2 Measurement of Voidage of a Packed Bed	12
2.3 Bed Conductivity and Bed Expansion Measurement	14
2.3.1 Conductivity measurement	16
2.3.2 The expansion of the fluidized bed	17
2.4 Elutriation and Particle Charge Measurement	19
2.4.1 Elutriation constant and particle charge	19
2.4.2 Temperature effect on elutriation	21
2.4.3 Charge of elutriated fines	25

2.5 Yield Strength and Minimum Bubbling Velocity Measurement	25
2.5.1 Minimum bubbling velocity and pressure drop ...	25
2.5.2 The relative humidity effect	29
2.5.3 The effect of gas viscosity and particle diameter	31
2.6 Temperature Effect on the Bubble Control	32
3. RESULTS AND DISCUSSIONS	34
3.1 Bed Conductivity	34
3.2 Correlation for Bed Expansion with an Electric Field	39
3.2.1 Correlation with two-phase theory	47
3.2.2 Frequency effect	53
3.2.3 Relative humidity effect	57
3.2.4 Bed expansion and freezing	60
3.3 Elutriation	60
3.3.1 Beam attenuation theory	60
3.3.2 Elutriation constant with an electric field ...	64
3.3.3 Particle charge	78
3.4 Mapping the Electric Field	80
4. THEORETICAL STUDIES	84
4.1 Extension of Davidson Model (DC)	90
4.2 AC Electric Field Model	101

4.3 Stability Analysis	107
4.4 Scale-up Analysis	136
5. CONCLUSIONS	139
BIBLIOGRAPHY	142
ACKNOWLEDGMENTS	146
APPENDIX A: ERROR ANALYSIS	147
APPENDIX B: PERTURBATION ANALYSIS	154
APPENDIX C: SCALE-UP ANALYSIS	158
APPENDIX D: PROPERTIES OF MATERIALS	160
APPENDIX E: CALIBRATION OF ROTAMETERS	168
APPENDIX F: PROGRAM AND EXAMPLE DATA	180

LIST OF TABLES

Table 3.1: Constants of $C(U)$, a , and b for Eqn.3.6	52
Table 3.2: Constants in Richardson-Zaki equation for glass beads of various diameters	52
Table 3.3: Elutriation constant at different temperatures with an electric field	78
Table 4.1: Various particle and interparticle force equations	85
Table 4.2: Summary results for bed elasticity modulus, bed resistivity, and Richardson-Zaki fit for different materials with Argon, 24°C	121
Table A.1: Summary results of error analysis	153
Table D.1: Properties of materials used in the experiment	162
Table D.2: The properties of different materials	163

LIST OF FIGURES

Figure 2.1:	Pyrex fluidized bed for elutriation constant measurement	13
Figure 2.2:	Copper fluidized bed for measurement of bed electrical conductivity and bubble control, placed in oven	15
Figure 2.3:	Particle size distribution of sand fines as Waddel diameter fit to a Rossin-Rammler-Bennett size distribution	22
Figure 2.4:	Brass fluidized bed with natural gas burning for measurement of high temperature elutriation constant	23
Figure 2.5:	Faraday cage for particle charge measurement	26
Figure 2.6:	Pyrex fluidized bed for measurement of bubble control and bed elasticity modulus	27
Figure 2.7:	Instruments set up for controlling relative humidity	30
Figure 2.8:	Quartz fluidized bed with electrical heating wire for measurement of the high temperature bubble control, bed resistivity and bed elasticity modulus	33
Figure 3.1:	Log-log plot of current density versus electric field strength showing linearity with effect of temperature	35
Figure 3.2:	Log-log plot of current density versus temperature showing (approximately) linearity with effect of electric field strength (potential)	36

Figure 3.3:	Reduced data, current density, electric field strength, and temperature with least squares fit of Eqn.3.2	38
Figure 3.4:	Packed bed, current density of sand with fines at various temperature	40
Figure 3.5:	Packed bed, current density of sand at various temperature with 15 minutes of fluidization to reduce fines	41
Figure 3.6:	Sample of sand particles, (a) before, (b) after running the fluidized bed for 15 minutes (SEM, Kevex, automated image analyzer), x200	42
Figure 3.7:	Bed voidage with superficial velocity, increased effect of electric field strength. 44-74 μ m with air, AC-3Hz, peak-to-peak (p-p), R.H.=9.8%	44
Figure 3.8:	Minimum superficial velocity for onset of bubbling with p-p field strength, effect of temperature, 44-74 μ m with Air	45
Figure 3.9:	Bed voidage with superficial velocity, increased temperature at various electric field strength, 44-74 μ m with air	46
Figure 3.10:	Bed expansion with electric field strength and superficial velocity, experimental data and least squares fit. 74-144 μ m with air	49
Figure 3.11:	Summary data for bed expansion and electric field strength for various particle size ...	54
Figure 3.12:	Summary data for superficial velocity and particle diameter (median) for various electric field strength	55
Figure 3.13:	Bed expansion with frequency, 74-144 μ m, AC-5kV p-p, 24 $^{\circ}$ C, air	56

Figure 3.14: Freezing bed with increased relative humidity, 44 μ m n.w.p. glass beads, AC-3Hz-3kV, p-p ...	58
Figure 3.15: Freezing bed with increased relative humidity, 44 μ m w.p. glass beads, AC-3Hz-3kV, p-p	59
Figure 3.16: Frequency effect on bed expansion/contraction at various electric field strength, FCC 2-A with Argon, $U/U_{mf}=2.24$, 24 $^{\circ}$ C, AC p-p	61
Figure 3.17: Size distribution of elutriated sand fines at various superficial velocity	65
Figure 3.18: Comparison of elutriation constant calculated using correlation from Merrik & Highley and Geldart with result from Laser-beam method .	66
Figure 3.19: Elutriation constant at different electrode height (inserted from distributor), $U/U_{mf}=2.24$	67
Figure 3.20: Elutriation constant of DC 3 kV and AC p-p, 3 Hz, 3 kV electric field $U/U_{mf}=2.24$	69
Figure 3.21: Elutriation constant of various velocity ratio with and without electric field (3 Hz, 3 kV, p-p)	70
Figure 3.22: Elutriation constant versus frequency, AC-3kV peak-to-peak, $U/U_{mb}=1.5$, sand, 24 $^{\circ}$ C, $U/U_{mf}=2.24$	71
Figure 3.23: Particle concentration in freeboard with time, slope is a measure of elutriation constant $U/U_{mf}=2.24$	73
Figure 3.24: Particle concentration in freeboard with time at various temperature. DC-3kV, $U/U_{mf}=2.24$..	74
Figure 3.25: Particle concentration in freeboard with time at various temperature. 0kV, $U/U_{mf}=2.24$	75

Figure 3.26: Particle concentration in freeboard with time at various temperature. AC-3Hz-3kV, $U/U_{mf}=2.24$	76
Figure 3.27: Particle concentration in freeboard with electric field momentarily off and momentarily on, 0 kV and 3 kV, AC, 3Hz, p-p, $U/U_{mf}=2.24$.	77
Figure 3.28: Charged elutriated fines with and without electric fields, $U/U_{mf}=2.24$, $d_p= 8.66 \mu\text{m}$	79
Figure 3.29: Bubble and no bubble zone for the bed with electric field, 44 μm n.w.p. microbeads glass AC 20 Hz, half of p-p, Ar	81
Figure 3.30: Map of electrofluidization with Geldart A powders	82
Figure 4.1: Comparison of various particle-particle (wall) in fluidized bed versus particle diameter for effect contact separation $2.23 \times 10^{-10} \text{m}$	87
Figure 4.2: Comparison of various particle-particle (wall) in fluidized bed versus particle diameter for effect contact separation $2.23 \times 10^{-9} \text{m}$	88
Figure 4.3: Contour plot of constant pressure gradient lines showing maximum pressure gradient on spherical bubble of unit radius	93
Figure 4.4: Pressure gradient on surface of bubble of unit radius (with the vertical z axis)	94
Figure 4.5: Vector field plot of current density magnitude and electric field strength near bubble ($\theta=0$), Current density inside bubble = 0	96
Figure 4.6: Lines of constant ψ showing current path and direction of electric field past bubble of unit radius (largest current concentration at the top of the bubble)	97

Figure 4.7:	Equivalent circuit for particles with mutual capacitance, including contact resistance and surface conductivity	102
Figure 4.8:	Decrease in particle-particle force with increasing frequency of electric field	105
Figure 4.9:	Freezing zone of expanded bed for frequency effect on the FCC 2-A with Argon (Ar) and $U/U_{mf}=2.24$	106
Figure 4.10:	Conception of particle contacts during fluidization	109
Figure 4.11:	Comparison of constant for 44 μ m n.w.p. glass particles with N ₂ using R&Z and K&C approaches	111
Figure 4.12:	Experimental and theoretical Y_{mb} vs. E (K&C). 44 μ m, n.w.p. glass beads with Ar and AC-20Hz, half p-p electric field	113
Figure 4.13:	Experimental and theoretical Y_{mb} vs. E (K&C). 44 μ m n.w.p. glass beads with N ₂ and AC-3Hz, half p-p electric field	114
Figure 4.14:	Experimental and theoretical Y_{mb} vs. E (R&Z). 44 μ m n.w.p. glass beads with Ar and AC-20Hz, half p-p electric field	116
Figure 4.15:	Experimental and theoretical Y_{mb} vs. E (R&Z). FCC 1-B (Kaolin clay) with Ar and AC-1Hz, half p-p electric field	117
Figure 4.16:	Experimental and theoretical Y_{mb} vs. E (R&Z). FCC 1-A (Zeolitic, spent) with Ar and AC-1.5Hz, half p-p electric field	118
Figure 4.17:	Experimental and theoretical Y_{mb} vs. E (R&Z). FCC 2-A (Zeolitic, fresh) with Ar and AC-1Hz, half p-p electric field	119

- Figure 4.18: Experimental and theoretical Y_{mb} vs. E (R&Z).
44 μ m n.w.p. glass beads with Air and AC-3Hz,
half p-p electric field 122
- Figure 4.19: Experimental and theoretical Y_{mb} vs. E (R&Z).
44 μ m n.w.p. glass beads with N_2 and AC-3Hz, half
p-p electric field 123
- Figure 4.20: Experimental and theoretical Y_{mb} vs. E (R&Z).
44 μ m n.w.p. glass beads with CO_2 and AC-1.5Hz,
half p-p electric field 124
- Figure 4.21: Y_{mb} vs. voidage at U_{mb} of different gas, 44.1
 μ m, n.w.p. Microbeads glass, 24 $^{\circ}C$, 0 kV ... 125
- Figure 4.22: U_{mb} vs. gas viscosity, 44.1 μ m, n.w.p.
Microbeads glass, 24 $^{\circ}C$, 0 kV 126
- Figure 4.23: ϵ_{mb} vs. gas viscosity 44.1 μ m, n.w.p. Microbeads
glass, 24 $^{\circ}C$, 0 kV 127
- Figure 4.24: U_{mb} vs. particle diameters, n.w.p. Microbeads
glass, 24 $^{\circ}C$, 0 kV R.H.=9.8%, Air 128.
- Figure 4.25: Y_{mb} vs. particle diameter, n.w.p. Microbeads
glass, 24 $^{\circ}C$, 0 kV, R.H.=9.8%, Air 129
- Figure 4.26: Experimental and theoretical bed elasticity
modulus for various frequency at constant
electric field strength using K&C relation.
44 μ m n.w.p. glass beads with N_2 131
- Figure 4.27: Experimental and theoretical bed elasticity
modulus for various frequency at constant
electric field strength using R&Z relation.
44 μ m n.w.p. glass beads with N_2 132
- Figure 4.28: Y_{mb} with and without electric field (AC, 4. kV,
p-p) vs. R.H., n.w.p. 44 μ m Microbeads glass,
24 $^{\circ}C$, Air 133

Figure 4.29: Voidage at U_{mb} vs. temperature, FCC (2-A), Ar, 0 kV	134
Figure 4.30: U_{mb} vs. temperature, FCC (2-A), Ar, 0 kV	135
Figure D.1: U vs. pressure drop of the fluidized bed for determining the U_{mf}	164
Figure D.2: (a). Picture of glass beads (marked as 63-74 μ m) taken from SEM, Kevex, automated image analyzer, x100 (b). Picture of sand fines, x200	165
Figure D.3: (a). Picture of FCC 1-B (Kaolin clay) taken from SEM, Kevex, automated image analyzer, x50 (b). Picture of FCC 1-A (Zeolitic, spent), x100 .	166
Figure D.4: (a). Picture of FCC 2-A (Zeolitic, fresh) taken from SEM, Kevex, automated image analyzer, x100 (b). Picture of FCC 3-A (aluminum oxide), x500	167
Figure E.1: Calibration of rotameter SA1 with Air, N ₂ , and CO ₂	169
Figure E.2: Calibration of rotameter SA2 with Air, N ₂ , and CO ₂	170
Figure E.3: Calibration of rotameter SA3 with Air, N ₂ , and CO ₂	171
Figure E.4: Calibration of rotameter LabCrest 450-700 with Air	172
Figure E.5: Calibration of rotameter Devco 250-8 with Air	173
Figure E.6: Calibration of rotameter SA3 with CO ₂	174
Figure E.7: Pressure drop across distributor for N ₂ at 24 °C, 1 atm	175

Figure E.8:	Pressure drop across distributor for CO ₂ at 24 °C, 1 atm	176
Figure E.9:	Pressure drop across distributor for Air at 24 °C, 1 atm	177
Figure E.10:	Pressure drop across distributor for Ar at 24 °C, 1 atm	178
Figure E.11:	Pressure drop across rotameter SA3 for various gases at 24 °C, 1 atm	179

NOMENCLATURE

A_c	cross section area of fluidized bed, m^2
$C(U)$	non-dimensional correlation factor
E	electrical field strength, V/m (or kV/m)
E_o	reference electrical field strength
E_{mb}	electric field strength of minimum bubbling
E_{max}	breakdown electrical field strength between particle contact
F_{J-DC}	electrical force due to the DC current effect, N
F	interparticle force, N
H	bed height, m
H_{mf}	bed height of minimum fluidization
H_{mb}	bed height of minimum bubbling
I	intensity of laser beam reading, V
I_o	reference laser beam reading
J	current density, A/m^2
K	constant
K_a	permittivity constant, 8.85×10^{-12} F/m
K_b	ratio of permittivity
K_c	constant
K_i	elutriation constant, s^{-1}

M	mass of particles in the bed
M_i	mass of particle size i , kg
M_{i0}	total mass of fine of size I elutriated in an infinite time
P	pressure, N/m^2
ΔP	pressure across the fluidized bed
R_c	particle contact resistance
R_s	surface contact resistance
R.H.	relative humidity, %
U	superficial velocity, m/s
U_b	bubble rise velocity
U_{mf}	minimum fluidized velocity
U_{mb}	minimum bubbling velocity
$U_{mb,E}$	minimum bubbling velocity under electric field
U_o	gas velocity
U_s	superficial gas velocity
T	temperature, $^{\circ}C$
Y	elasticity of the fluidized bed, N/m^2
Y_{mb}	elasticity of the bed under minimum bubbling
Y_{vdw}	elasticity due to van der Walls force
$Y_{vdw,el}$	elasticity due to van der walls force with electrical field applied on the bed

c	constant
d	particle diameter, μm
d_p	particle diameter
g	acceleration of gravity, 9.81 m/s^2
k	constant from the Richardson-Zaki relationship
n	constant from the Richardson-Zaki relationship
n_i	particle number density of size I
p_b	pressure inside the bubble, N/m^2
r	radius coordinate
r_b	bubble radius, m
t	time, s
u	velocity of fluid phase, m/s
u_b	relative fluid/particle interstitial fluid velocity far from the bubble, m/s
v	velocity of disperse (or particle) phase, m/s
x	distance between two particles, m

Greek

α	resistivity of the bed, ohm
$\beta_o(\varepsilon)$	permeability constant
ε	voidage of the fluidized bed

ϵ_b	voidage of bubbling phase
$\epsilon_{em,o}$	permittivity of free space, 8.854×10^{-12} F/m
ϵ_{mf}	voidage of the fluidized bed under minimum fluidization
ϵ_{mb}	voidage of the fluidized bed under minimum bubbling
ϵ_{packed}	voidage of the packed bed
ϕ	electrical field potential, V
ϕ_s	particle sphericity
μ	viscosity, N.s/m ²
γ	constant
ξ	cumulative fraction of all particles up to diameter d
ζ	conductivity of the fluidized bed, Ω -m
ρ_f	fluid density, kg/m ³
ρ_p	particle density, kg/m ³
σ	stress of the fluidized bed, N/m ²
τ_c	time constant for particle contact resistance
τ_s	time constant for surface contact resistance
ω	angular velocity, radian/s

1. INTRODUCTION

Gas fluidization is a phenomena in which solid particles are kept in a flotation state by an upward flowing gas. At a low superficial gas velocity, gas passes through the void spaces between the particles. In this condition the bed essentially remains fixed. As the gas velocity is increased, the bed expands slightly. At a critical velocity, the solid particles become suspended by the upwarding flowing gas. This state is known as minimum fluidization. The corresponding velocity is the minimum fluidization velocity, or incipient velocity. In this condition, the hydrodynamic drag force is exactly balanced by the gravitational force on the particle. The pressure drop through any section of the fluidized bed equals the weight of the solid particles and the gas divided by the cross-sectional area of the bed.

As the gas velocity is increased above the minimum fluidization velocity, bubbles begin to form in the bed. The velocity at which bubbles first appear is called the minimum bubbling velocity. The fluidized bed now consists of two regions. One region contains bubbles, while the other is a

mixture of fluid and particles in a state of minimum fluidization. Further increases in the superficial velocity move the fluidized bed into a fast transporting regime where slugs dominate in the bed. Finally, once the superficial velocity exceeds the terminal velocity of the largest particle in the fluidized bed all the particles in the fluidized bed would be carried out.

Bubbles are formed by the gas in the fluidized bed. After the gas velocity reaches the minimum bubbling velocity, any extra gas forms bubbles. Bubbles grow, diminish or coalesce with other bubbles. They move from the bottom of the bed to the top. Particles are carried and released by bubbles. This behavior creates a fast and intimate mixture between the particles. When bubbles reach the free surface of the bed, they erupt and throw particles into the freeboard. Smaller particles are carried out by the gas, while large particles drop back into the bed. This carry-out behavior is called elutriation. When the superficial velocity of the fluidized bed exceeds the terminal velocity of a particle, the particle is elutriated out of the fluidized bed.

Bubbles by-pass flow and cause elutriation. In order to improve the fluidized bed efficiency for industrial applications, it is desirable to eliminate the bubble formation and thereby reduce the elutriation of fines. Both electric and magnetic field can be applied to fluidized beds to reduce the bubble formation.

1.1 Previous Study

Fluidized beds stabilized by an electrical field are also called electro-fluidized beds. The electrical field may be parallel or vertical to the direction of flowing gas. The electrical field can either be a direct current (DC) or an alternating current (AC). The resulting electric force acting on the particles alter the dynamics of the fluidized bed.

1.1.1 Bubble control

The formation of bubbles in a fluidized bed are determined by properties of both the particles and the fluid (Geldart, 1986). Due to gas by-passing, a bubbling condition can be undesirable in the application of fluidized beds. Use

of an electric field has been studied as alternative method for the control of the formation of bubbles.

Katz and Sears (1969) reported 100% bed expansion without diffusive particle motion or bubble formation, using gel particles with a DC electric field. Johnson and Melcher (1975) tested cross-flow and co-flow DC sand electrofluidized beds. They reported that bed expansion was possible. However, in the co-flow condition, the electric field could easily freeze the bed. Dietz and Melcher (1978a) investigated interparticle electrical forces in packed and fluidized beds with a DC electric field. It was reported that the electric force required to gain bubble control was a function of the applied electric field strength. Dietz and Melcher (1978b) proposed a force equation using a momentum analysis for a model which consisted of two particles inside an electric field.

In the case of an AC electric field, Dietz (1977) studied the fields and forces on a microscope sphere above a ground plane in a sinusoidal varying electric field. He found that there were three regimes: conduction, polarization and intermediate. He also showed that the electric force is a

function of frequency. Moissis and Zahn (1986) conducted a theoretical approach to an electrofluidized bed that responded to a small AC electric field of excitation. It was concluded that bed expansion would occur in the co-flow condition. However, they reported no effect on the fluidized bed for the cross flow condition.

A good survey of work in electrofluidized beds was given by Colver (1979). According to Colver, stabilization was best achieved with small particles, diameters smaller than 100 μm , and a horizontally directed alternating electric field. He also showed the superiority of an AC electric field over a DC on a fluidized bed in terms of bubble control. Colver and Basshart (1980) reported an up to 30% expansion in bed height without bubbling for a bed of 60 μm particles in a field alternating at 20 Hz and with an rms. field strength of 9.05 kilo-volt per centimeter (kV/cm). It was also reported that high relative humidity could dramatically increase the conductivity and reduce the effect of bubble control. Colver (1976) found that the required electric field strengths for bubble control were of the order kV/cm. This electric field was found to be effective on a variety of particulate

materials, including both good conductors and semi-insulators. Donahoe and Colver (1984) conducted experiments on injecting a single bubble into an all electrofluidized bed. It was determined that applying an electric field changed the bubble volume and rise velocity. In the DC case, the bubble could easily be immobilized by the field. Also, the required electric field strength to gain bubble control was higher for the AC electric field than for the DC electric field, due to charge relaxation.

To understand the mechanism of bubble control, the interparticle and hydrodynamic forces on particles must be investigated. Colver (1976) first conducted a series of experiments to understand the dynamics and stationary charging of heavy metallic and dielectric particles against a conducting wall in the presence of a DC applied electric field. It was reported that the charge had the form $Q=4\pi\epsilon_{em/o}a^2KE$, where $K=1.64$. Colver (1980) investigated different interparticle forces, such as van der Waals, capillary, electrostatic contact, dipole, and electrostatic. Different charge relaxation time constants were also determined for 62 μm glass beads at 30% relative humidity.

Colver (1983) also proposed equations for estimating different charge relaxation time constants. From this time constant, which was relative to the bed surface, the void fraction of the electrofluidized bed could be predicted.

Rietema (1991) proposed a criteria for the minimum bubbling velocity using the perturbation analysis for the bed elasticity modulus. Xie and Geldart (1992, 1993) examined the effect of van der Waals force on the fluidized bed without an electric field. It was reported that the voidage of minimum bubbling decreased with the increasing particle diameter and temperature.

Gidaspow (1994) derived a relationship for the particle drag force from the kinetic energy dissipation analysis. He showed the same function as the Ergun equation.

The scale-up parameters of the fluidized bed were studied by Glicksman (Glicksman, 1986). By adding an electric field, new parameters must be found in order to scale up the electro-fluidized bed.

1.1.2 Elutriation

Elutriation is defined as a loss of fines from the fluidized bed and is due to the bursting of bubbles on the surface of the fluidized bed. The elutriation constant is a function of the terminal velocity of the particle, minimum fluidization velocity, superficial velocity and density of the particles and fluid. Several correlations have been proposed for estimating the elutriation constant (Kunii and Levenspiel, 1991). The elutriation constant can be derived from batch-operation modes. Applying an electric field to the fluidized bed offers an alternative control parameter to elutriation, since it controls the formation of bubbles. Zahedi and Melcher (1975) described a practical development in control of oil ash, asphalt fume and coal ash in flue gas, using the electric field on fluidized beds.

A creative method for measuring the elutriation constant involves using a laser beam and the Lambert-Beer Law as given conducted by Liu and Colver (1991). The method measures the attenuation rate of the intensity of the laser beam from which the particle concentration on the top of the cross-

section of the pipe can be calculated. However, the method does not apply to fluidized beds directly.

1.2 Present Research

The objective of the current research was to gain an understanding of the control mechanisms of the fluidized bed with AC and DC electric fields. As a control parameter, the electric field changed the mode of fluidized bed.

Several fluidized beds were assembled to determine the influence of different parameters. A quartz bed with an electrical heater was used to study the temperature effect. A parallel Pyrex bed was used to study the effect of different relative humidity, fluid viscosity, particle diameter, electric field strength, and field frequency. A circular copper bed and a circular Pyrex bed with cross-flow electrodes were used to test elutriation control. The bed materials were Geldart A powders.

To understand the mechanism of bubble formation and elutriation control, the interparticle forces acting on the particle were also studied.

To obtain an understanding of how electrical fields affect bubble formation, mechanism of elutriation control, minimum bubbling velocity and the elutriation rate, various correlations were derived from experimental data and compared with results based on a theoretical approach.

Scale-up parameters were also observed in order to study the possibility of industrial applications on a large scale.

2. EXPERIMENT SETUP AND PROCEDURES

The experimental setup includes several fluidized beds, a data acquisition system, a laser emitter-receiver system, an electric field supply system and an air flow supply and regulation system. The detailed description of the experimental procedure will be in the following sections.

2.1 Generation and Measurement of Electric Fields

AC or DC electric fields were generated using a function generator (Wavetek 193) with a AC power amplifier (Trek 609A 1:1000 Volt (V), Trek 620A 1:2000 V) or a DC power supply (Del Electrostatics DC 1:15000 V), respectively. The AC voltage signal could be sinusoidal, square, or triangular in wave form. The electric field was measured using a high voltage voltmeter (Sensitive Research Electrostatic Voltmeter, Model: ESH 0-50000 V). The voltmeter displayed a root-mean-square value (rms.) of the AC electric voltage. A safety resistor of 93 mega-ohms was placed between the output of power supply (or amplifier) and the fluidized bed to protect system instruments from spark surge. The resistor

would reduce transient currents generated when an electric breakdown occurred. When using an AC electric field, an oscilloscope (HP 1222A) and a high voltage probe (Keithly model 2316 1000:1) could be used to pick up the voltage signal across the fluidized bed. Fig. 2.1 showed the voltage supply and measurement assembly (lower left hand corner). The frequency could be as low as 0.01 Hertz (Hz), and as high as several thousand Hz; however, a drop off in voltage occurred above a few hundred Hz. The input voltage of the AC amplifier varied from 0 to 10 V. Therefore, the output of the amplifier was variable over the range of 0 to 10 kilo-volt (kV).

2.2 Measurement of Voidage of a Packed Bed

The voidage of a packed bed of powder was measured using a liquid displacement method. Initially, a liquid 1-1-1 trichro-ethylene was poured into a 10 milli-liter graduated cylinder until a desired liquid volume (V_1) was achieved. After measuring the mass of the powder with an electronic scale, the powder was poured into the graduated cylinder containing the liquid. Once the powder had settled, the total volume of the liquid plused powder (V_{1+s}), and the volume of

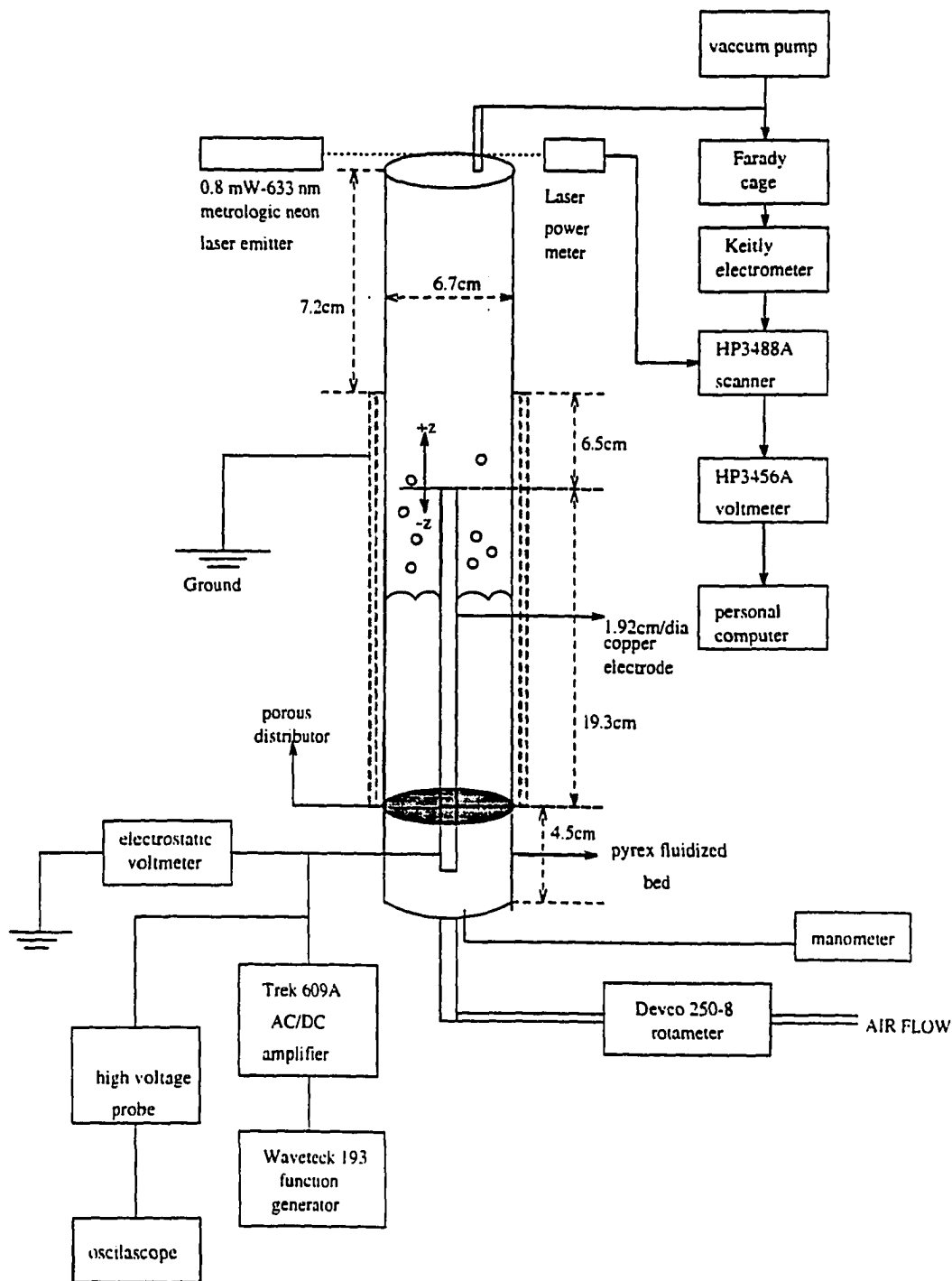


Figure 2.1 Pyrex fluidized bed for elutriation constant measurement

the powder mixed with the liquid (V_s), were recorded. The volume of the powder without the liquid was determined by the following equation:

$$V_{\text{powder}} = V_{s-l} - V_l \quad (2.1)$$

Thus, the voidage of the packed bed of powder was calculated as

$$\epsilon_{\text{packed}} = 1 - \frac{V_{\text{powder}}}{V_s} \quad (2.2)$$

The term ϵ_{packed} was usually referred to be ϵ_{mf} (voidage at minimum fluidization) in the fluidized bed. The density of the powder could be calculated by dividing the mass of the powder by the volume of the powder V_{powder} .

2.3 Bed Conductivity and Bed Expansion Measurement

Bed conductivity and bed expansion were investigated by using a parallel copper plate fluidized bed as shown in Fig.2.2. The base of the fluidized bed was Teflon. The bed consisted of two parallel copper plates glued to two quartz glass plates using a high temperature ceramic glue. The height of the bed was 26.5 cm, the width was 1.6 cm, and the length was 7.2 cm. For high temperature experiments (up to

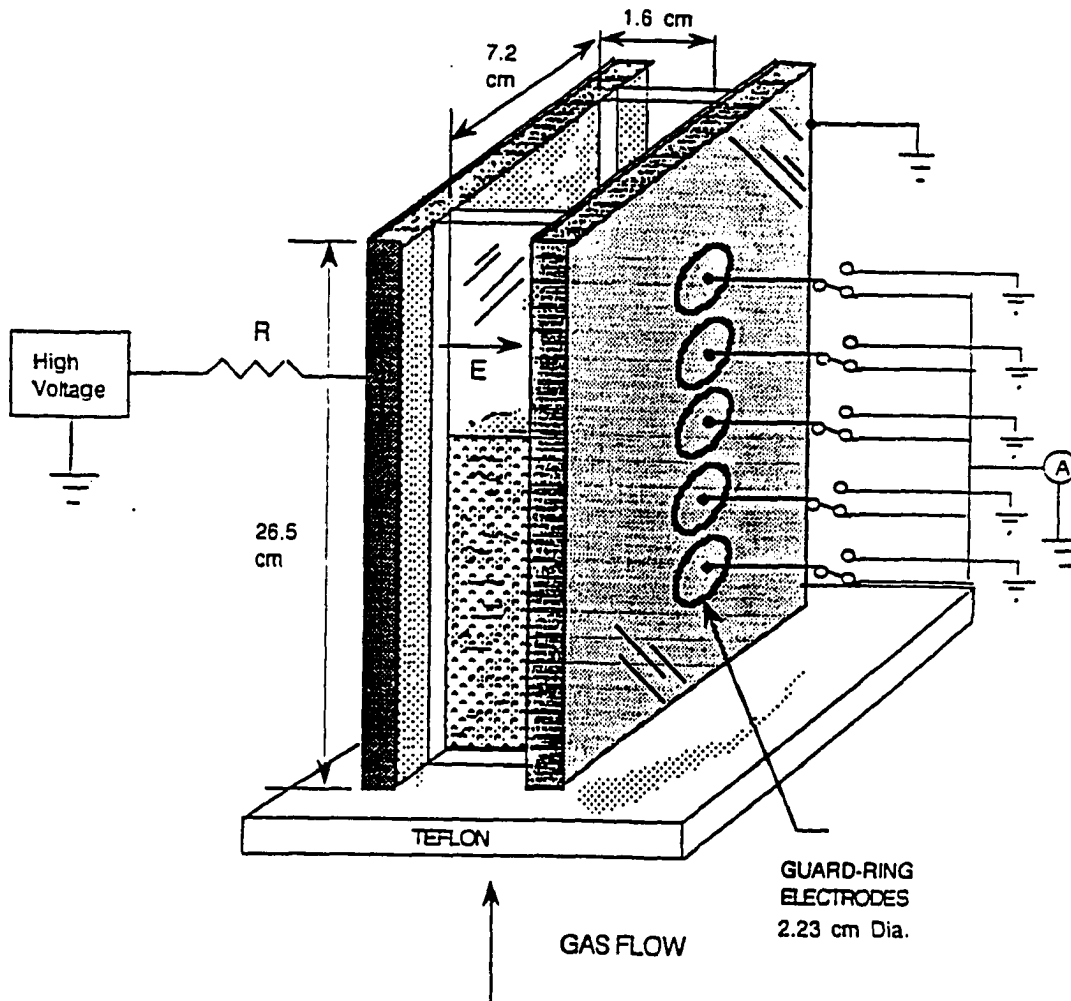


Figure 2.2 Copper fluidized bed for measurement of bed electrical conductivity and bubble control, placed in oven

200 °C), the whole bed could be placed inside an oven (Fisher isotemp model 176). The power supply used to generate the electric field was connected to one of the copper plates with a high temperature electric wire which was covered by a layer of Teflon. The other copper plate was grounded. Air flowed into the bottom of the bed through two copper tubes. The air flow rate was regulated by a rotameter (Gilmont B5284), which was calibrated using a wet testmeter (GCA Precision Scientific). The current and resistance of the powders in the packed or fluidized bed were measured by an electrometer (Keithly 602 Solid State Electrometer).

2.3.1 Conductivity measurement

The conductivity of the fluidized bed was studied using the following procedures: Water-proof (w.p.) Microbeads glass particles with a diameter of 44 to 74 micro meter (μm) were baked at 150 °C in a oven for half an hour. The particles were then allowed to cool down to room temperature, after which they were placed in the bed. It, too, cooled down to room temperature. Air was supplied to the bed at a constant rate of approximately 0.03 cm/sec. The relative humidity

(R.H.) of the bed was controlled by the R.H. of the supplied air. As long as the velocity of the air which flowed into the bed was much less than U_{mf} (in this experiment 0.636 cm/s), the bed expansion was negligible and the R.H. of the fluidized bed was approximately that of the flowing air. An electric field was applied to the fluidized bed and gradually increased. The current was read from the electrometer. Also, the resistance of the fluidized bed was taken from the electrometer. The procedure was then repeated for various oven temperatures. A plot of current density verses (vs.) electrical field strength was then obtained.

2.3.2 The expansion of the fluidized bed

This experiment was conducted at room temperature with 74-144 μm and 44-74 μm w.p. Microbeads glass powder for two different tests. In the first test, an electric field was applied to the fluidized bed. The superficial velocity was then gradually increased until bubbles formed and the bed height no longer increased. The bed height and pressure drop across the bed were recorded for each specific velocity. In the second test, the velocity was fixed above the U_{mb} . The

electric field was then gradually increased until the fluidized bed was frozen by the electric field. The bed height and pressure drop across the bed were recorded for each specific applied electric voltage, such as 0, 1, 2, 3, 4, 5, root-mean-square (rms.) kV.

The frequency effect was studied by applying a 0.3 Hz to 100 Hz AC electric field to the fluidized bed at room temperature. The voltage was 5 kV peak-to-peak (p-p). The particle diameter was 74-144 μm and the R.H. was 10%. The air velocity was gradually increased and the maximum bed height was recorded.

The effect of particle diameter was also studied by keeping the electric field and R.H. constant. Non-water-proof (n.w.p.) Microbeads glass powders with different ranges of diameters were used (see Table D.2). The electric field was 3 kV rms. and the frequency was 3 Hz. The R.H. was kept constant at 10%. The superficial velocity was gradually increased and the bed height and pressure drop were recorded. If the superficial velocity changed during the experiment, the bed was tapped, using a rod, to eliminate the wall effect.

The temperature effect on U_{mb} was studied using the 44-74 μm w.p. Microbeads glass powder. With the temperature fixed, the superficial velocity was gradually increased until U_{mb} was found.

2.4 Elutriation and Particle Charge Measurement

2.4.1 Elutriation constant and particle charge

Fig.2.1 illustrates the experimental setup used to determine the elutriation constant and net charge of the particles. The cylindrical fluidized bed was constructed from Pyrex. The inner diameter of the bed was 6.7 cm and the height was 33 cm. A wire screen was connected to ground and a 1.9 cm diameter copper electrode was assembled on the distributor of the fluidized bed to eliminate a possible electric precipitation effect. In the case of an AC electric field, the wire screen could be inside or outside the fluidized bed, and in the case of a DC electric field, the wire screen had to be inside. The laser beam system, which was formed by an emitter (Metrologic Neon 0.8 mW-633 nm) and a laser power meter, was used to measure the intensity of the

laser beam after passing through the top of the fluidized bed. By using the Lambert-Beer law and by assuming the elutriated particles were well distributed across the bed, the elutriation constant could be calculated. The Faraday Cage system was used to measure the particle charge. It consisted of a vacuum pump, a Faraday cage, and an electrometer. The electrometer gave the charge of the Faraday cage by the captured elutriated particles. A scanner (HP3488), a voltmeter (HP346A) and a personal computer made up the data acquisition system. This system read the laser intensity from the laser power meter and the charge from the electrometer.

For this experiment, ordinary sand was used as the bed material, since it was similar to the bed material of the coal burning fluidized beds. The data was taken under different air velocities and electric field strengths. The sand was baked at 200 °C in the oven for approximately half an hour, then allowed to cool down to room temperature to obtain a constant relative humidity. A rotameter (Devco 250-8) was used to control the gas flow rate into the fluidized bed. In each run, the sequence of the procedure was the

following: (1) a constant mass of sand of 387 grams (gm.) was obtained. (2) the sand into the bed was poured. (3) the pre-set electric field was turned on. (4) the vacuum pump was turned on; and (5) the gas flow was opened and the data acquisition computer was started. When the pre-set time of 180 second was reached, the air flow was closed, and both the vacuum pump and the electric field were turned off. The U_{mf} of the sand was found by plotting the pressure drop vs. superficial velocity. The average particle diameter was calculated from the mass distribution of the different particle diameter range, which were determined by sieving out the sand. The diameter of elutriated fines was calculated using an electronic microscope and was approximately $8.66\mu\text{m}$ (Waddel diameter, Appendix D). Fig.2.3 shows the plot of the particle diameter distribution of fines which were elutriated from the sand fluidized bed.

2.4.2 Temperature effect on elutriation

The effect of temperature on elutriation was determined using a 9.8 cm inner diameter cylindrical copper fluidized bed, as shown in Fig.2.4. The electrode was made from 2.5 cm

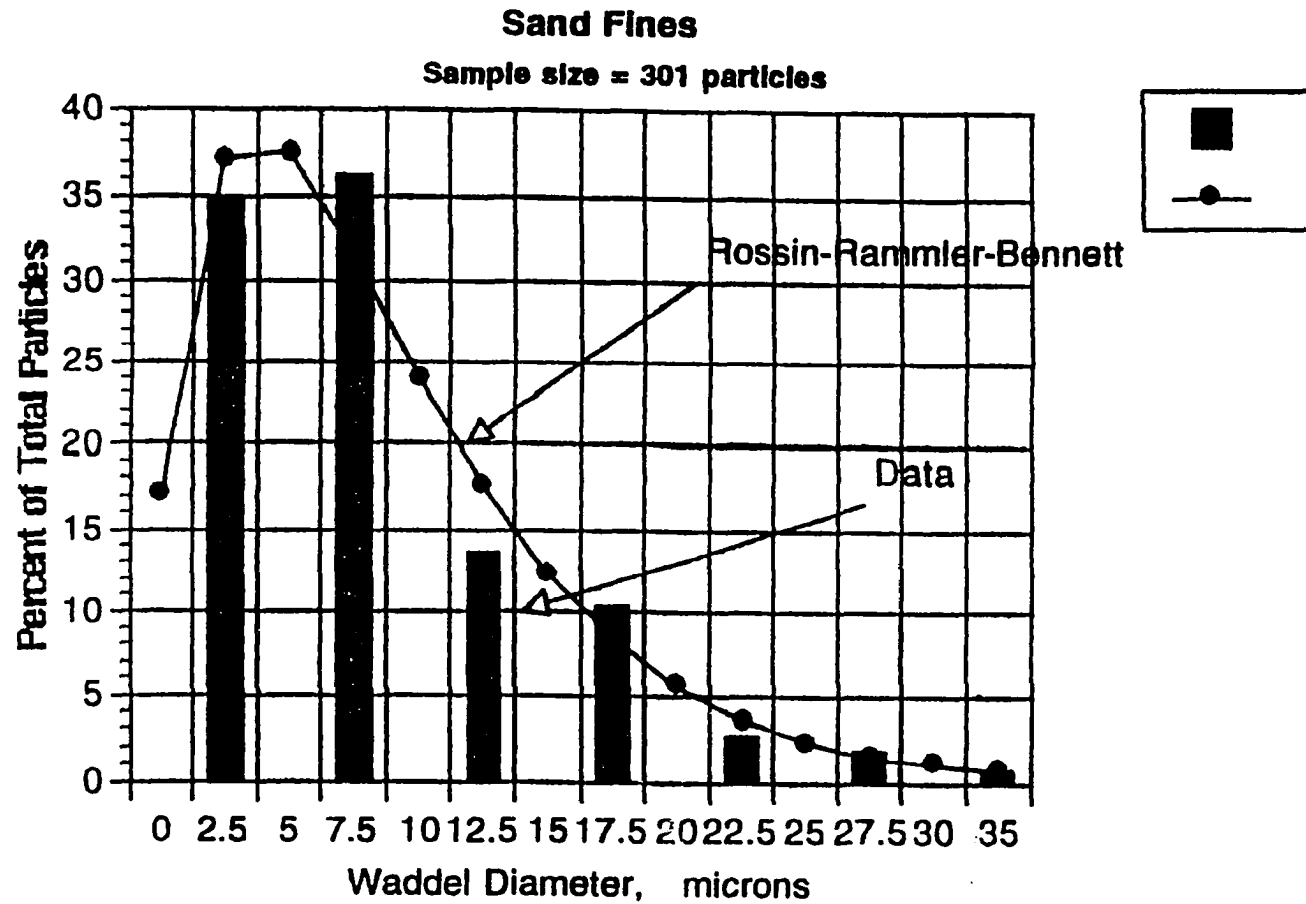


Figure 2.3 Particle size distribution of sand fines as Waddel diameter fit to a Rossin-Rammler-Bennett size distribution

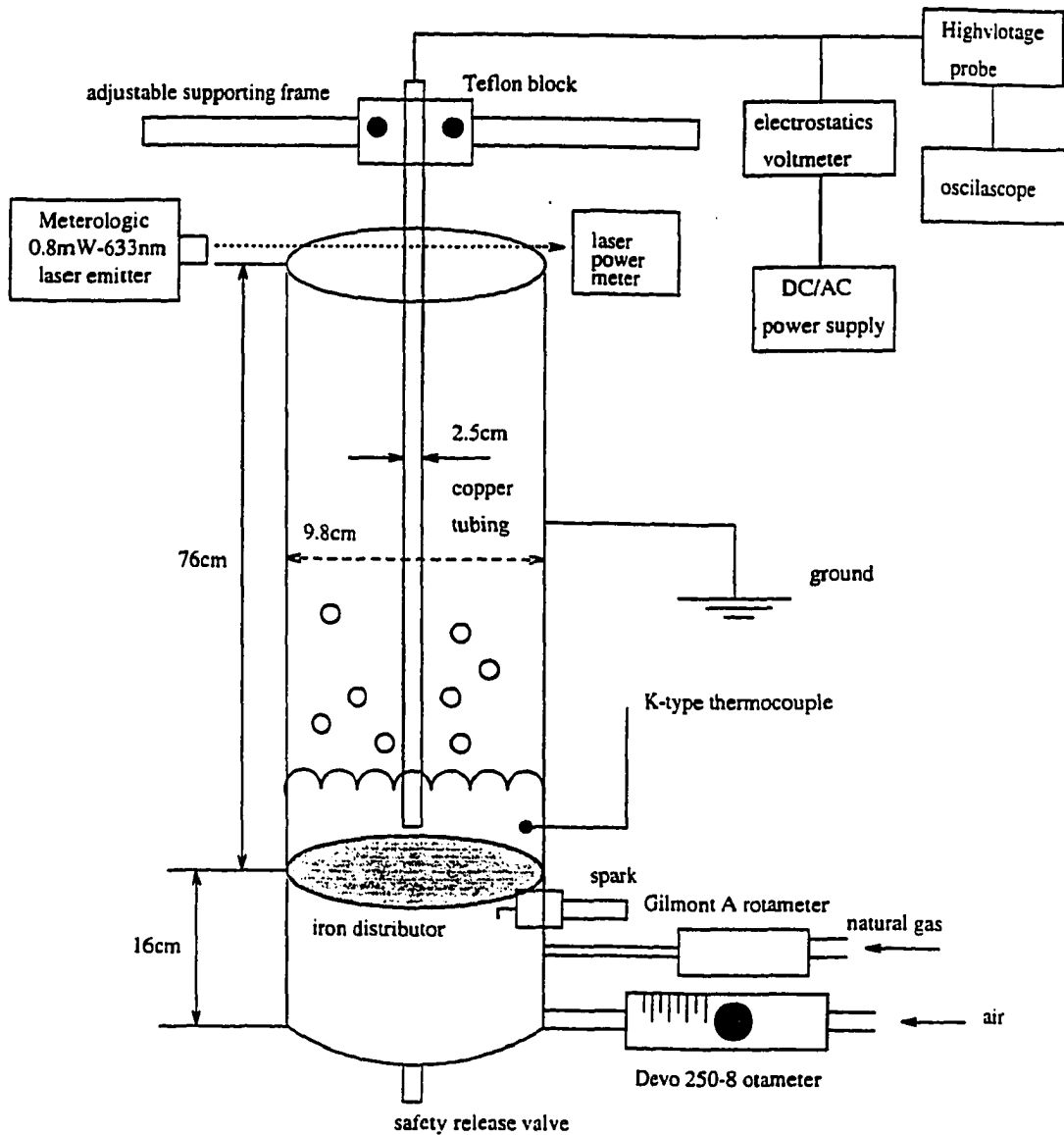


Figure 2.4 Brass fluidized bed with natural gas burning for measurement of high temperature elutriation constant

copper tubing and the bottom end was sealed with a piece of thin copper plate. The electrode was assembled on a frame which could move up and down in the fluidized bed. The bottom of the fluidized bed was a mixing chamber where the input flows of natural gas and air were mixed. A spark ignitor was located beneath the distributor to ignite the mixture. The laser beam system was used to measure the elutriation constant. A K-type thermocouple was imbedded at 5 cm above the distributor in the fluidized bed to measure the bed temperature. In this experiment, the temperature variance was large-approximately 20-30 °C. The temperature was controlled by the amount of natural gas burning in the fluidized bed. The air flow was held constant by controlling the rotameter. Initially, the bed was heated by burning the natural gas. After the bed temperature reached the specific value, such as 300 °C, the natural gas was turned off and 614 grams of pre-heated sand (up to 200 °C) was poured into the bed. The electrical field was turned on and air was allowed to flow into the bed. Readings from the laser power meter were taken every 15 seconds. The elapsed time for each run was 180 seconds. Different DC and AC electric voltages were applied.

In the case of an AC voltage, only a frequency of 3 Hz was studied, since it offered the maximum effect.

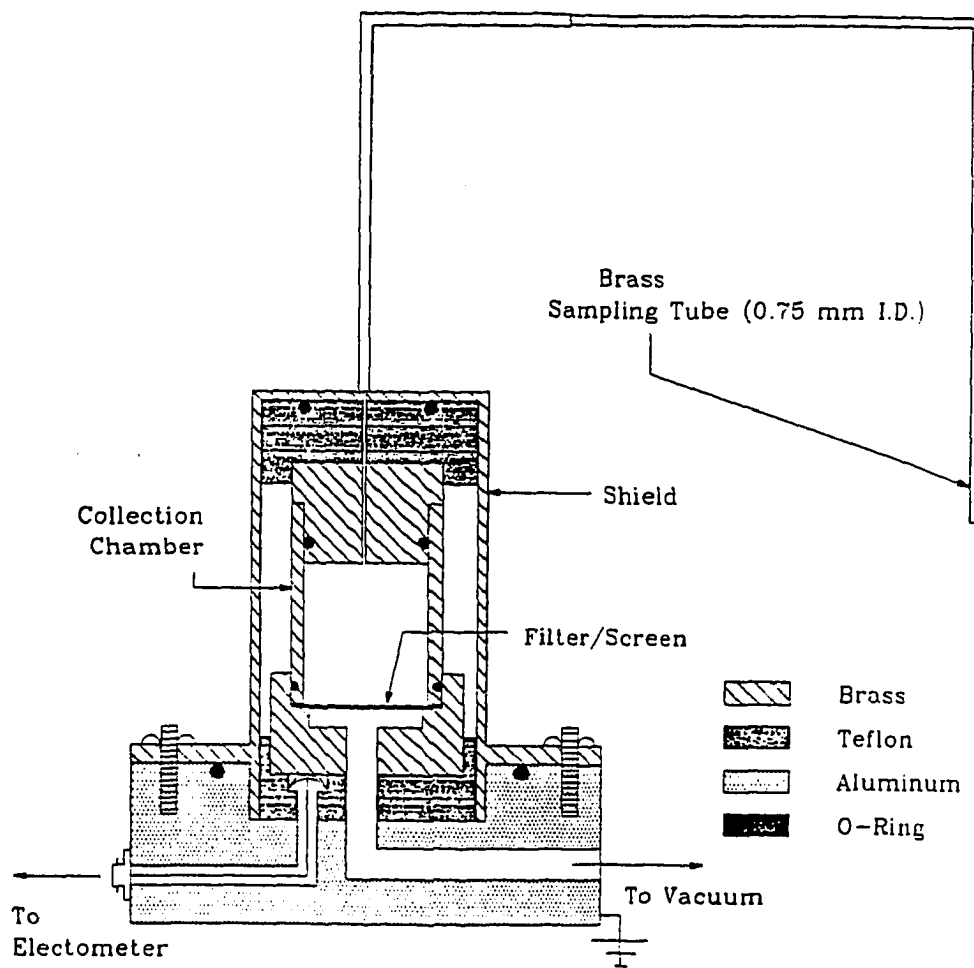
2.4.3 Charge of elutriated fines

The elutriated fines were captured by a Faraday cage with a vacuum pump, and the charge of these fines was measured by the Keithly Electrometer. The details of the Faraday cage are shown in Fig.2.5. During the test, the vacuum pump sucked fines into the Faraday cage and the data acquisition system recorded the charge accumulation. The total mass of fines collected could be found by measuring the mass of the filter paper which inserted into the bottom of the Faraday cage before and after each test run.

2.5 Yield Strength and Minimum Bubbling Velocity Measurement

2.5.1 Minimum bubbling velocity and pressure drop

The relationship between the minimum bubbling velocity and the yield strength of the fluidized bed were investigated through a Pyrex parallel fluidized bed, as shown in Fig.2.6.



Scale: 0.5 " = 1.0 "

Figure 2.5 Faraday cage for particle charge measurement

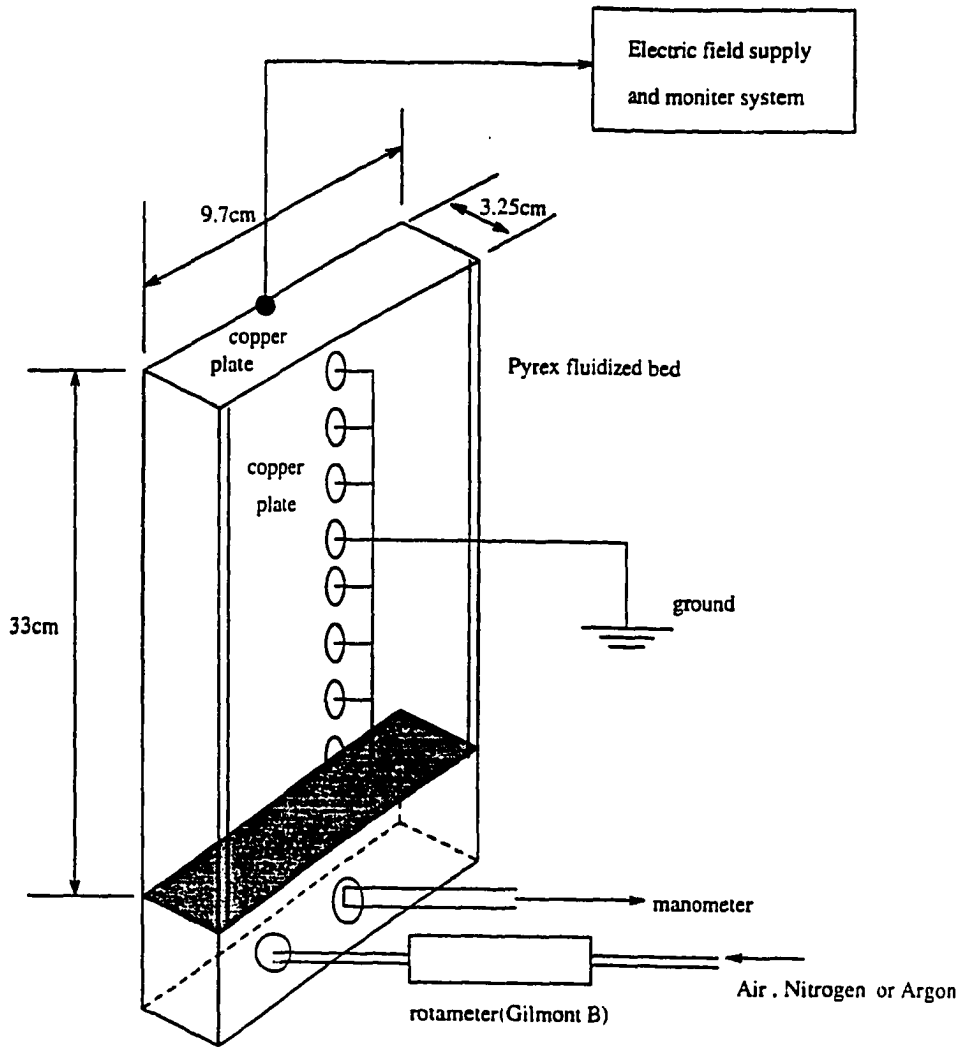


Figure 2.6 Pyrex fluidized bed for measurement of bubble control and bed elasticity modulus

The bed was 3.25 cm in width, 9.7 cm in length and 33 cm in height. Four different Fine Catalyst Chemicals (FCC) (Kaolin (1-B), Zeolitic-spent (1-A), Zeolitic-fresh (2-A), and Aluminum Oxide (3-A)) were used as bed material. The pressure drop (ΔP) was measured using a manometer. These rotameters were calibrated using a wet test meter with argon (Ar), nitrogen (N_2), carbon dioxide (CO_2) and air. The pressure drop across the sinter (or distributor) was obtained by running different velocities through the empty bed. Under a constant electric field strength, the superficial velocity of the mixture was gradually increased until bubbles formed. The gas velocity was then decreased until bubbles almost disappeared. This velocity was taken as the minimum bubbling velocity, U_{mb} . During the decreasing velocity procedure, the fluidized bed must be knocked by a rod to eliminate the wall effect. With the velocity and pressure drop known, the U_{mf} could be found from the plot of ΔP vs. U . The bed elasticity modulus could also be calculated from this data.

The frozen bed with an electric field was studied by using the FCC Zeolitic (fresh) (2A) as the bed material. The fluidized gas was Ar. The superficial velocity was fixed at

0.34 cm/s. The frequency was set to the desired value and the electric voltage was gradually increased. The bed height was recorded. The frequency was changed and the procedure was repeated.

2.5.2 The relative humidity effect

The relative humidity effect was also measured using the previous fluidized bed as illustrated in Fig.2.6. The bed material were 63-74 μm w.p. and n.w.p. Microbeads glass powders. Different R.H.s of the air were generated using two tanks of dry air. The R.H. of the dry air was closed to 9.8%. Air flowed through the bottom of a beaker which contained distilled water from the first tank. It was assumed that the air was saturated after passing through the water (R.H.=100%). A pre-mixed container was used to decrease the damping effect when the flow rate was changed. From the second tank, air flowed directly into the mixing container. The R.H. of the mixture was measured using two thermocouples: one was dry and the other was covered with a wick moistened with water. The experimental setup for obtaining various relative humidity is shown in Fig.2.7. For each test, the

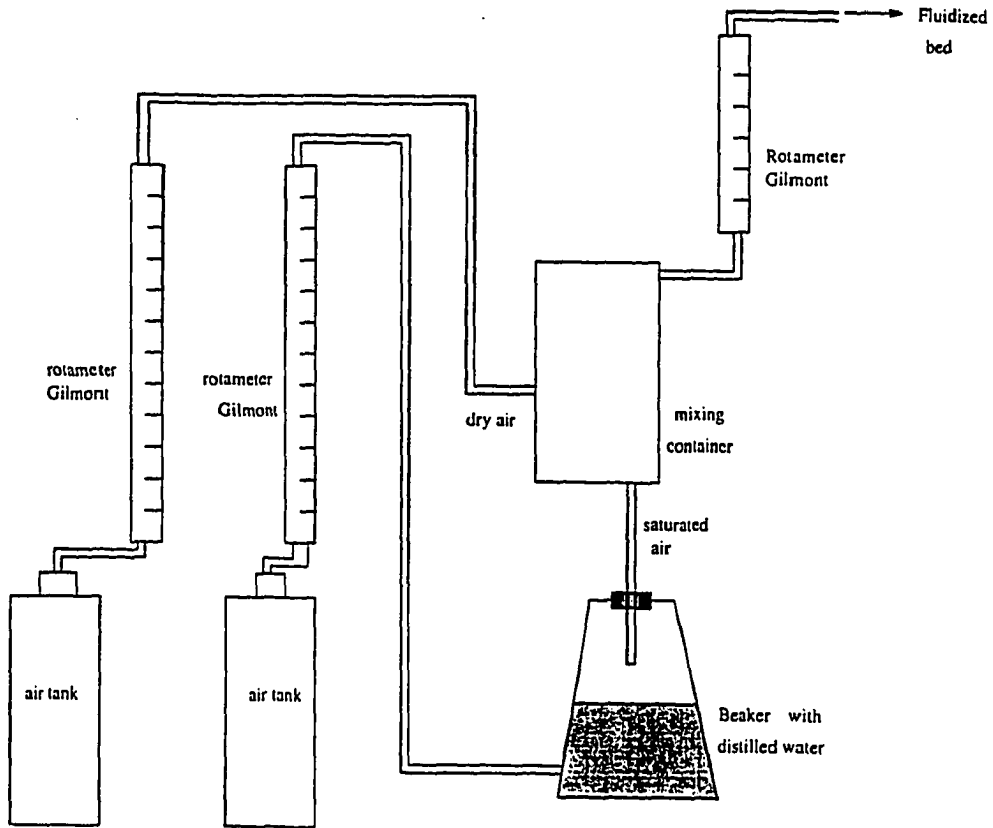


Figure 2.7 Instruments set up for controlling relative humidity

electric voltage was 3 Hz and 3 kV p-p. The bed height was recorded for various relative humidities. The bed elasticity modulus for 52.5 μm n.w.p. Microbeads glass powder with AC 3 kV, 3 Hz, p-p electric field at different R.H. were studied.

2.5.3 The effect of gas viscosity and particle diameter

Four different gases were used in this test. Argon, Air, CO_2 , and N_2 were used. The fluidized bed was the square-Pyrex bed was set at room temperature, as illustrated in Fig.2.6. The minimum bubbling velocity and bed height were recorded at various electric field strengths. The electric field frequencies were set to generate the minimum control effect. Also, the bed elasticity modulus was calculated for each set of data obtained from different gas.

The diameter effect was conducted using different diameter of n.w.p. Microbeads glass powders, ranging from 31.8 μm to 87.6 μm . The gas was Air with the electric field frequency was 3 Hz. It repeated the procedure of the gas viscosity effect test, during which bed height and velocity at minimum bubbling were recorded and the bed elasticity modulus was calculated.

2.6 Temperature Effect on the Bubble Control

The experimental setup for the temperature effect on the bubble control of the fluidized bed is illustrated in Fig.2.8. The fluidized bed was made from quartz glass. The inner diameter of the quartz bed was 9.0 cm and the height was 45.5 cm. An electrical heater (Omega CRWS124/120) was used to heat the fluidized bed. A K-type thermocouple with a controller (Omega 9000A) was used to control the bed temperature. The electrical heater was insulated to prevent large heat losses. 2.2cm in diameter copper electrode was inserted into the bed from the top. A manometer measured the pressure drop across the bed and a rotameter controlled the gas flow rate into the bed. The experiment procedure was as follows: the bed was heated by the electrical heater to the pre-set temperature, (T_1); the electric field was turned on, the electrical heater was turned off; the thermocouple was pulled out from the bed; and, finally the air flow was adjusted to the minimum bubbling condition. The pressure drop and bed height were recorded. Then, the thermocouple was put back into fluidized bed and the bed temperature (T_2) was recorded, The test temperature was obtained as $(T_1+T_2)/2$.

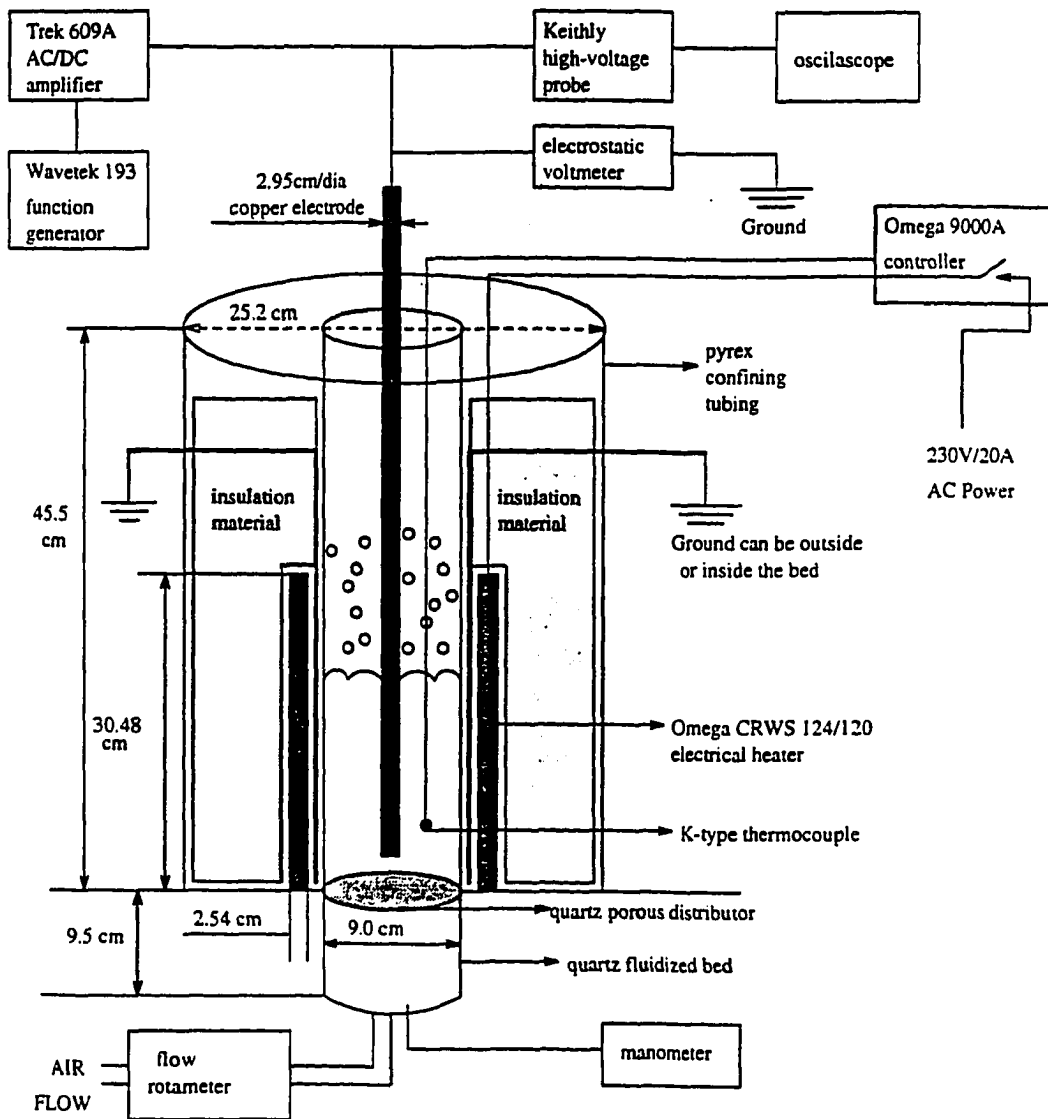


Figure 2.8 Quartz fluidized bed with electrical heating wire for measurement of the high temperature bubble control, bed resistivity and bed elasticity modulus

3. RESULTS AND DISCUSSIONS

3.1 Bed Conductivity

The conductivity of the fluidized bed was studied using the 44-74 μm w.p. spherical glass particles (Microbeads) in the parallel copper bed and oven. Figure 3.1 shows the log of the current density with the log of the electric field strength for constant bed temperatures. Figure 3.2 shows how the current density log varies from the log of the bed temperature, for constant electric field strength. Since the current density was a function of both the electric field strength and bed temperature, the following equation could be written (Colver et al., May, 1992) as

$$J = AE^m T^n \quad (3.1)$$

where J was the current density (A/m^2), A , m , and n were constants, E was the electric field strength (V/m), and T was temperature ($^{\circ}\text{K}$). Constants m and n represented the slope of the curves in Fig.3.1 and Fig.3.2, respectively. All the lines in Fig.3.1 had approximately the same slope, which was calculated to be 1.69. Similarly, all the lines in Fig.3.2

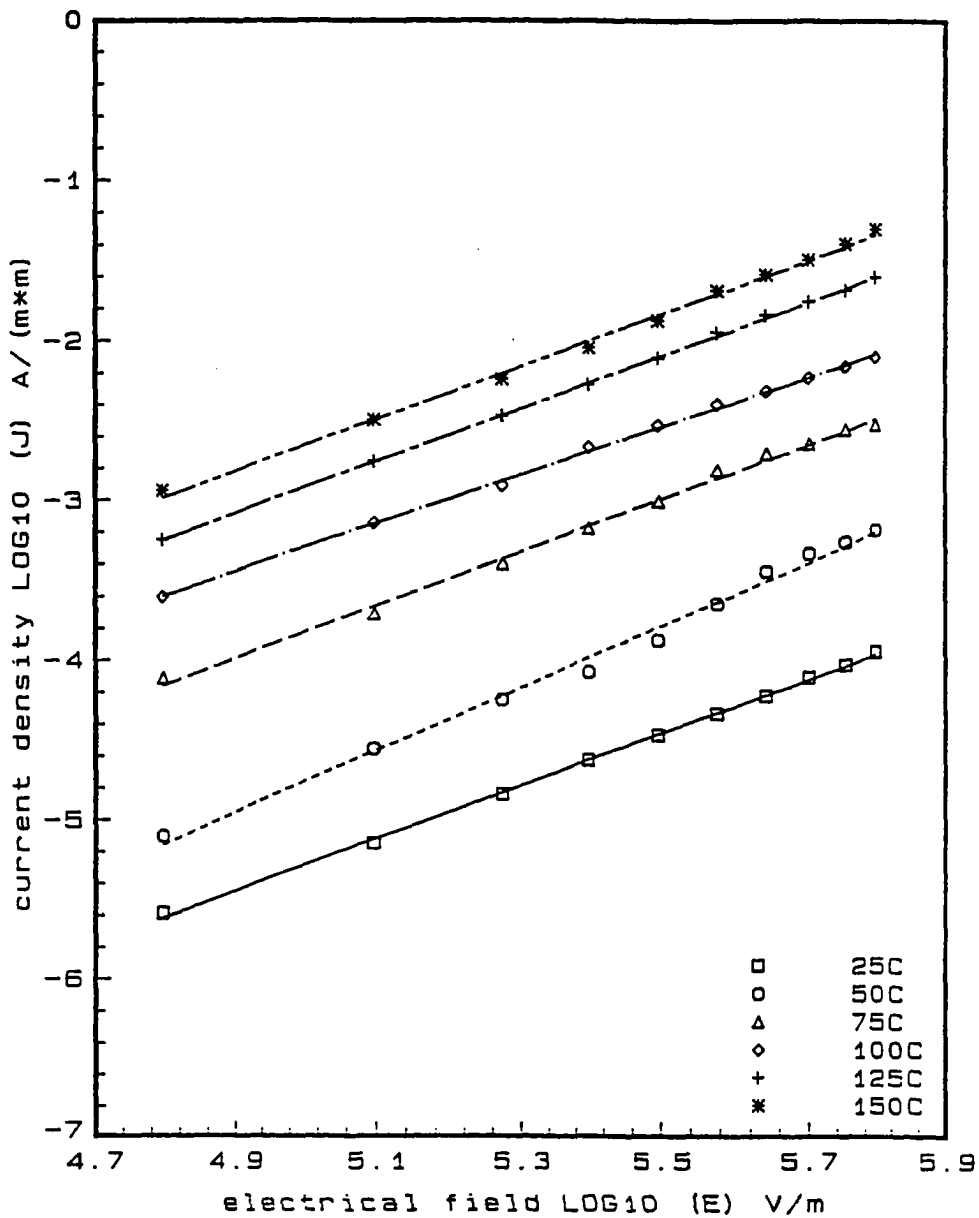


Figure 3.1 Log-log plot of current density versus electric field strength showing linearity with effect of temperature

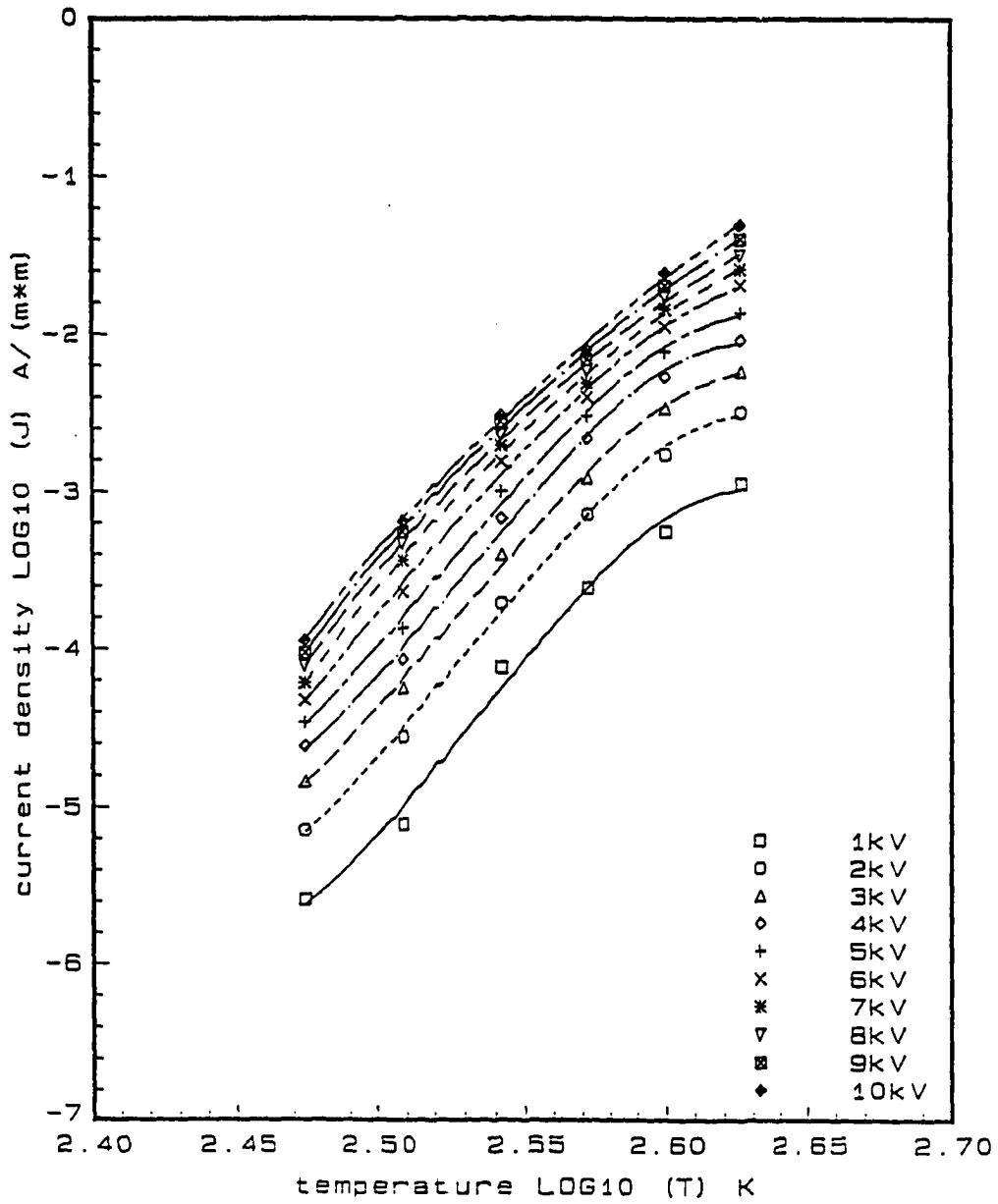


Figure 3.2 Log-log plot of current density versus temperature showing (approximately) linearity with effect of electric field strength (potential)

had approximately the same slope, which was estimated to be 17.71. The constants could be determined from Fig.3.1 or Fig.3.2. Thus, Eqn.3.1 could be rewritten as

$$J = 3.6074 \times 10^{-58} E^{1.69} T^{17.71} \quad (3.2)$$

Fig.3.3 showed Eqn.3.2 plotted for all of the data.

Equation 3.2 could be put into a more general form by taking into account the particle diameter and the relative humidity of the bed. Colver (1980) gave an equation relating the particle diameter and the R.H. to the bed conductivity of 3M glass superbrite beads as

$$\alpha(\Omega - m) = 3.25(d)^{5.12} \exp[-0.188 * R.H.] \quad (3.3)$$

where α was the bed conductivity ($\Omega - m$), d was the particle diameter (μm), and R.H. was the relative humidity (%). Thus, assuming that the bed conductivity for the glass particles (Microbeads) would have a similar dependence in the particle diameter and R.H. as that of the 3M superbrite beads, Eqn.3.2 may be placed into a more general form. The bed conductivity (α) for 44-74 μm Microbeads glass spheres was given as (normalized to R.H.=8% and $d=60.5 \mu m$)

$$\alpha(\Omega - m) = 9.406 \times 10^{-48} E^{-1.69} T^{-17.71} (d)^{5.12} \exp[-0.188 * R.H.] \quad (3.4)$$

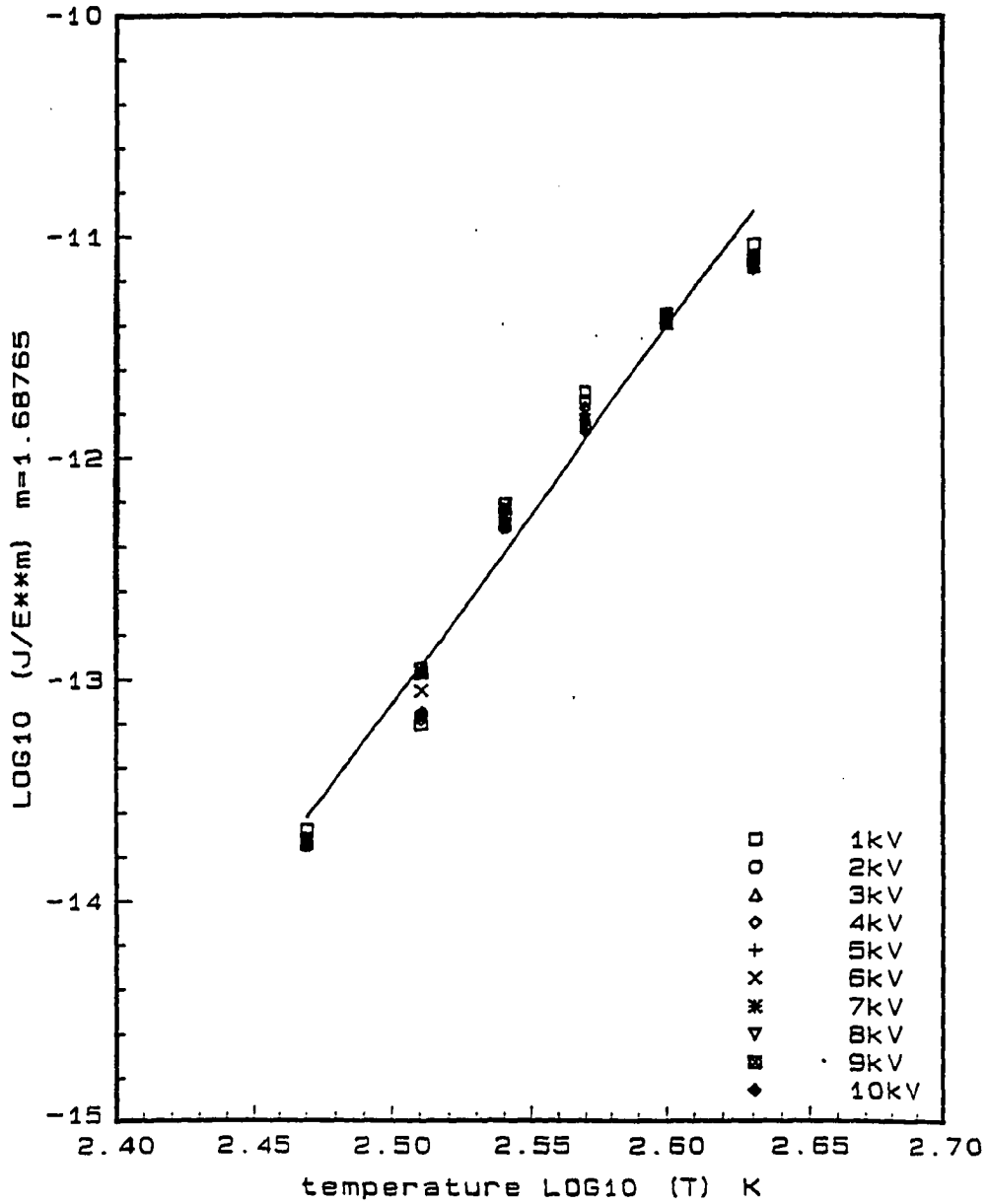


Figure 3.3 Reduced data, current density, electric field strength, and temperature with least squares fit of Eqn.(3.2)

where d in μm , and R.H. in percent. Eqn.3.1 was generally valid in temperature dependence. Eqn.3.3 had also been used to predict bulk bed current under the influence of high voltage fields and for evaluating the particle charge and charge relaxation time, which was useful information when considering the charge adjustment time of the individual particles.

The fines in the sand packed bed affected the bed conductivity significantly. Figure 3.4 and Figure 3.5 showed the bed conductivity before and after fluidizing sand for 15 minutes, respectively. The current density in Fig.3.5 was much larger than that in Fig.3.4. The increasing current density (or decreasing resistivity) was due to the fines which were linked between the larger particles and acted as an extra resistor. From Fig.3.6, it can be seen that the fines attached to the large particles were significantly decreased after 15 minutes of fluidization.

3.2 Correlation for Bed Expansion with an Electric Field

The bed expansion was affected by the strength and frequency (in the AC electric field) of the electric field,

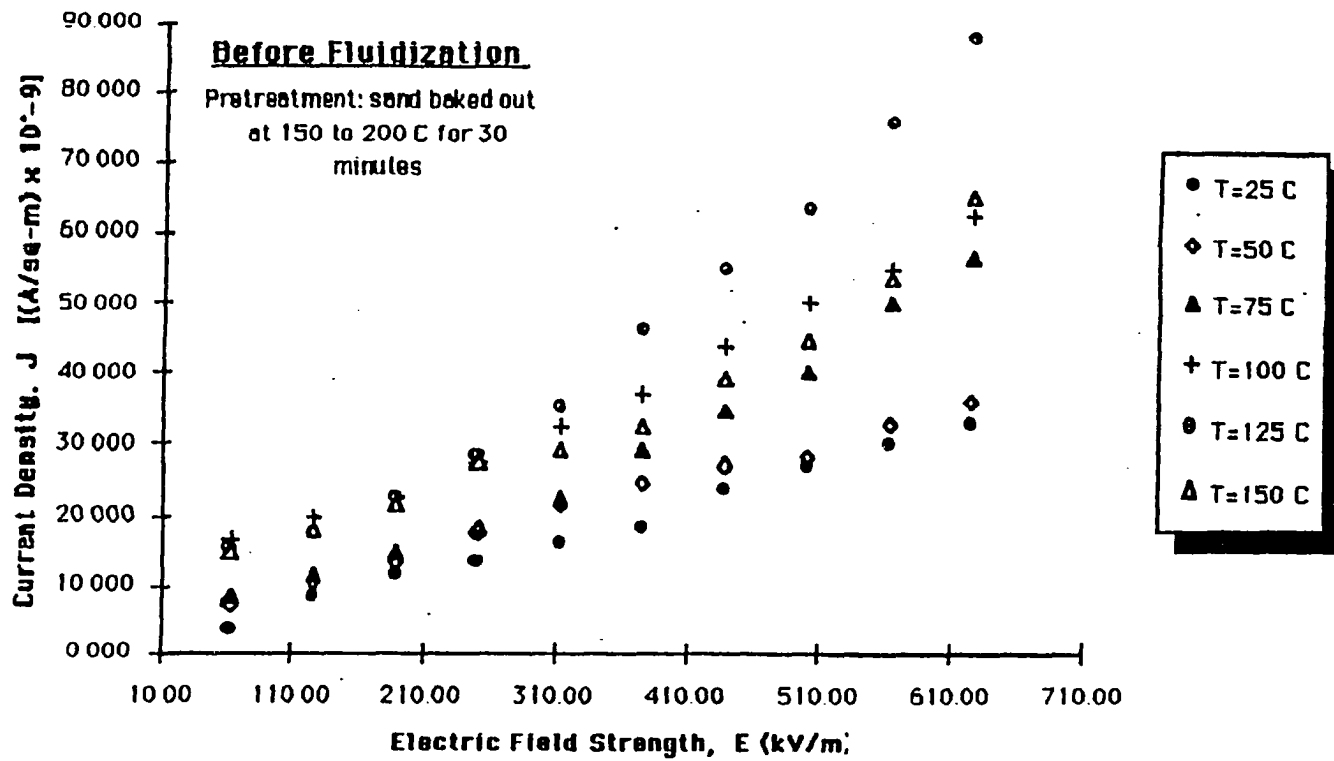


Figure 3.4 Packed bed, current density of sand with fines at various temperature

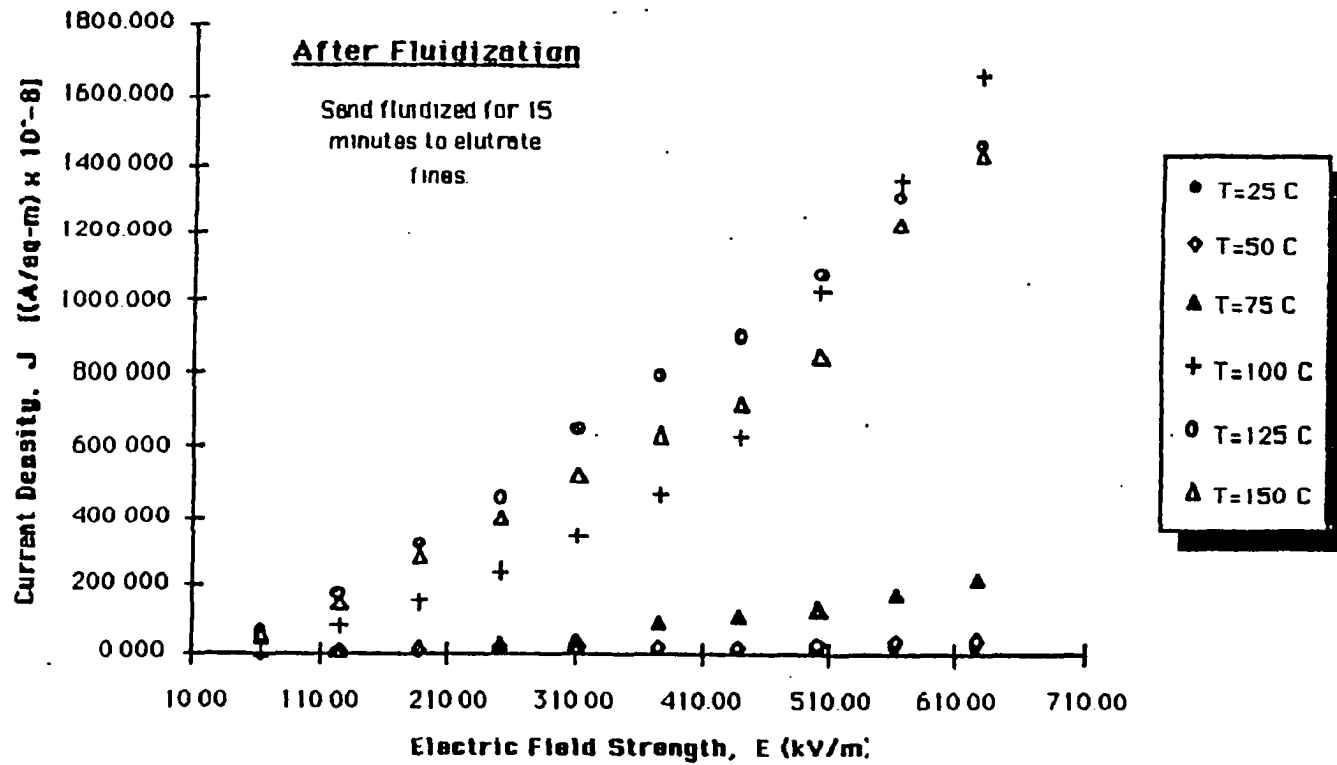
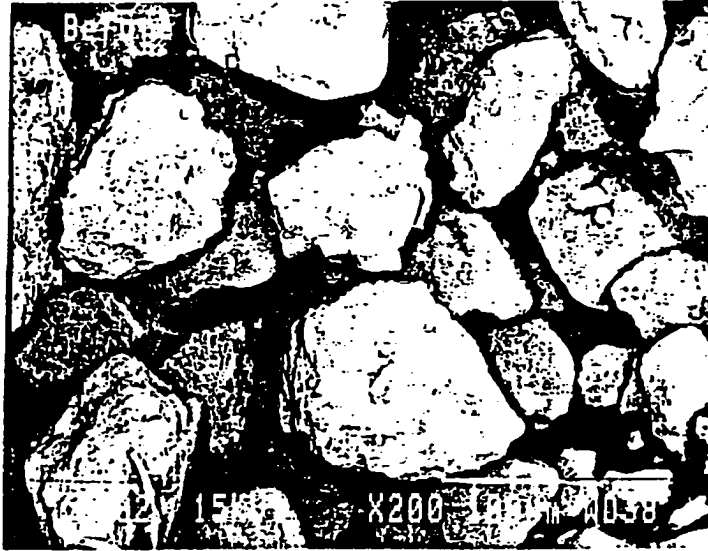


Figure 3.5 packed bed, current density of sand at various temperature with 15 minutes of fluidization to reduce fines



(a)



(b)

Figure 3.6 Sample of sand particles, (a) before, (b) after running the fluidized bed for 15 minutes (SEM, Kevex, automated image analyzer), x200

the R.H., the temperature, and the properties of particles, such as diameter, conductivity, and density. Figure 3.7 shows that bed expansion, given as voidage, is continuous, with superficial velocity at a fixed field strength up to the condition of minimum bubbling, using the 44-74 μm w.p. glass spheres under constant R.H. (9.8%) and electric field frequency of 3 Hz. The separation of the 187.5 kV/m curve from the trend curve of the other electric field strengths was thought to be due to the wall effect, because the experiment was conducted in the parallel copper bed. The minimum bubbling velocity was dependent on the electric field strength. A correlation of the dependence between U_{mb} and E is shown in Fig.3.8 as

$$U_{mb} = 1.042 \times 10^{-6} E (\text{V/m}) + 0.74 (\text{cm/s}) \quad (3.5)$$

The U_{mb} was a function of electric field strength, but the U_{mf} was not and was just a property of the bed. The temperature effect on bed expansion is shown in Fig.3.9. The increase in the voidage of the bed was significant, from 0.45 to 0.51, when the temperature was 125 °C and E was 125 kV/m.

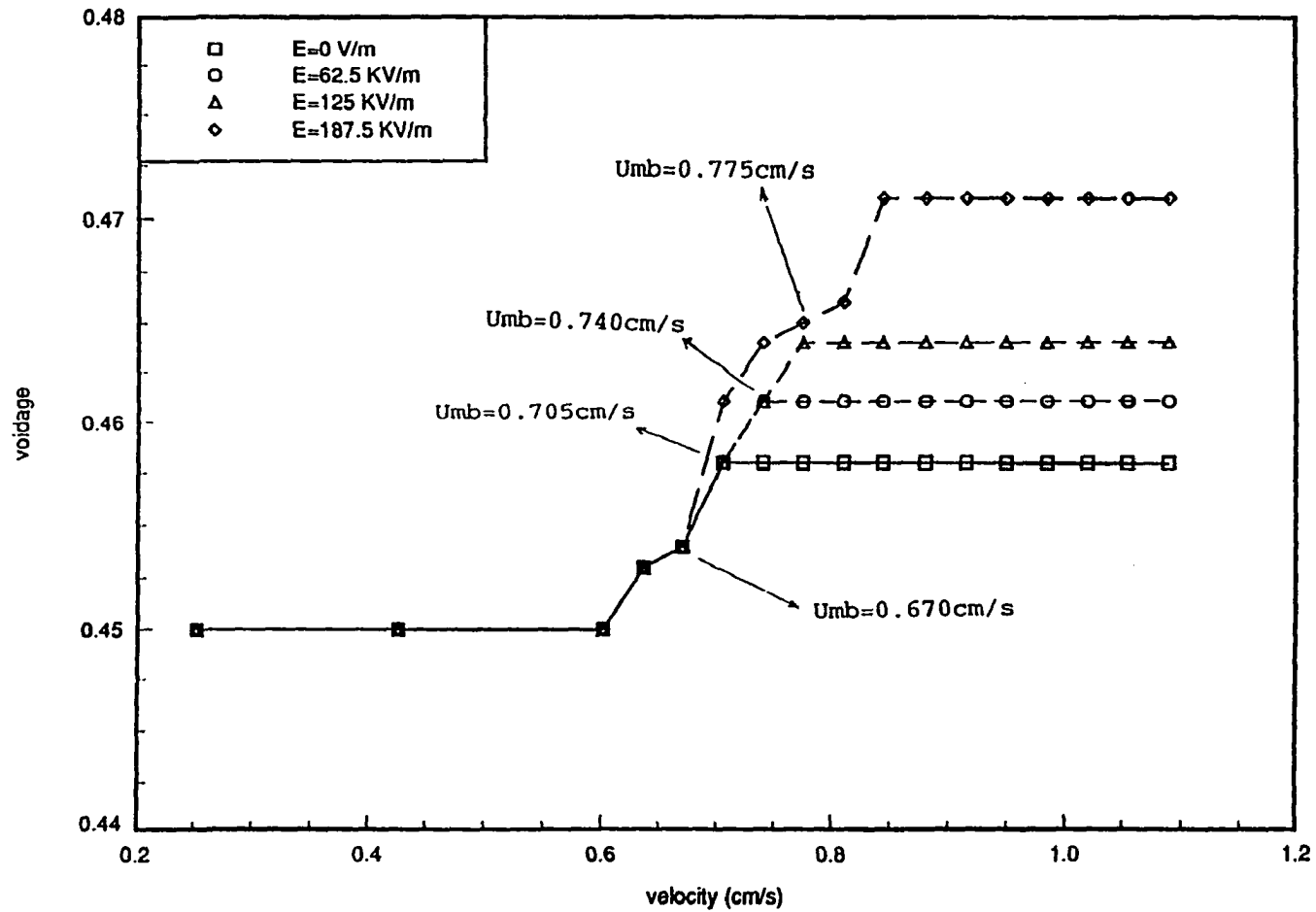


Figure 3.7 Bed voidage with superficial velocity, increased effect of electric field strength. 44-74 μ m with air, AC-3Hz, peak-to-peak (p-p), R.H.=9.8%

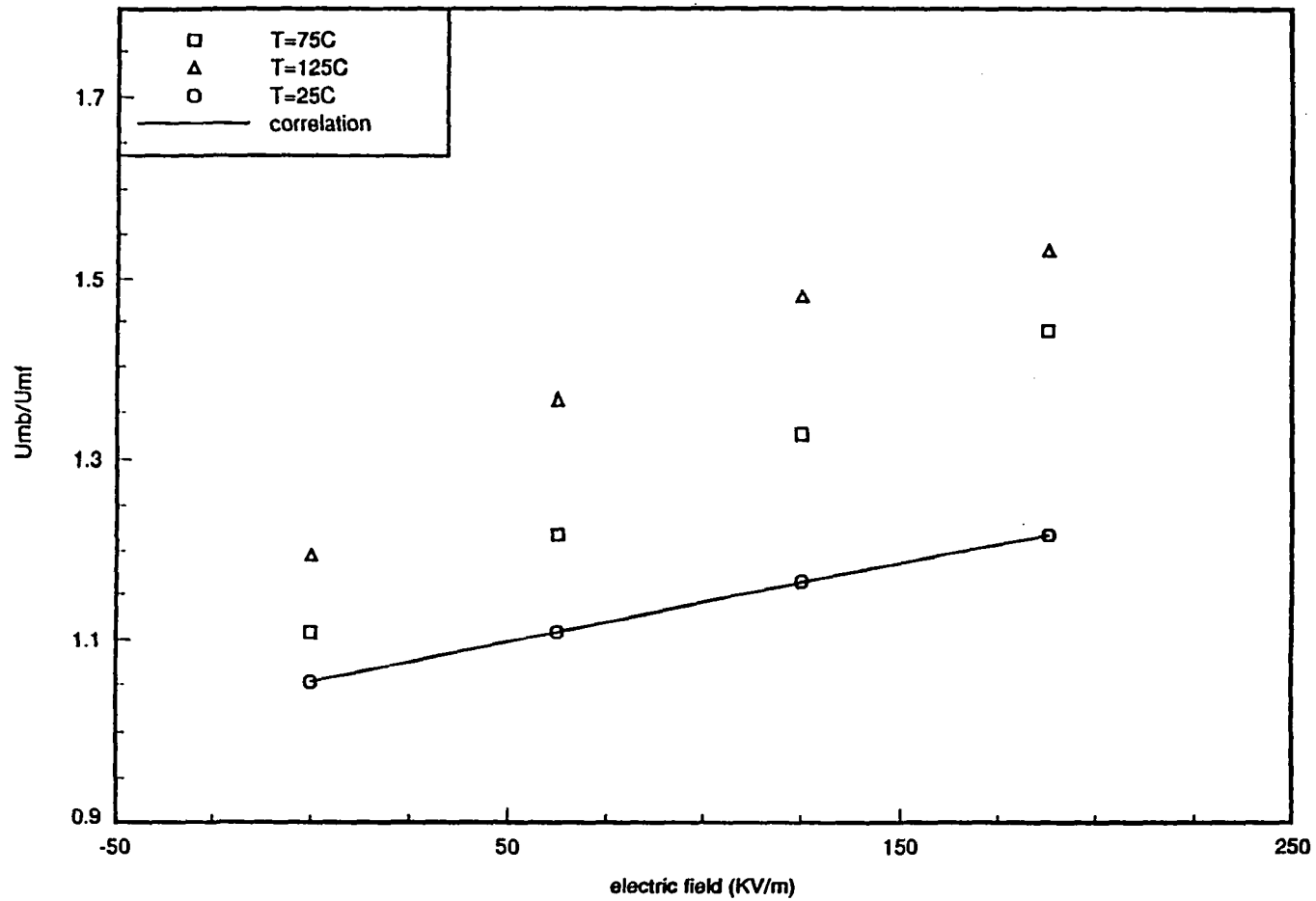


Figure 3.8 Minimum superficial velocity for onset of bubbling with p-p field strength, effect of temperature, 44-74 μ m with Air

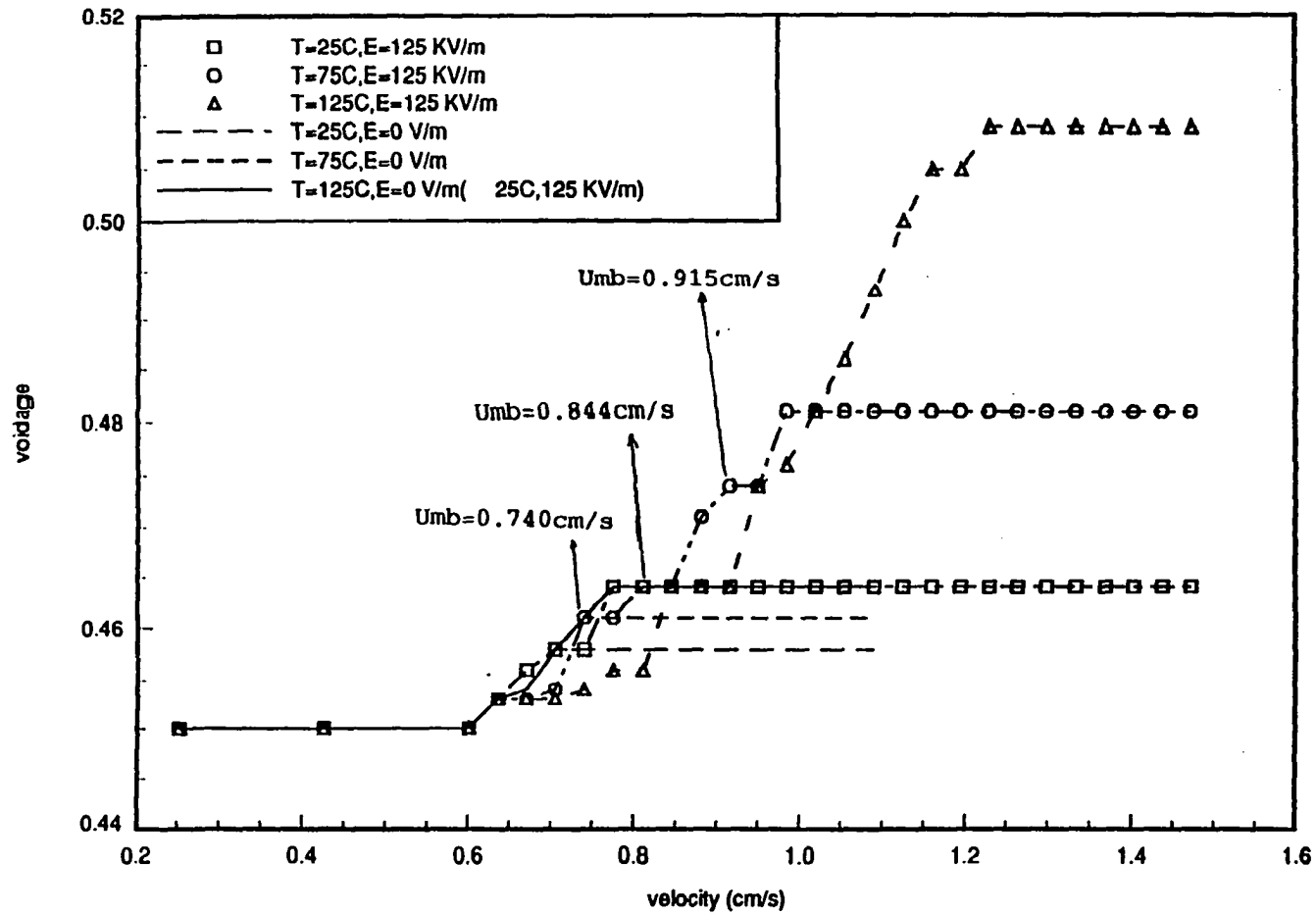


Figure 3.9 Bed voidage with superficial velocity, increased temperature at various electric field strength, 44-74 μ m with air

3.2.1 Correlation with two-phase theory

A correlation for bed height (H) with electric field strength and superficial velocity was obtained by extending the two-phase fluidized bed theory (Davidson and Harrison, 1985)

$$\frac{H-H_{mf}}{H} = \frac{U-U_{mf}}{U_b} = C(U) \frac{U-U_{mf}}{U_{mf}} \quad (3.6)$$

where the bubble rise velocity U_b was replaced approximately with U_{mf} , which was derived as a function $C(U)$. The bed height H was correlated with electric field E at a constant superficial velocity (U) and the result was then correlated with the superficial velocity in the form suggested by Eqn.3.6. The equation could be expressed as

$$\frac{H-H_{mf}}{H} = C(U) \left[\frac{U-U_{mf}}{U_{mf}} \right]^a \exp[b * E(V/m)] \quad ; \quad U \geq U_{mb} \quad (3.7)$$

where $C(U)$, a , and b were constants. The correlation for the 44-74 μm Microbeads w.p. glass spheres under constant R.H. (=9.8%) and electric field frequency (=3 Hz) at room temperature was given as

$$\frac{H-H_{mf}}{H} = 0.0507 \left[\frac{U-U_{mf}}{U_{mf}} \right]^{0.567} \exp[1.815 \times 10^{-6} E(V/m)] \quad ; \quad U \geq U_{mb} \quad (3.8)$$

The two-phase fluidized bed theory gave an experimental dependence of unity on the velocity term for bed expansion, where a dependence of 0.567 with $C(U) \approx 5.07$ was found. Examining the relation between U_b and $U - U_{mf}$, it showed that U_b was in proportion to $(d_b)^{0.5}$, where d_b was the average bubble diameter (Davidson, 1985). However, d_b was also in proportion to the $(U - U_{mf})^{0.4}$ according to Darton et al., or $(U - U_{mf})^{0.5}$ according to Rowe, or one of $(U - U_{mf})^{0.4}$ and $(U - U_{mf})^{0.94}$ according to Geldart (Geldart, 1986). Therefore, the value of a in Eqn.3.7 should range from 0.53 to 0.8. The average experimental value was 0.603. Eqn.3.8 was plotted in Fig.3.10 for various experimental data at different superficial velocities. Using the relationship for conservation of mass $(1 - \varepsilon)H = (1 - \varepsilon_{mf})H_{mf}$ with the relationship of voidage from the two-phase theory $(1 - \varepsilon) = (1 - \varepsilon_{mf})(1 - \varepsilon_b)$, Eqn.3.8 could be cast into the following form

$$\varepsilon = 1 - (1 - \varepsilon_{mf}) \left[1 - C(U) \frac{U - U_{mf}}{U_{mf}} \right]^{0.567} \exp[1.815 \times 10^{-6} E(V/m)] ; U \geq U_{mb} \quad (3.9)$$

where $\varepsilon_{mf} = 0.45$ for the 44-74 μm Microbeads glass spheres. Eqns.3.8 and 3.9 were restricted to minimum values of $U \approx U_{mb}$

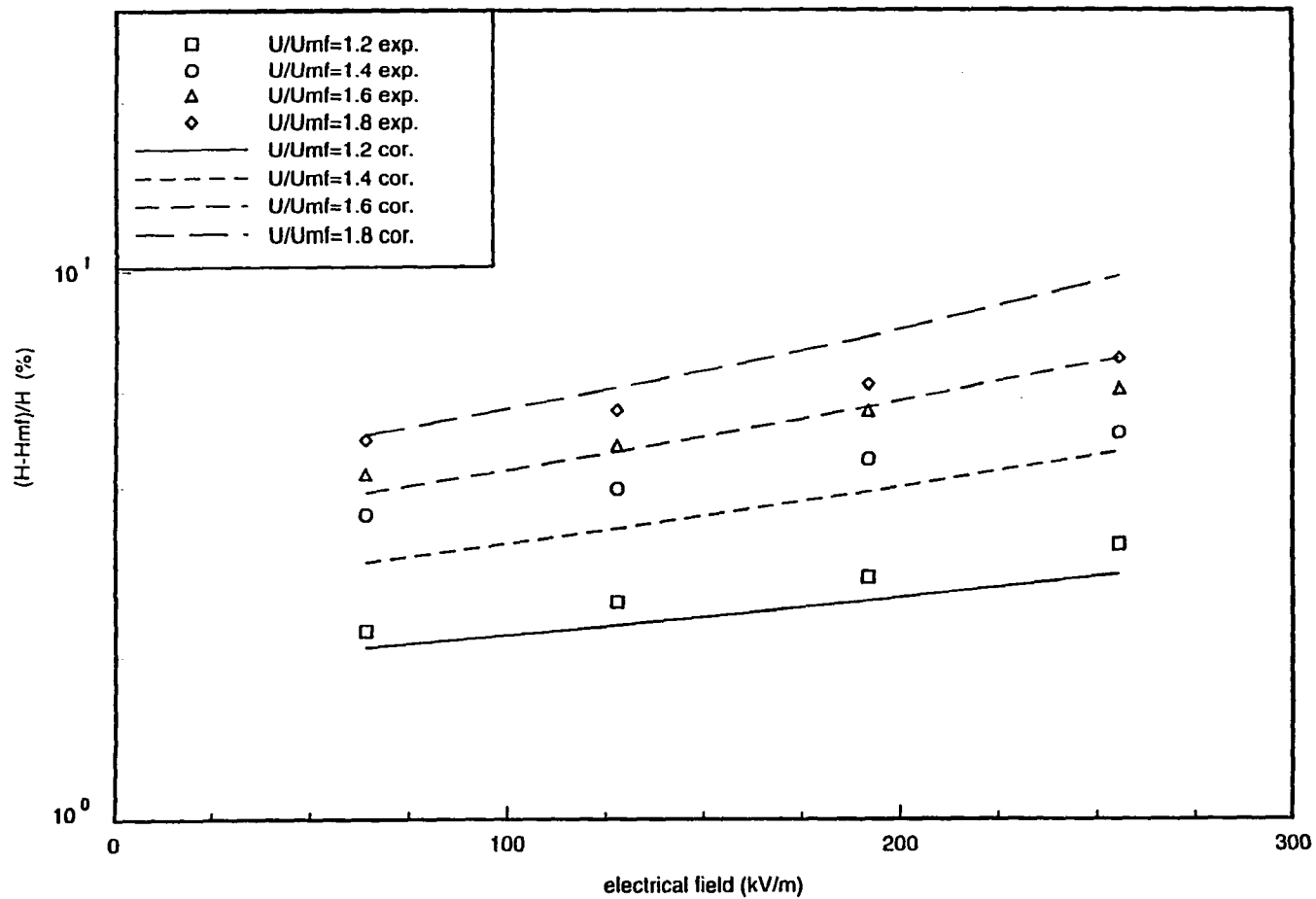


Figure 3.10 Bed expansion with electric field strength and superficial velocity, experimental data and least squares fit. 74-144 μ m with air

for a given H (or E), which was a Richardson-Zaki equation and gave maximum values of E (H or ϵ) for a given U. For example, using data from Fig.3.7, a relation was found for our range of data as

$$\frac{U_{(\text{cm/sec})}}{6.93} = \epsilon^{1.54} \quad (3.10)$$

for $U_{mf} \leq U \leq U_{mb}$ and Eqn.3.5 was used to calculate the later restriction. Eqn.3.5 could be substituted into Eqn.3.9 to obtain the limiting relationship between voidage ϵ and electric field strength E. Together, Eqns.3.5, 3.8, 3.9, and 3.10 formed a complete set of equations describing the bed expansion for the range of our data ($E \leq 313\text{kV/m}$, $U \leq 2.5\text{cm/sec}$). The constants of the bed expansion correlation (Eqn.3.7) for different particle diameters were shown in Table 3.1. It was difficult to draw any relationship between particle diameter and the constants, $C(U)$, a, and b. Therefore, assuming no particle diameter effect and taking the average of the first six data in Table 3.1, a more general correlation for the bed height (%) and bed voidage is given as

$$\frac{H - H_{mf}}{H} = 0.0746 \left[\frac{U - U_{mf}}{U_{mf}} \right]^{0.603} \exp[0.953 \times 10^{-6} E(\text{V/m})] \quad (3.11)$$

$$\varepsilon = 1 - (1 - \varepsilon_{mf}) \left[1 - 0.0746 \frac{U - U_{mf}}{U_{mf}} \right]^{0.603} \exp[0.953 \times 10^{-6} E(\text{V/m})] ; U_{mf} \leq U \leq U_{mb,E} \quad (3.12)$$

For a given superficial velocity U , the limiting conditions of the electric field strength E_{mb} on the overall bed voidage ε permitted in Eqn.3.12 or on $(H - H_{mf})/H$ in Eqn.3.11 were given by the following relationships

$$\left(\frac{U_{mb,E}}{U_{mf}} - 1 \right) = 10^{3.81 \times 10^{-1} d(\mu\text{m}) - 3.346} E_{mb}(\text{kV/m}) \quad (3.13)$$

and

$$\varepsilon^n = \frac{U(\text{cm/s})}{u_s'} ; U_{mf} \leq U \leq U_{mb,E} \quad (3.14)$$

where u_s' was the settling rate of a single isolated particle and n depends on the corresponding Reynolds number (e.g. $n \approx 2.4 \rightarrow 4.65$). The constants u_s' and n in Eqn.3.14 represented different diameter particles which were shown in Table 3.2. The calculated values for 63-74 μm glass particles in Table 3.2 were $u_s' = 30.4$ and $n = 4.356$. They were close to the experimental values 39.4 and 4.52, respectively. It was very difficult to correlate the particle diameter with constants

Table 3.1 The constants, $C(U)$, a , and b for Eqn. (3.6)

particle diameter μm	b ($\times 10^{-6}$)	a	$C(U)$
44-53	0.937	0.567	0.0723
63-74	0.977	0.262	0.0855
74-88	1.254	1.085	0.0609
88-104	0.859	0.338	0.0799
104-125	0.936	1.118	0.0757
125-147	0.756	0.249	0.0759
44-74	1.815	0.567	0.0507
74-144	2.208	0.929	0.0951

Microbeads w.p. for 44-74 μm and 74-144 μm glass spheres. n.w.p. for others. R.H.=9.8%, $T=24^{\circ}\text{C}$, 3 Hz peak-to-peak electric field.

Table 3.2 Constants in Richardson-Zaki equation

particle diameter, μm	u_s' , cm/sec	n
44-53	12.64	4.26
63-74	39.4	4.52
74-88	12.80	3.41
88-104	22.00	3.89
105-125	26.56	3.31
125-147	14.24	2.38

Microbeads n.w.p. glass spheres, R.H.=9.8%, air, room temperature, AC 3 Hz peak-to-peak electric field.

u_s' and n because of the wide scatterness among the values. In fact, the Richardson-Zaki type Eqn.3.14 was unnecessary in lieu of Eqns.3.12 and 3.13, and served mainly as a check on the permitted bed voidage. The correlation and summary data are shown in Fig.3.11 and Fig.3.12 for Eqns.3.11 and 3.13, respectively. Each correlation line fitted the experimental data quite well.

3.2.2 Frequency effect

The frequency of the AC electric field affected the bed expansion. Fig.3.13 shows the bed expansion of 74-144 μm w.p. glass spheres for an AC electric field with the strength of 5 kV p-p. The peak of the bed expansion occurred at 3 Hz and decreased rapidly when the frequency was increased or decreased from 3 Hz. All bed materials showed this same frequency effect during the tests except the peaking frequency was shifted because of different characteristics of the fluidized beds.

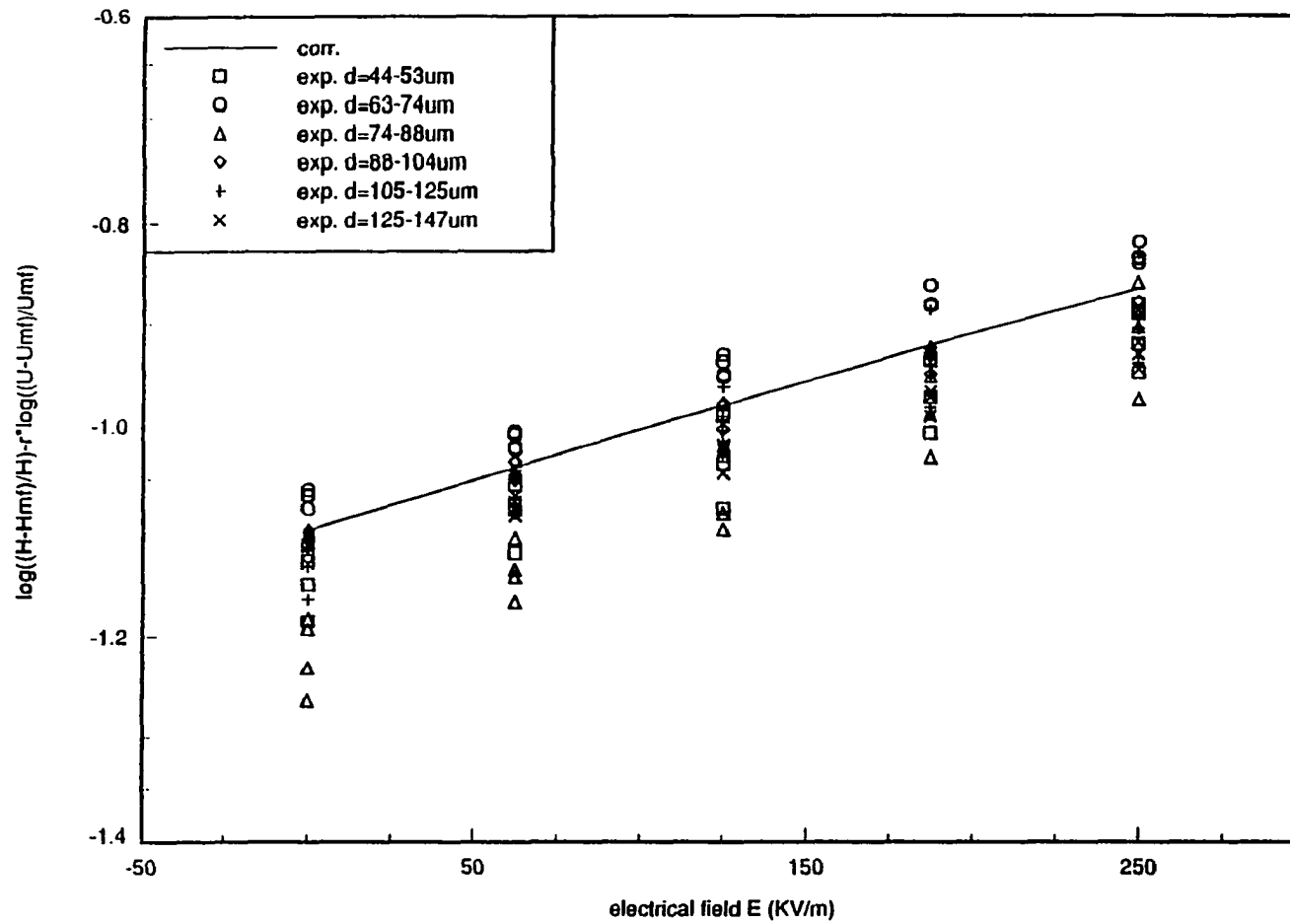


Figure 3.11 Summary data for bed expansion and electric field strength for various particle size

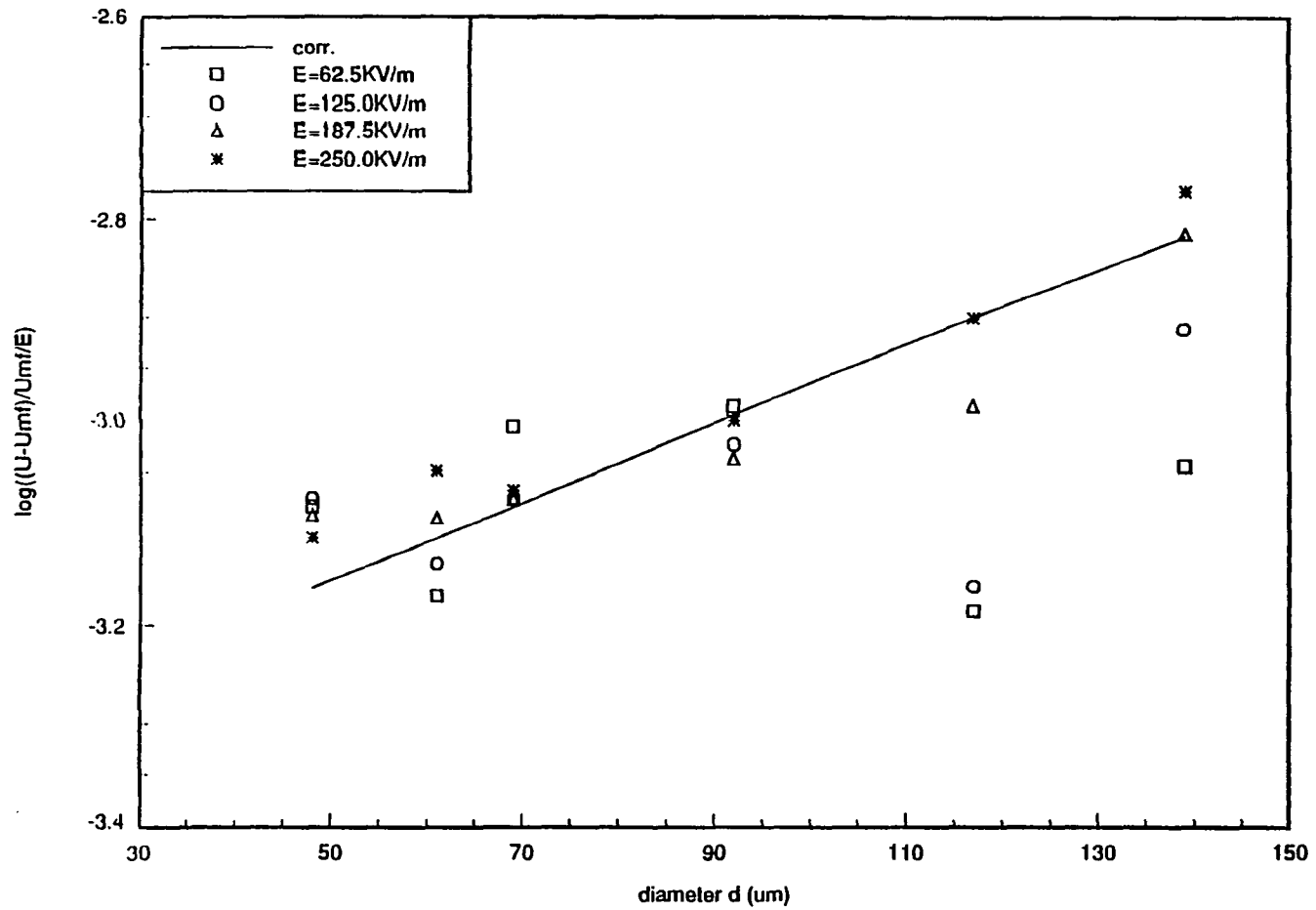


Figure 3.12 Summary data for superficial velocity and particle diameter (median) for various electric field strength

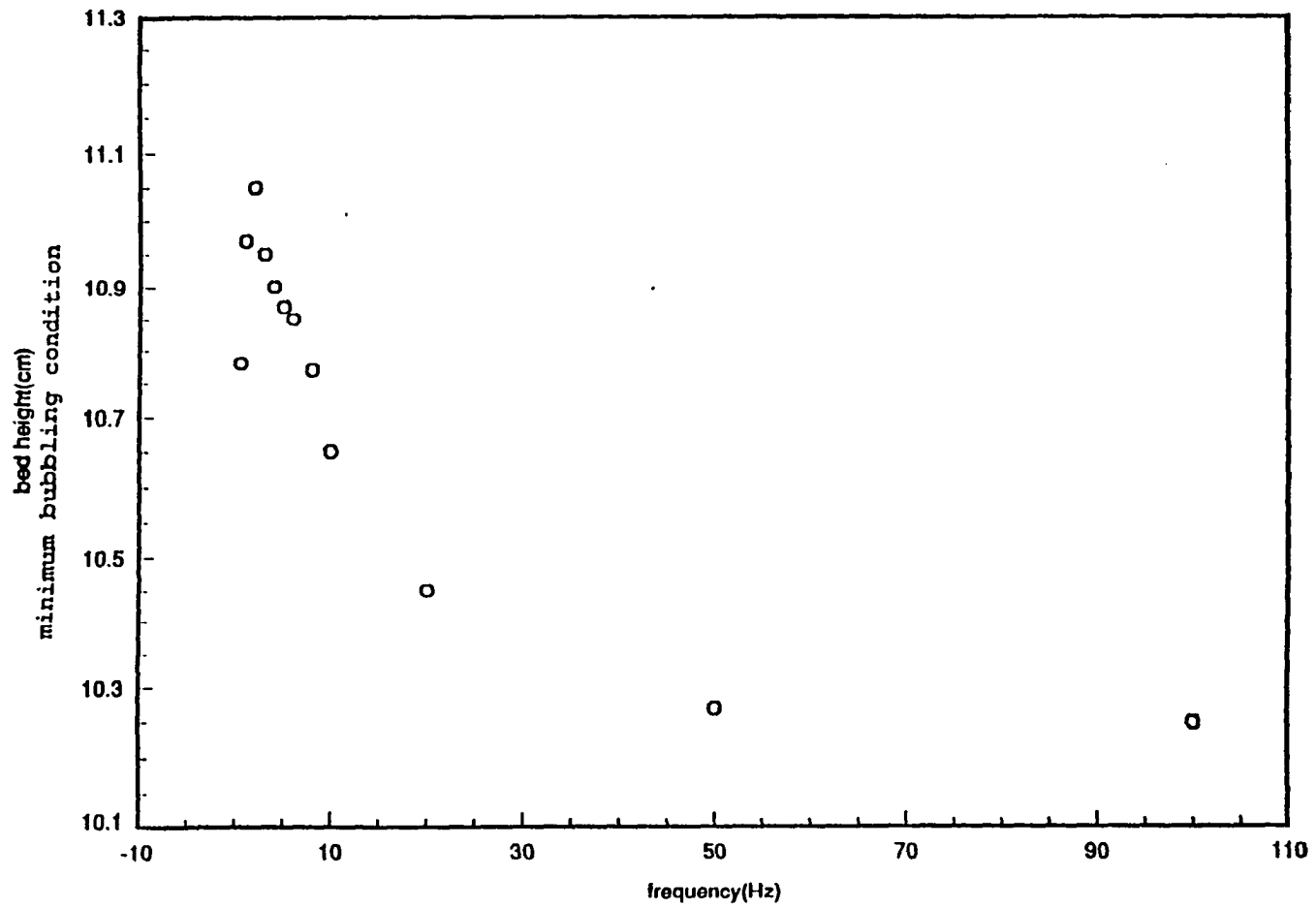


Figure 3.13 Bed expansion with frequency, 74-144 μ m, AC-5kV p-p, 24 $^{\circ}$ C, air

3.2.3 Relative humidity effect

The R.H. significantly affected the bed expansion, since the bed conductivity decreased exponentially with the R.H. (see Eqn.3.4). Fig.3.14 and Fig.3.15 showed the bed expansion under different R.H. using the 63-74 μm Microbeads n.w.p. and w.p. glass spheres fluidized with air, for an electric field of 3 kV and 3 Hz, and at room temperature. A peak in bed expansion was found to occur in this experiment. Gradually increasing R.H. from low to high would decrease the resistivity of the fluidized bed and increase the current flowing through the bed. Therefore, the electric force between the particles also increased. However, further increasing the R.H. could freeze the bed since the inter-particle electric force was so large that the particles stuck together and a contraction occurred. The decrease of bed height was due to this contraction. The R.H. peak in the expansion of the fluidized bed was close to 30% in both particles.

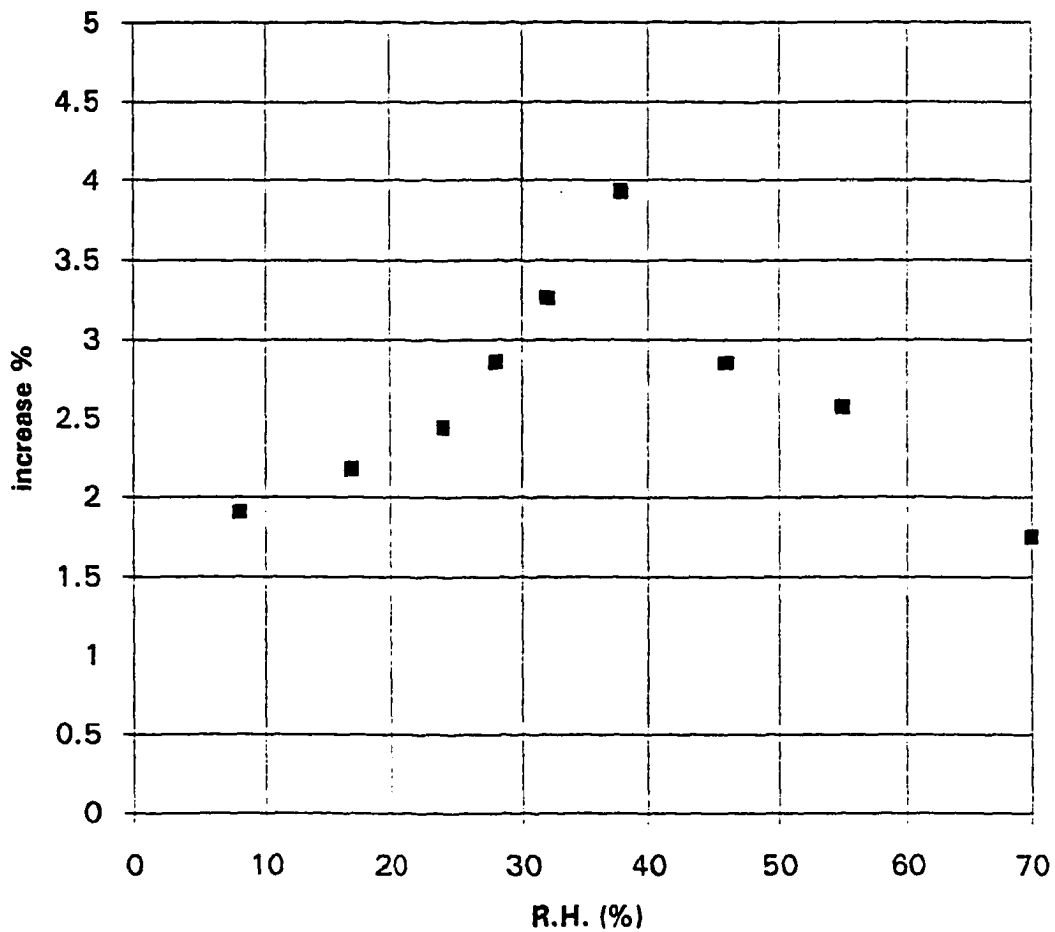


Figure 3.14 Freezing bed with increased relative humidity, 44 μ m n.w.p. glass beads, AC-3Hz-3kV, p-p

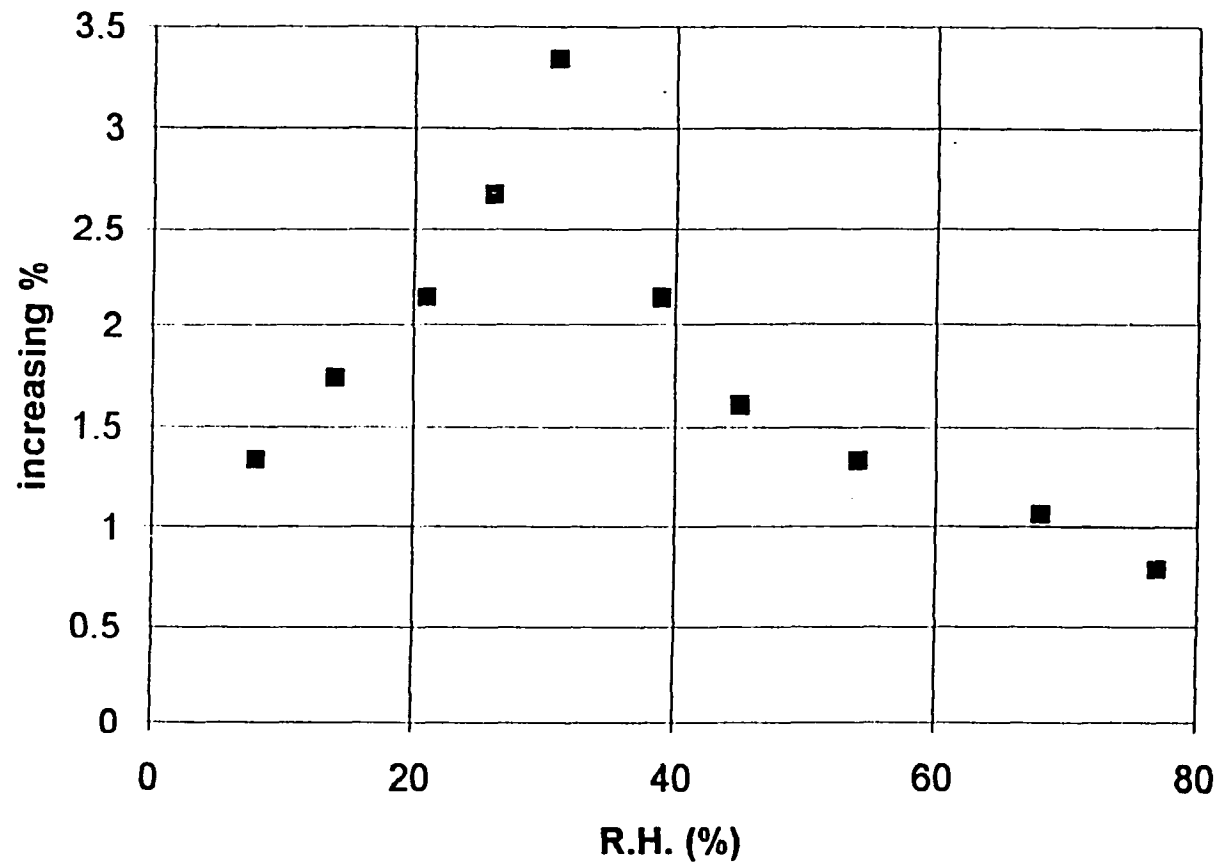


Figure 3.15 Freezing bed with increased relative humidity,
44µm w.p. glass beads, AC-3Hz-3kV, p-p

3.2.4 Bed expansion and freezing

Figure 3.16 gives the bed expansion and freezing curve for the FCC (2-A) powder, flowing with Ar under different electric field strengths and frequencies at a constant R.H. (10%) and temperature (25 °C). The bed initially expanded with the increase of the electric field. Further increase in the electric field seized and contracted the bed. A peak frequency in the bed expansion was found to occur in this experiment at 1 Hz. The bed froze easily with the sticky particles whose van der Waals force was strong, such as FCC (1-B) and FCC (3-A). The additional electric force made the fluidization worse.

3.3 Elutriation

3.3.1 Beam attenuation theory

Laser beam attenuation was used to determine the concentration of fines in the freeboard of the fluidized bed. The Lambert-Beer law (Liu and Colver, 1989) was,

$$\frac{I}{I_0} = e^{\left[-\frac{\pi}{4} Q_{ext} d^3\right]} \quad (3.15)$$

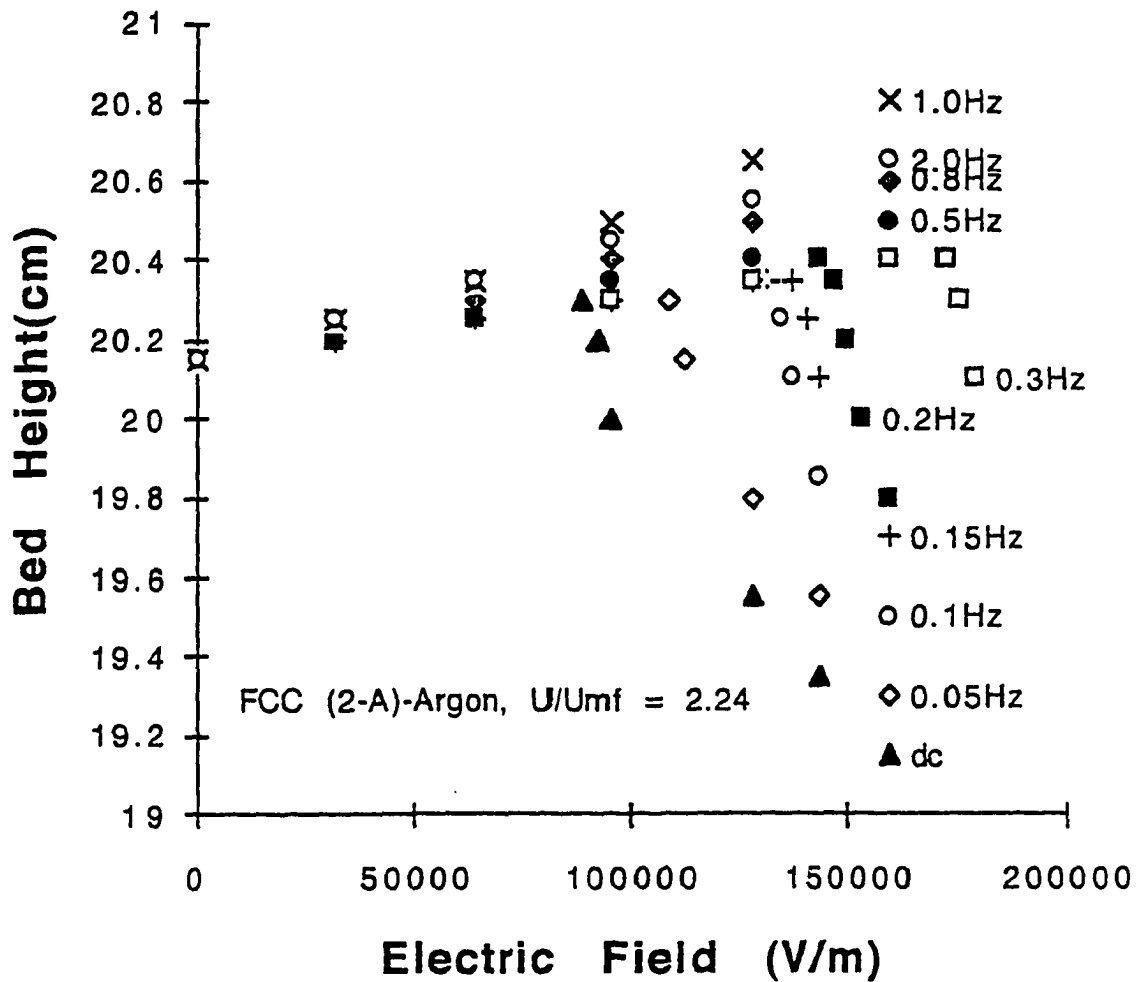


Figure 3.16 Frequency effect on bed expansion/contraction at various electric field strength, FCC 2-A with Argon, $U/U_{mf}=2.24$, 24°C , AC p-p

The Mie theory gives $Q_{\text{ext}}=2$ for particles larger than approximately $10\mu\text{m}$. I is the laser intensity with elutriation, I_0 is the laser intensity without elutriation, and x was the distance across the fluidized bed (close to the diameter of the bed). The elutriation constant (k_i) is defined through the mass relationships for particles in the bed (Kunii and Levenspiel, 1991)

$$-\frac{dM_i}{dt} = A_t k_i^* \left(\frac{M_i}{M} \right) \quad (3.16)$$

and

$$k_i^* = \frac{k_i}{A_t} M \quad (3.17)$$

where M_i , M , A_t , and k_i were the instantaneous mass of the fines, and the mass of the bed, the cross section of the bed, and the elutriation constant of size i , respectively. The mass flux of particles above the bed was related to the measured number density n_i of size i fines in the freeboard and the superficial velocity (assuming there was no slip or constant slip condition between the fluid and fines) by the following relationship

$$\dot{m}_i = \left| \frac{dM_i}{A_t dt} \right| = n_i m_{pi} U_s \quad (3.18)$$

where n_i , m_{pi} , and U_s were the particle number density of size i , particle mass of i , and particle (or slip) velocity, respectively. Solving Eqns. 3.16, 3.17, and 3.18 showed that a plot of the log of the number density with time gives the elutriation constant from the negative slope of the line for a batch process in which the total mass (M) of the bed did not change appreciably over the test.

$$\ln(n_i) = -\left(\frac{k_i' A_i}{M}\right)t + \ln\left(\frac{k_i' M_{i0}}{M m_{pi} U_s}\right) \quad (3.19)$$

where M_{i0} was the total mass of fines in the bed that would be elutriated in an infinite time, that was

$$M_{i0} = M_{i0}(E) \quad (3.20)$$

where E was the electric field strength in the bed. Thus the second term on the right hand side of Eqn. 3.19 was a constant and a function of E . It was assumed that the average particle diameter of fines was the Waddel diameter of the collected fines and the concentration of fines was smoothly distributed across the cross section of the bed (Colver and Wang, June, 1993). Since the diameter distribution of the elutriated fines would vary with the gas velocity the fines had to be collected in order to determine the Waddel diameter of each

velocity. Fig.3.17 showed the particle diameter distribution for different velocities (7.60 cm/s, 11.40 cm/s, 14.67 cm/s, and 17.47 cm/s). The average Waddel diameters of elutriated fines were 8.18 μm , 9.44 μm , 10.63 μm , and 11.52 μm , respectively. The elutriation constant calculated by the laser-attenuation method represented the average elutriation constant of fines. Fig.3.18 compared the experimental data with the results calculated using the correlation developed by Merrick and Highley, and by Geldart et al. (Kunii and Levenspiel, 1991). There was an agreement between the correlation and the range of experimental data. The advantage of using the laser attenuation method was that Eqn.3.15 could be put into Eqn.3.19 for the n_i term. Therefore, only the M, A, and I/I_0 (with time) were required to calculate the average elutriation constant. Therefore, it was not necessary to know the diameter of fines.

3.3.2 Elutriation constant with electric field

Figure 3.19 gives the elutriation constant (K_i) vs. the distance between the free surface of the bed and the top of the electrode in the Pyrex bed. The electrode was attached to

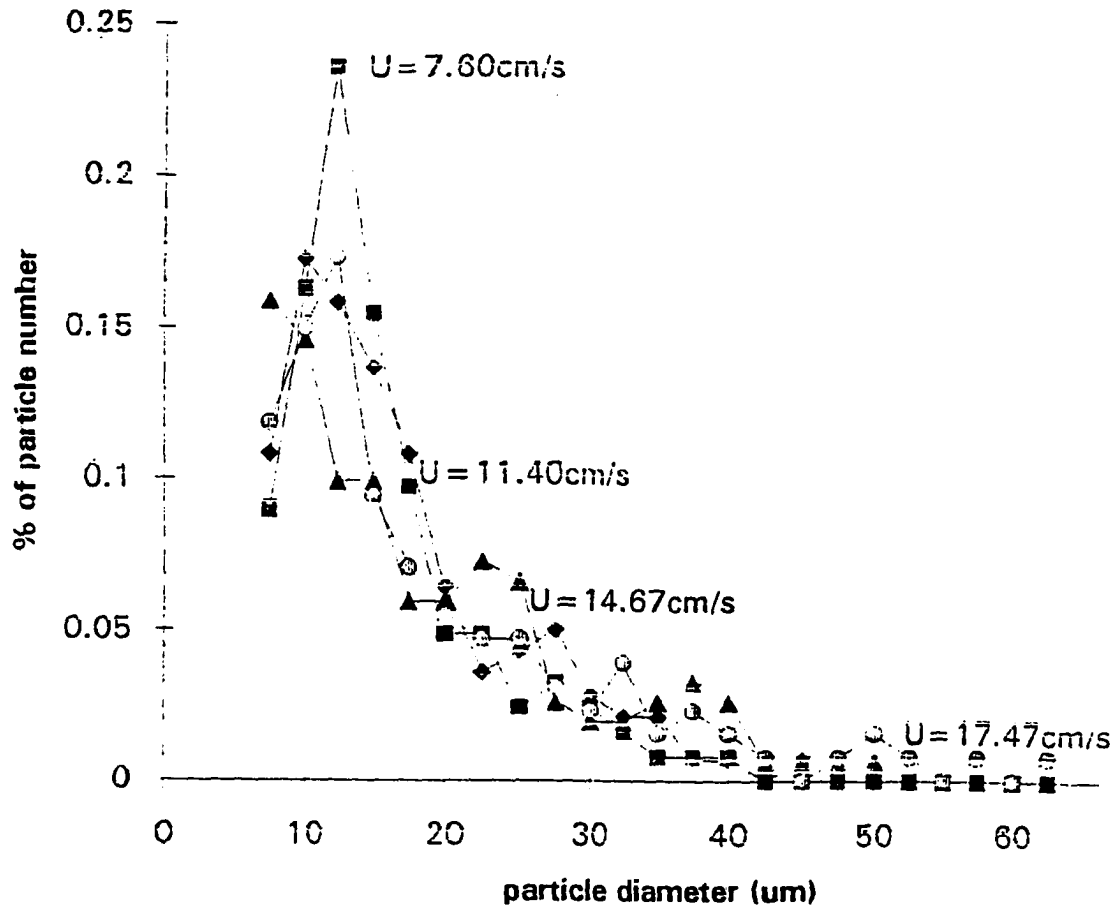


Figure 3.17 Size distribution of elutriated sand fines at various superficial velocity

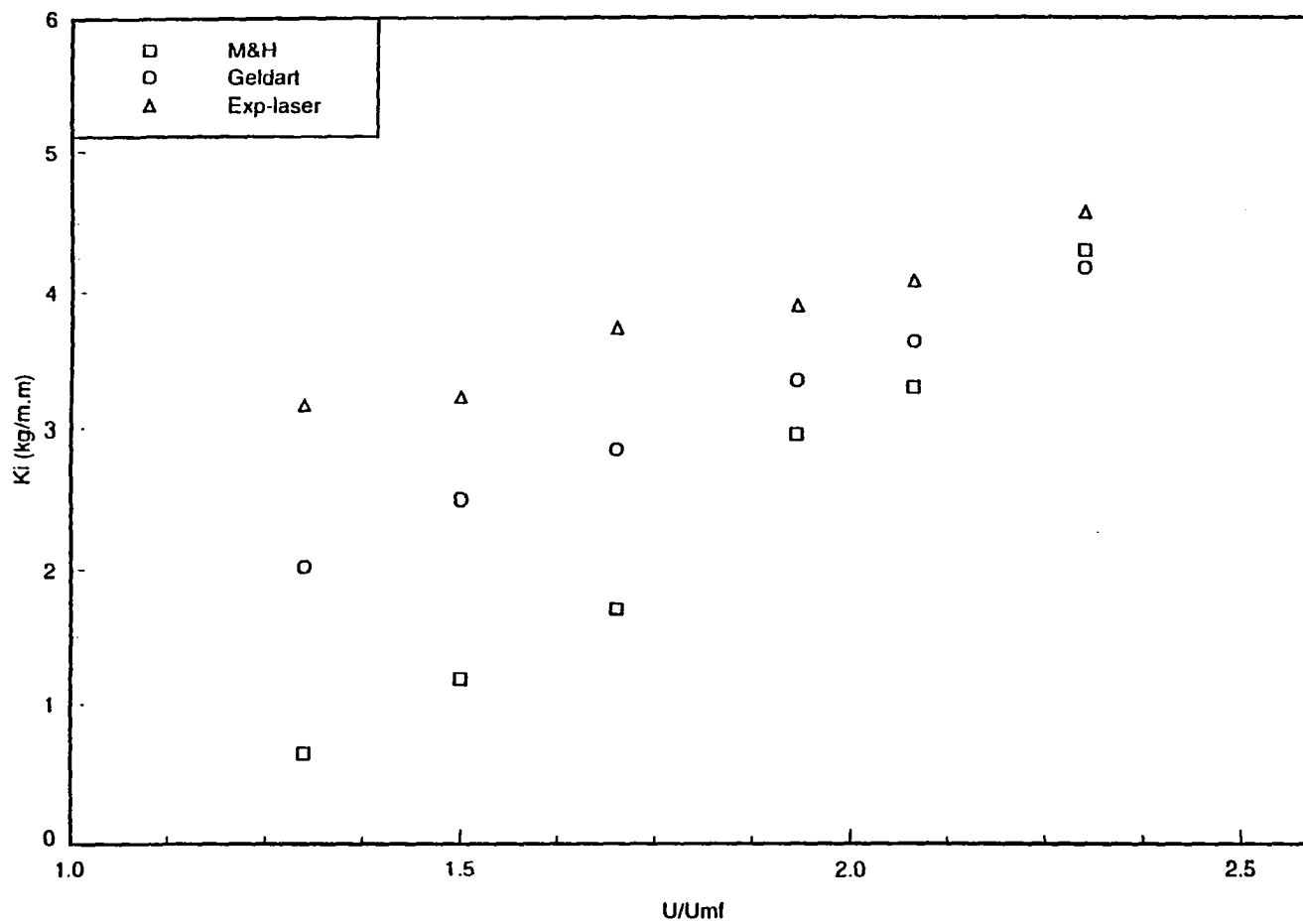


Figure 3.18 Comparison of elutriation constant calculated using correlation from Merrik & Highley and Geldart with result from Laser-beam method

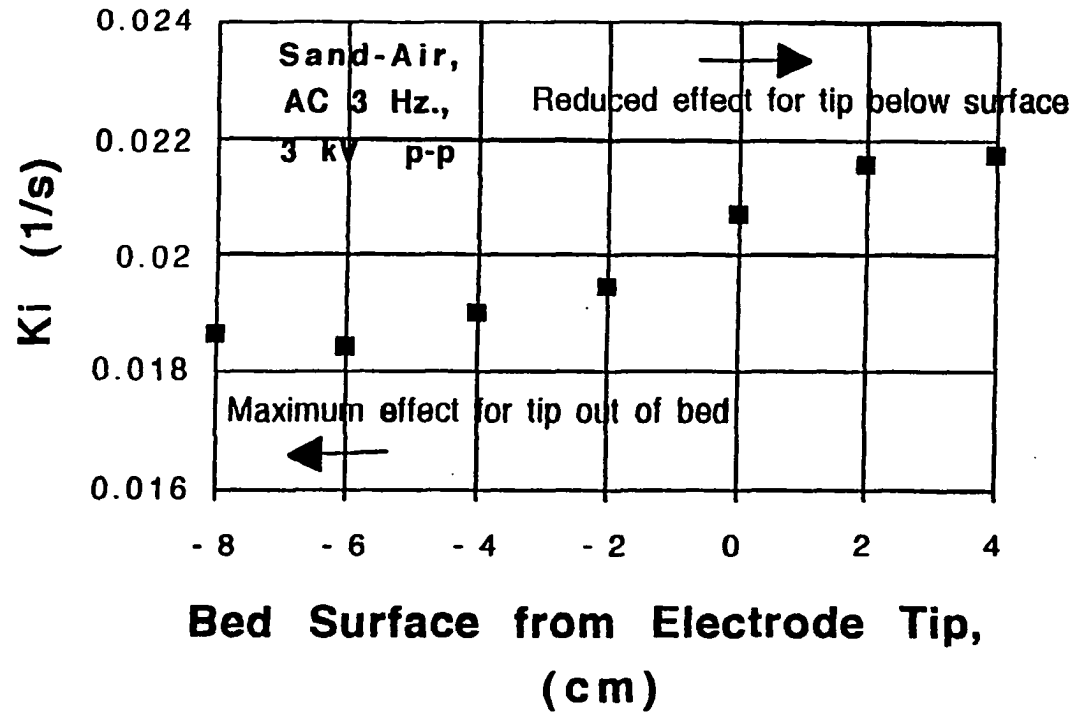


Figure 3.19 Elutriation constant at different electrode height (inserted from distributor), $U/U_{mf}=2.24$

the distributor. The negative sign indicated that the surface of the bed was lower than the top of the electrode. Results confirmed that the control of the elutriation was due to the electric field and not the precipitation in the freeboard of the bed.

The effect of electric field strength on the elutriation constant taken from the Pyrex bed (Fig.2.1) with the stopwatch is shown in Fig.3.20. Increasing the electric strength decreased the elutriation constant. In Figs.3.20 and 3.21, the correlations are

$$\text{DC: } K_i = 0.02732 - 0.01748xE(\text{kV/m}) \quad (3.20)$$

$$\text{AC: } K_i = 0.02688 - 0.01435xE(\text{kV/m}) \quad (3.21)$$

where AC was 3 Hz p-p. Comparing the result from the copper bed (Fig.2.4), in which $K_i = 0.0166 - 0.02098xE(\text{kV/m})$ for the DC case, good agreement is shown. The effect of electric field strength on various velocity with and without an electric field is also shown in Fig.3.21. The slope of the decreasing elutriation constant for each velocity ratio was almost the same between the 0 kV and 3 kV case. The frequency effect on K_i is shown in Fig.3.22. The lowest value of K_i was found at 0.8 Hz. The trend of the curve is similar to the frequency

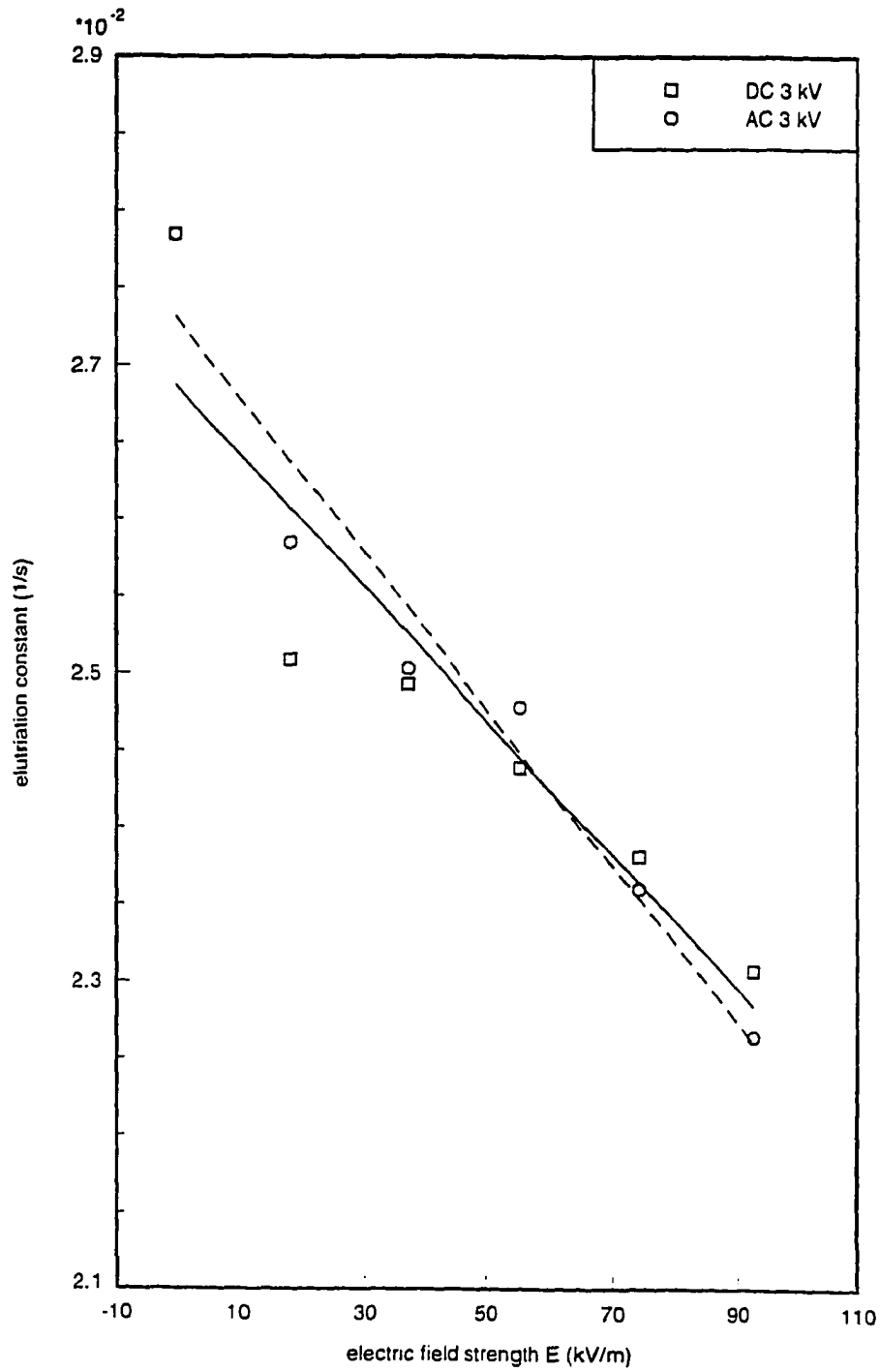


Figure 3.20 Elutriation constant of DC 3 kV and AC p-p, 3 Hz, 3 kV electric field $U/U_{mf}=2.24$

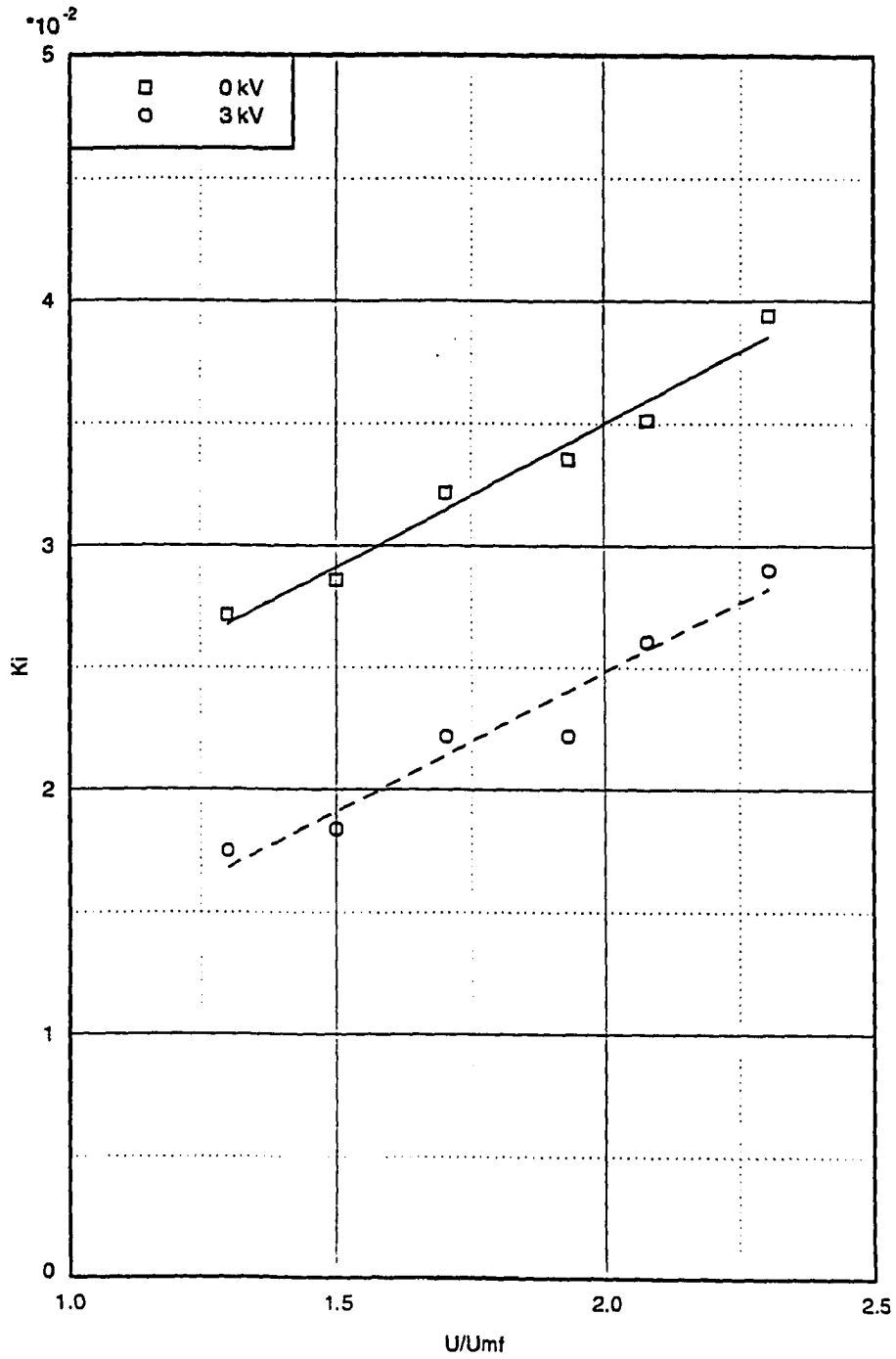


Figure 3.21 Elutriation constant of various velocity ratio with and without electric field (3 Hz, 3 kV, p-p)

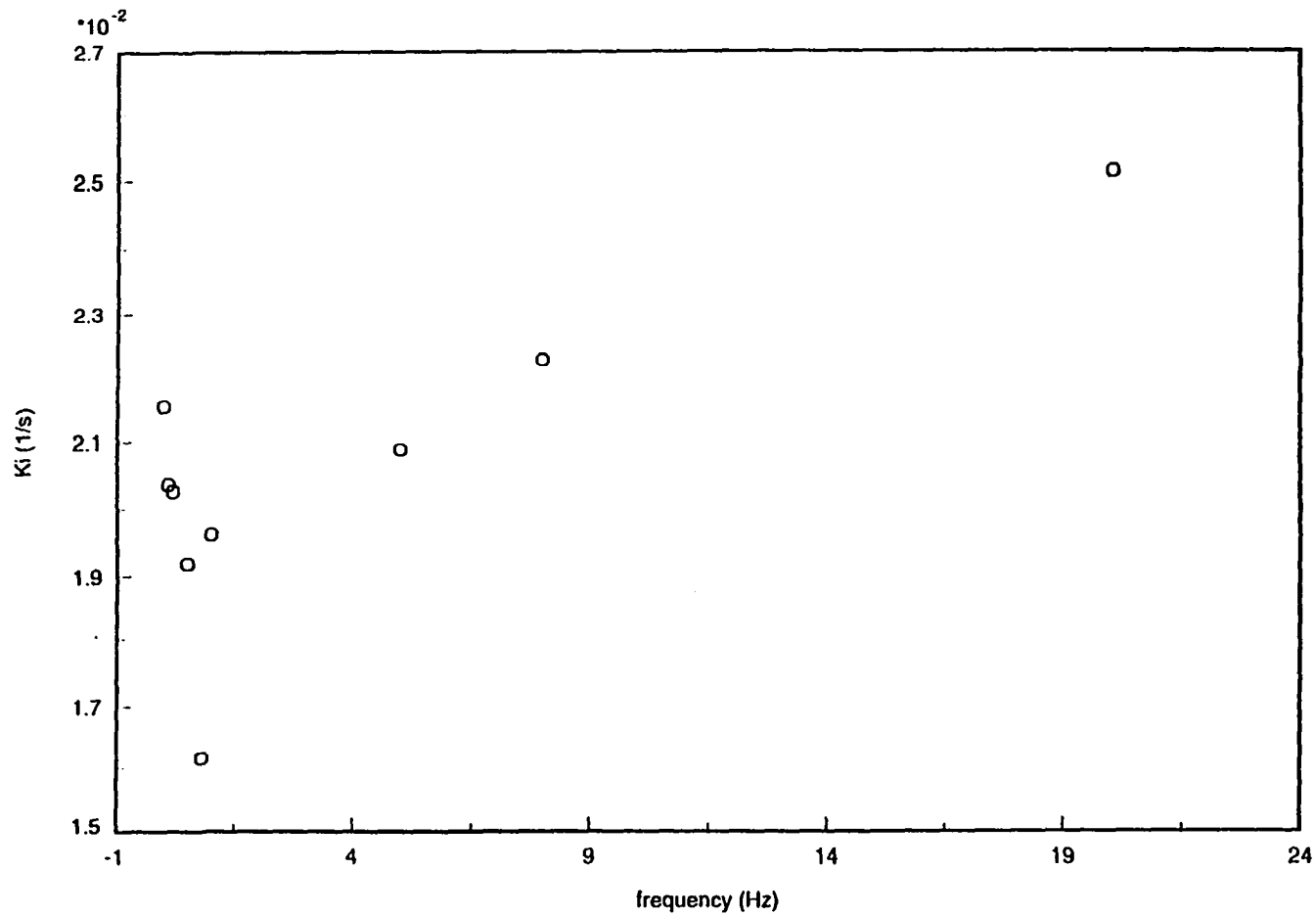


Figure 3.22 Elutriation constant versus frequency, AC-3kV peak-to-peak, $U/U_{mb}=1.5$, sand, $24^{\circ} C$, $U/U_{mf}=2.24$

effect on the bed expansion in Fig.3.13. The temperature effect for a DC electric field of 0 and 3 kV, and for an AC electric field of 0 and 3 kV, is shown in Fig.3.23, Fig.3.24, Fig.3.25, and Fig.3.26, respectively. Increasing the electric field strength was found to reduce the particle concentration at any given time, as did an increase in the temperature of the bed above room temperature to 255 °C. It can be concluded that

- Increasing the voltage increased the elutriation constant at a constant temperature of 255 °C; later data suggest the reverse trend occurred at a lower temperature (25 °C).
- Increasing the temperature had no effect on the elutriation constant (at a constant 0 kV voltage); this tended to be confirmed by later data.

The relaxation time was tested by switching the electric field momentarily on or off. The results were shown in Fig.3.27. In this test, the electric field relaxation was close to 15-30 seconds. The elutriation constant for different tests was summarized in Table 3.3.

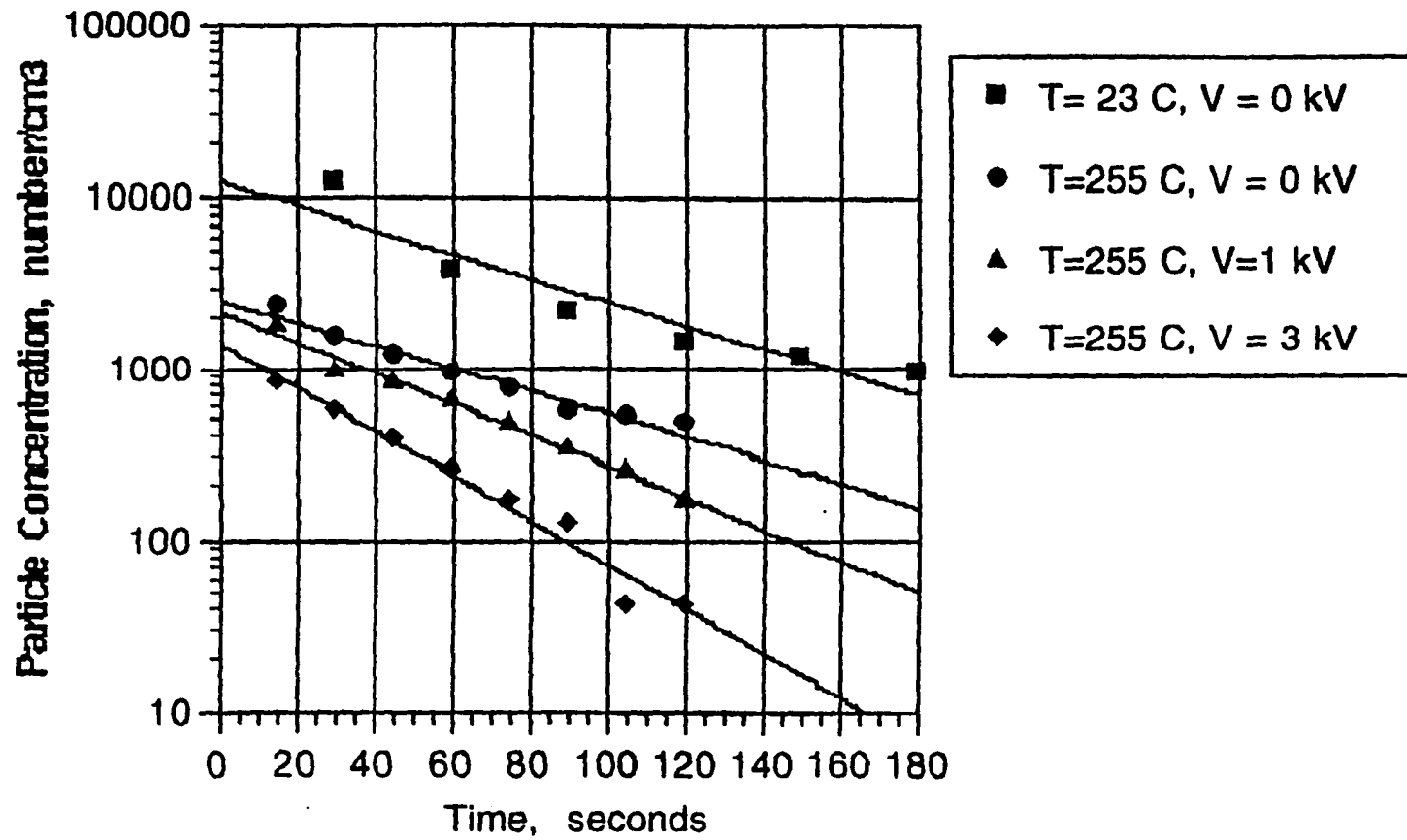


Figure 3.23 Particle concentration in freeboard with time,
 slope is a measure of elutriation constant
 $U/U_{mf}=2.24$

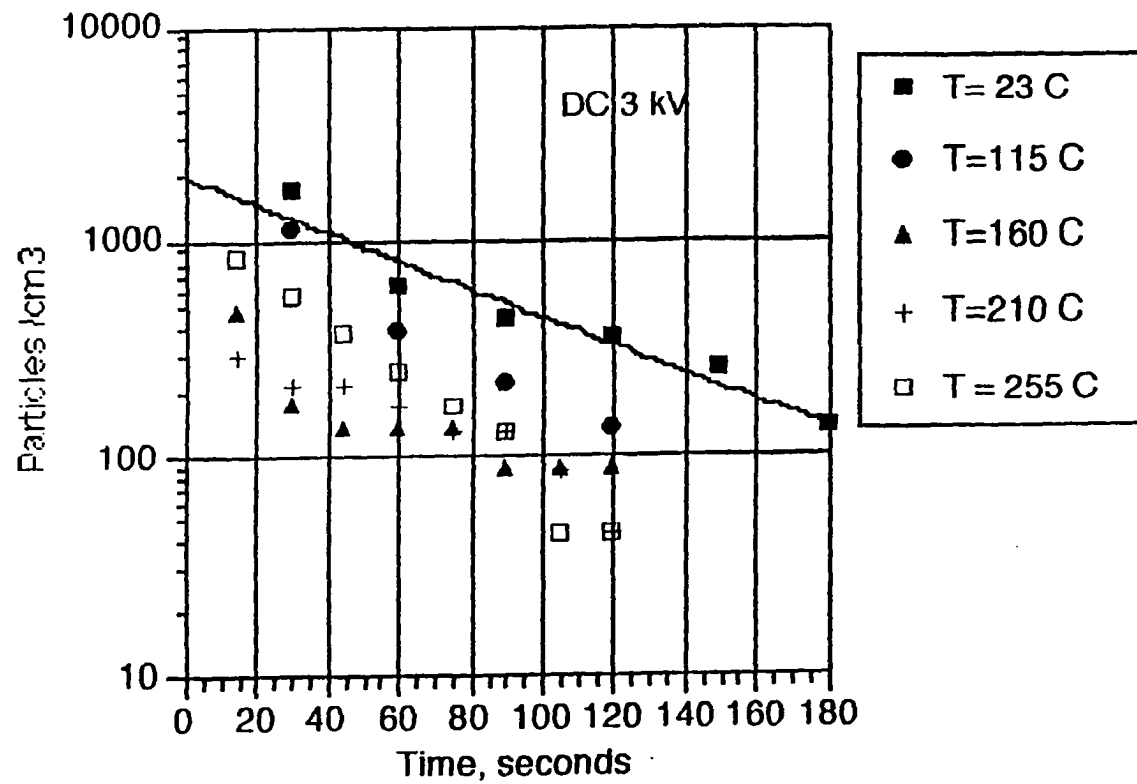


Figure 3.24 Particle concentration in freeboard with time at various temperature. DC-3kV, $U/U_{mf}=2.24$

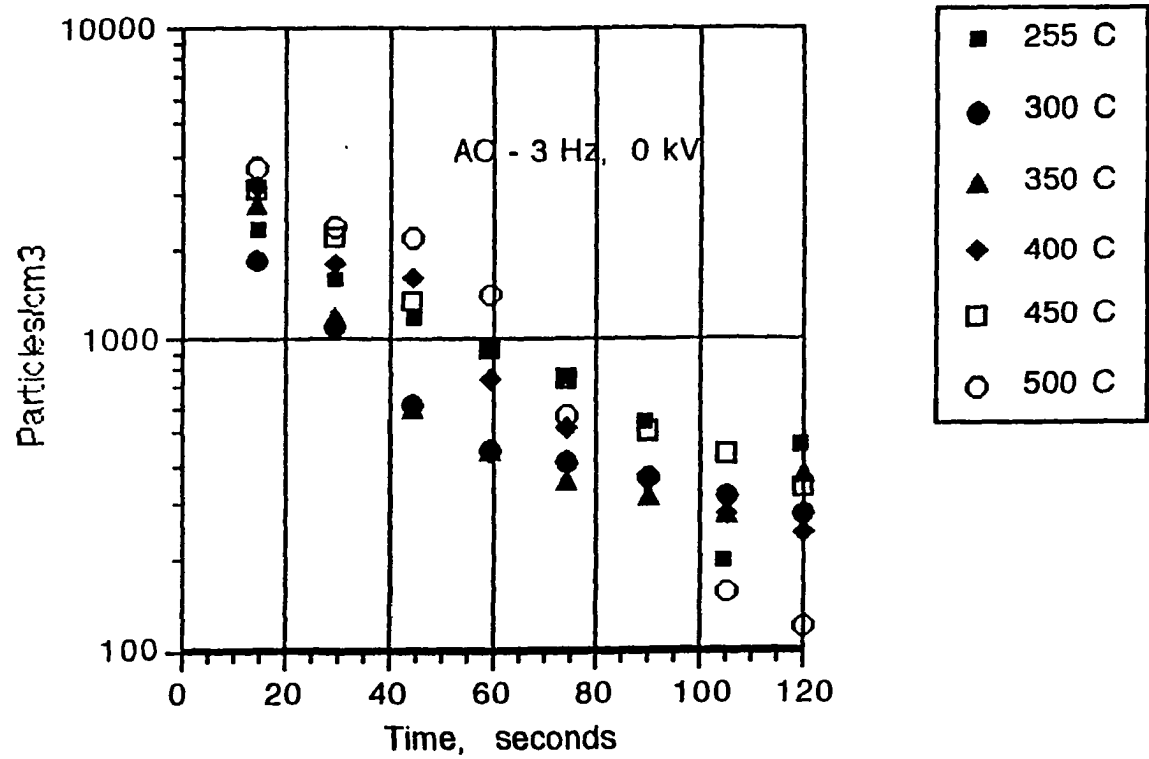


Figure 3.25 Particle concentration in freeboard with time at various temperature. 0kV, $U/U_{mE}=2.24$

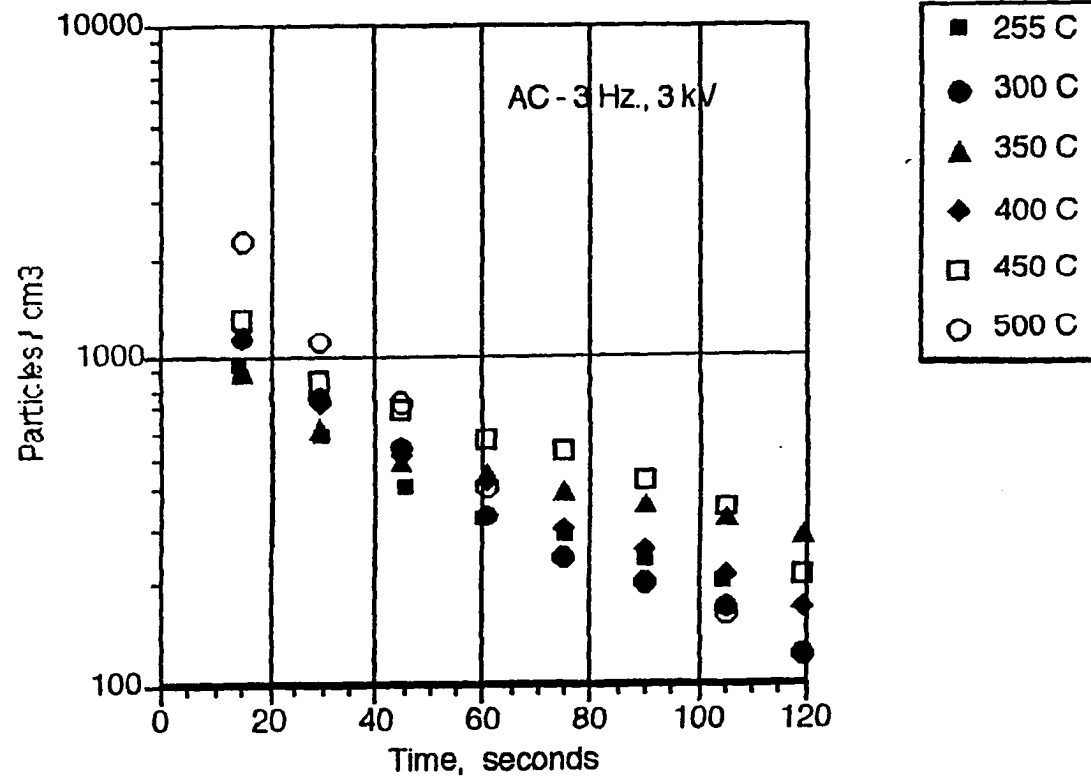


Figure 3.26 Particle concentration in freeboard with time at various temperature. AC-3Hz-3kV, $U/U_{mf}=2.24$

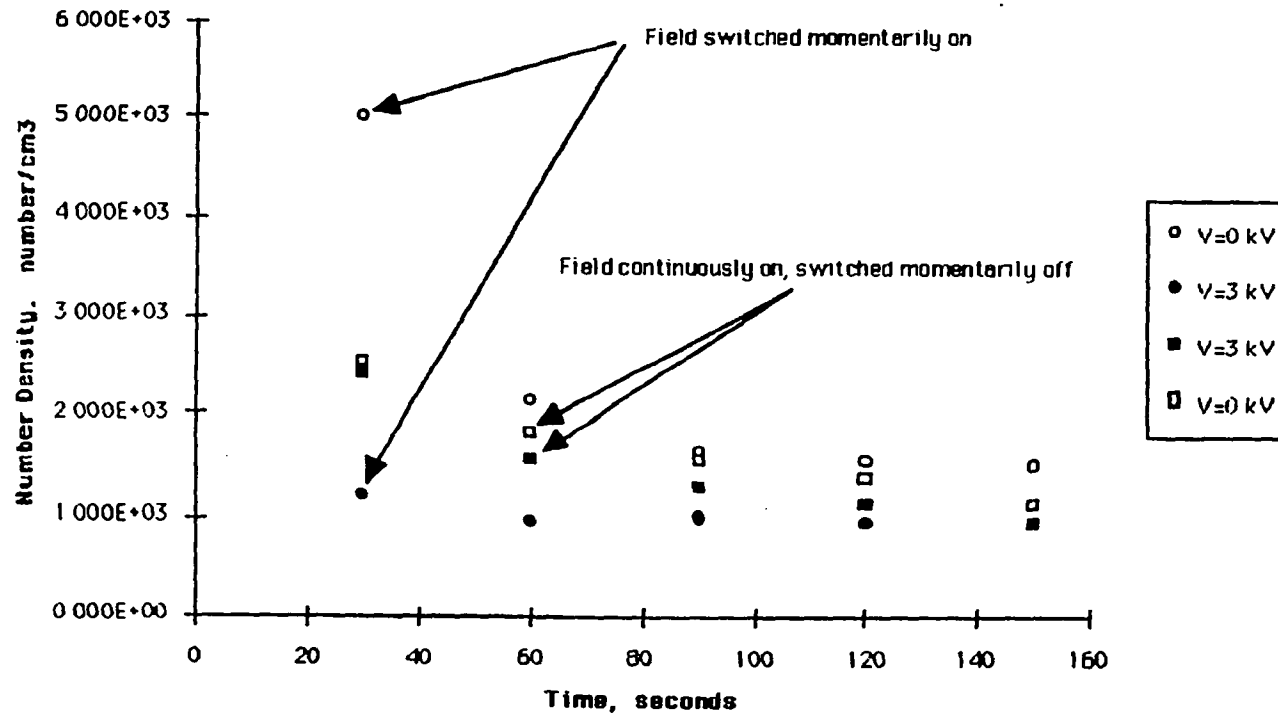


Figure 3.27 Particle concentration in freeboard with electric field momentarily off and momentarily on, 0 kV and 3 kV, AC, 3Hz, p-p, $U/U_{mf}=2.24$

Table 3.3 Elutriation constant at different temperatures with an electric field

	Temperature °C	elutriation constant K_i (1/s)
DC	23	0.01478
DC	115	0.02339
DC	160	0.01324
DC	210	0.01594
DC	255	0.02963
AC	255	0.01696
AC	300	0.02075
AC	350	0.00976
AC	400	0.01736
AC	450	0.01466
AC	500	0.02749

Sand, R.H.=9.8%, AC electric field 3 Hz and 3 kV p-p, DC electric field 3 kV, Air, Mass=614 gm, superficial velocity=10.6 cm/s.

3.3.3 Particle charge

The result of particle charge accumulated by using sand and 3 kV DC and p-p AC electric field was shown in Fig.3.28. It shows that the AC electric field reversed the charge sign. This result will be examined further.

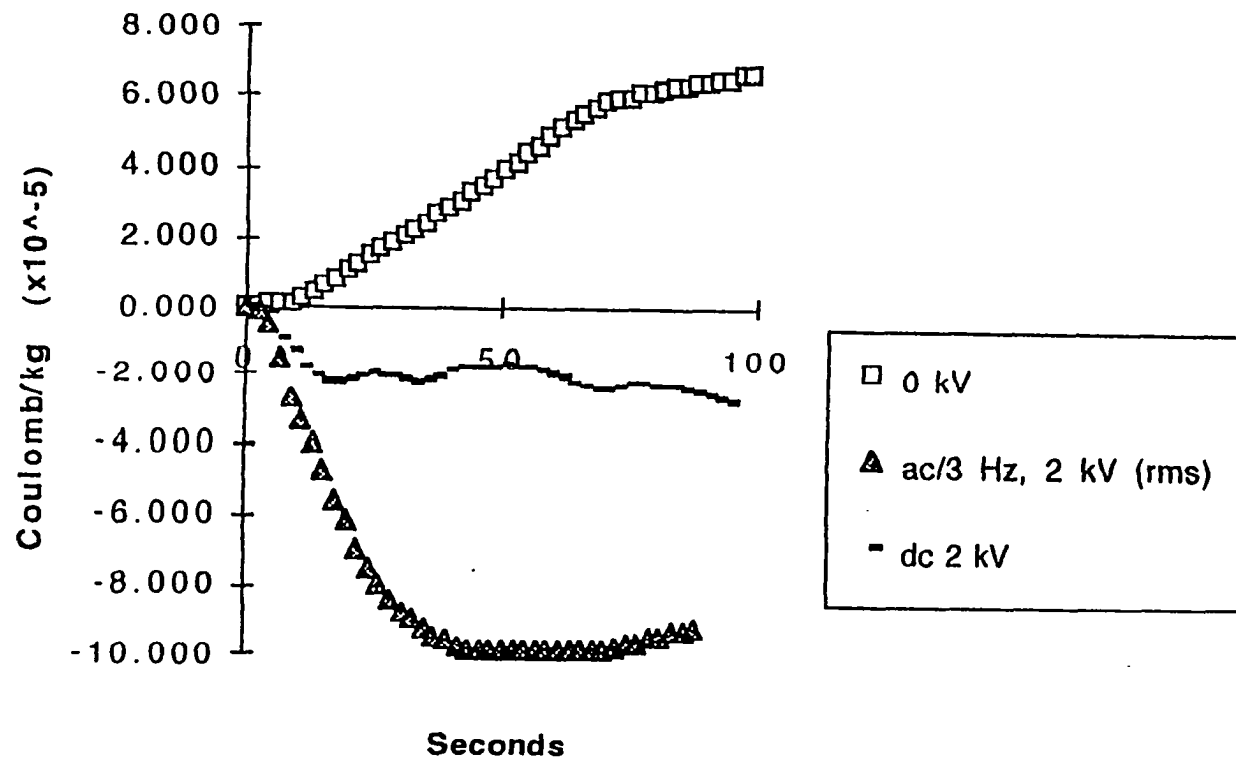


Figure 3.28 Charged elutriated fines with and without electric fields, $U/U_{mf}=2.24$, $d_p=8.66 \mu\text{m}$

3.4 Mapping the Electric Field

The effect of the electric field on the fluidized bed with Geldart A powders was shown in Fig.3.29. The increase of U_{mb} with an increase of the electric field indicated an expansion of the fluidized bed. The bubbling and no bubbling zones are separated as a function of the applied field strength. However, this behavior can be represented by a "process window" with the operation map, shown in Fig.3.30, for which three independent variables (superficial velocity, electric field strength, and field frequency) were reduced to two parameters utilizing similarity. For example, the dashed vertical in Fig.3.30 intersects the abscissa at any of an infinite number of combinations of electric field strengths and frequencies. Increasing the superficial velocity along the dashed line leads to particulate fluidization at point a for a large bed (negligible wall effect). Increasing the superficial velocity past c in a field-free bed leads to bubbling; however, with an electric field the bed undergoes an additional bubble-free expansion. With an increase in superficial velocity to d, bubbling returns to the bed,

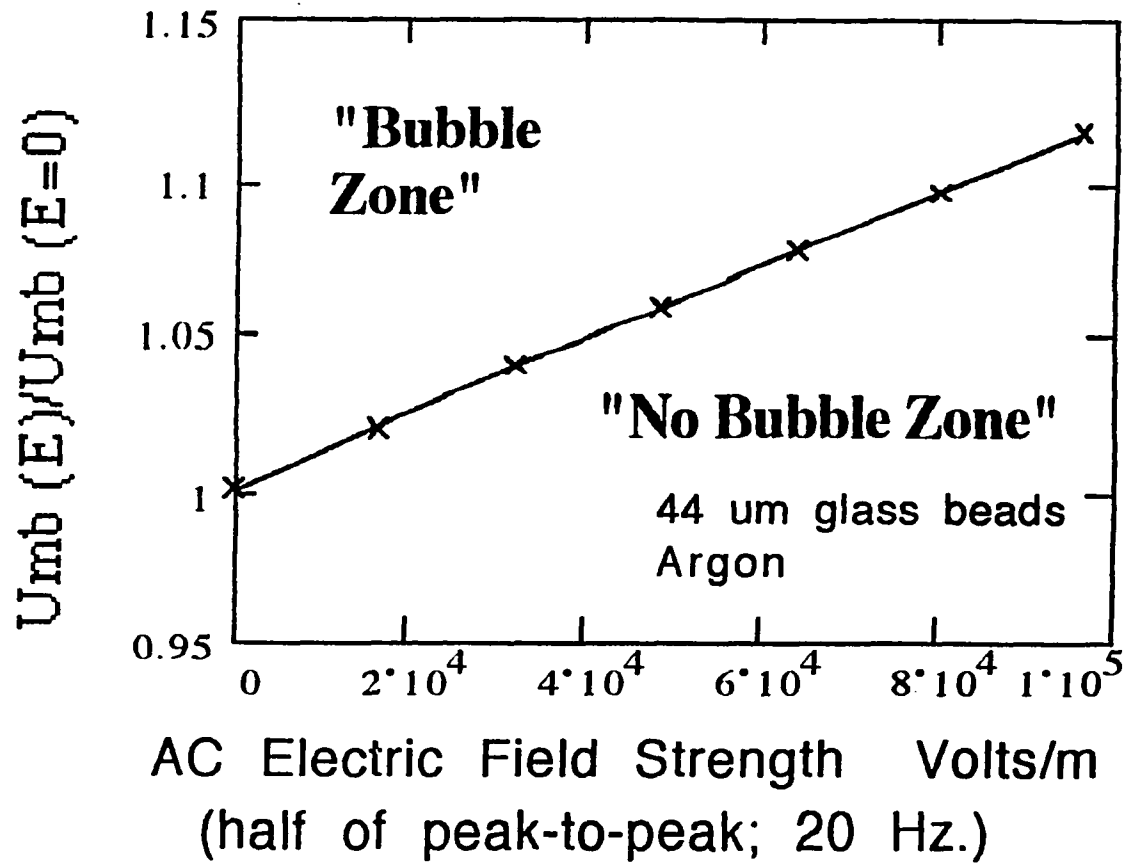


Figure 3.29 Bubble and no bubble zone for the bed with electric field, 44 μ m n.w.p. microbeads glass AC 20 Hz, half of p-p, Ar

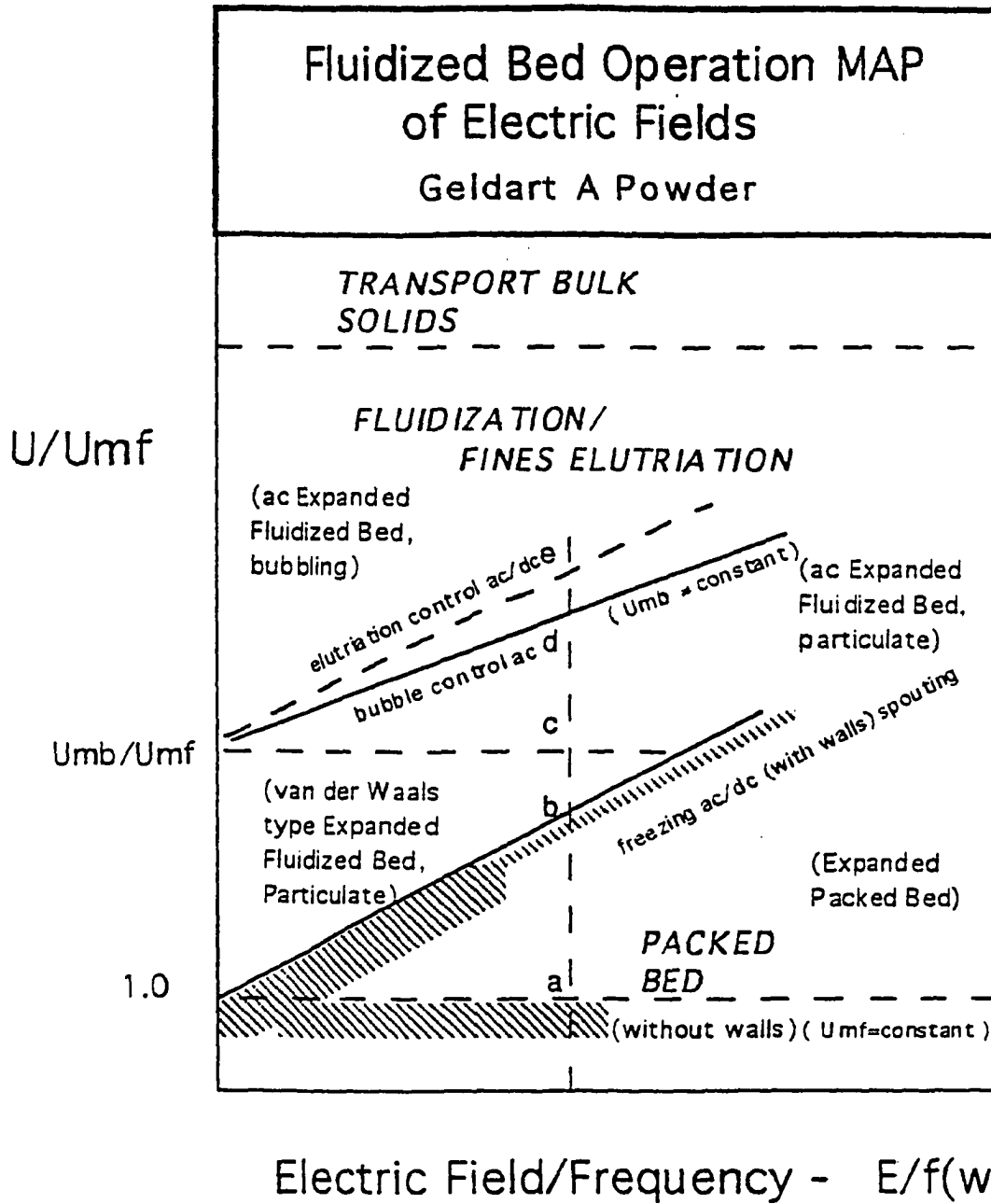


Figure 3.30 Map of electrofluidization with Geldart A powders

albeit at decreased intensity. Elutriation remains until e is reached with the onset of bubbling.

In summarizing the map, several observations for Geldart A powders can be made: (1) three independent variables—superficial velocity, electric field strength and frequency—combine to influence bubble formation and elutriation; (2) AC electric fields expand the bubble-free fluidizing zone by retarding the onset of fluidization (bed freezing) and delaying the onset of bubbling and increasing bed expansion; thus, new fluidized bed modes are attainable; (3) AC electric fields are better suited for bubble control than are DC fields; in other words, controlling U_{mb} can also freeze the bed; (4) DC fields are more effective in bed freezing applications and also can expand the bed with wall effects (small bed); (5) beds can be expanded first, and then frozen; and (6) elutriation and bubble control occurred simultaneously.

4. THEORETICAL STUDIES

A theoretical approach concentrated on the various forces acting on the particles. A study of these forces revealed information about how the fluidized bed behaves under the influence of an electric field. Table 4.1 gives a list of the important particle forces. A comparison could be made between van der Waals, triboelectric (electronic) and gravitation type forces with the electrostatically induced forces of induction and current constriction. The van der Waals and triboelectric forces are active in fine powders (Rietema, 1991) for field-free beds and must be overcome during the elutriation process or the bubble formation. To calculate these forces, some approximations were necessary. The first approximation made was that a triboelectric charge of 10^{-7} C/kg was distributed over particles of all sizes. The charge was assumed to be confined to the contacting surfaces of any individual particle within a fixed value of solid angle for all particle sizes. The second approximation was that the effective contact separation distance for van der Waals and triboelectric forces was taken to be 2.23×10^{-10} m

Table 4.1 Various paricle/interparticle force equations of interest

Force Type	Equation	Comments
van der Waals	$F_{vdw} = 0.75 \frac{Ad}{12z^2}$	sphere-plane; Rietema, 1991
Current Constriction (I)	$F_{J-DC} = 0.415\pi\epsilon_{em/o}d_p^2E_{max}^{0.8}E_o^{1.2}$	sphere-sphere; semi-emperical; fluidized bed, Dietz & Melcher, 1978
Current Constriction (II)	$F_{J-DC} = 2.165\pi\epsilon_{em/o}d_p^2E_{max}^{1.344}E_o^{0.656}$	sphere-sphere; semi-emperical; packed bed, Colver 1980; (rearranged to Zietz form)
Electric Field Induction	$F_{J-DC} = 1.37\pi\epsilon_{em/o}d_p^2E_o^2$	sphere-plane; (theoretical for conducting particle); Lebedev and Skal'skaya, 1962
Triboelectric (or Electrostatic contact)	$F_d = \frac{\epsilon_{ano}}{2} \left(\frac{\phi}{z}\right)^2 A = \frac{\pi(\phi)}{3z} \rho q \frac{d_p \Gamma\left(1+\frac{3}{n}\right)}{\Gamma\left(1+\frac{2}{n}\right)} d^2$	sphere-plane, Krupp, 1962, (adjusted here for distribution of average charge q over all particles in a Rossin-Ramler distribution)
Gravity	$F_g = \rho_p \frac{\pi d_p^3}{6} g$	single paricle

Data: $A=10^{-19}$ J; $\phi=0.5$ V; $z=2.23 \times 10^{-9}$ m & 2.23×10^{-10} m; $d=0.02$ μ m (=asperity diameter for lower limit of van der waals force); $q=2 \times 10^{-7}$ C/kg; $n=1.307$; $r_{ref}=9 \mu$ m; $E_{max}=30$ kV/cm; $E_o=0.79$ kV/cm; $\rho=2.4$ kg/m³; $d_{ref}=9 \mu$ m; $n=1.31$; and Γ is the gamma function.

and 2.23×10^{-9} m, respectively, for the upper limit forces (i.e., smooth surface particles); whereas the lower limit forces were calculated from an assumed surface asperity radius of $0.01 \mu\text{m}$ (i.e., microscopically rough surface). Finally, the AC field-induced forces were calculated from experimental results at a modest electric field strength of 0.79 kV/cm , a value that was shown to give good AC elutriation control for sand fines at 3 Hz .

Ordinary sand fines from the elutriation test were used as the material for the following calculations. The Rossin-Rammler-Bennet size distribution of the elutriated fines of river sand was calculated as

$$\xi = 1 - \exp \left[- \left(\frac{d(\mu\text{m})}{9} \right)^{1.300} \right] \quad 3.67 < d < 32 \mu\text{m} \quad (4.1)$$

where ξ was the cumulative fraction of all particles up to diameter d . Eqn.4.1 was used in the triboelectric charge calculation. Fig.4.1 and Fig.4.2 show the results of the particle forces for the different effective contact separation distance of 2.23×10^{-10} m and 2.23×10^{-9} m, respectively. The assumed smooth surface model for the van der Waals force (upper limit in Figs.4.1 and 4.2) was

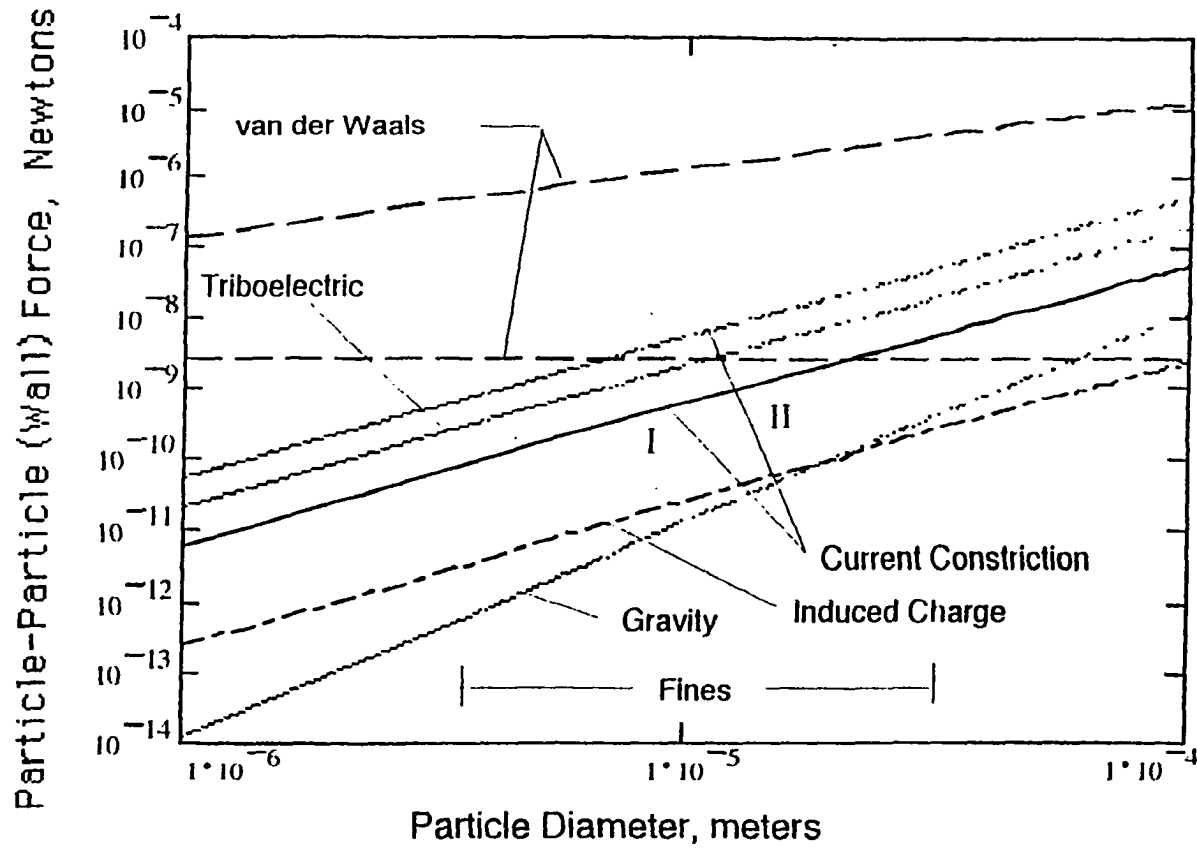


Figure 4.1 Comparison of various particle-particle (wall) in fluidized bed versus particle diameter for effect contact separation 2.23×10^{-10} m

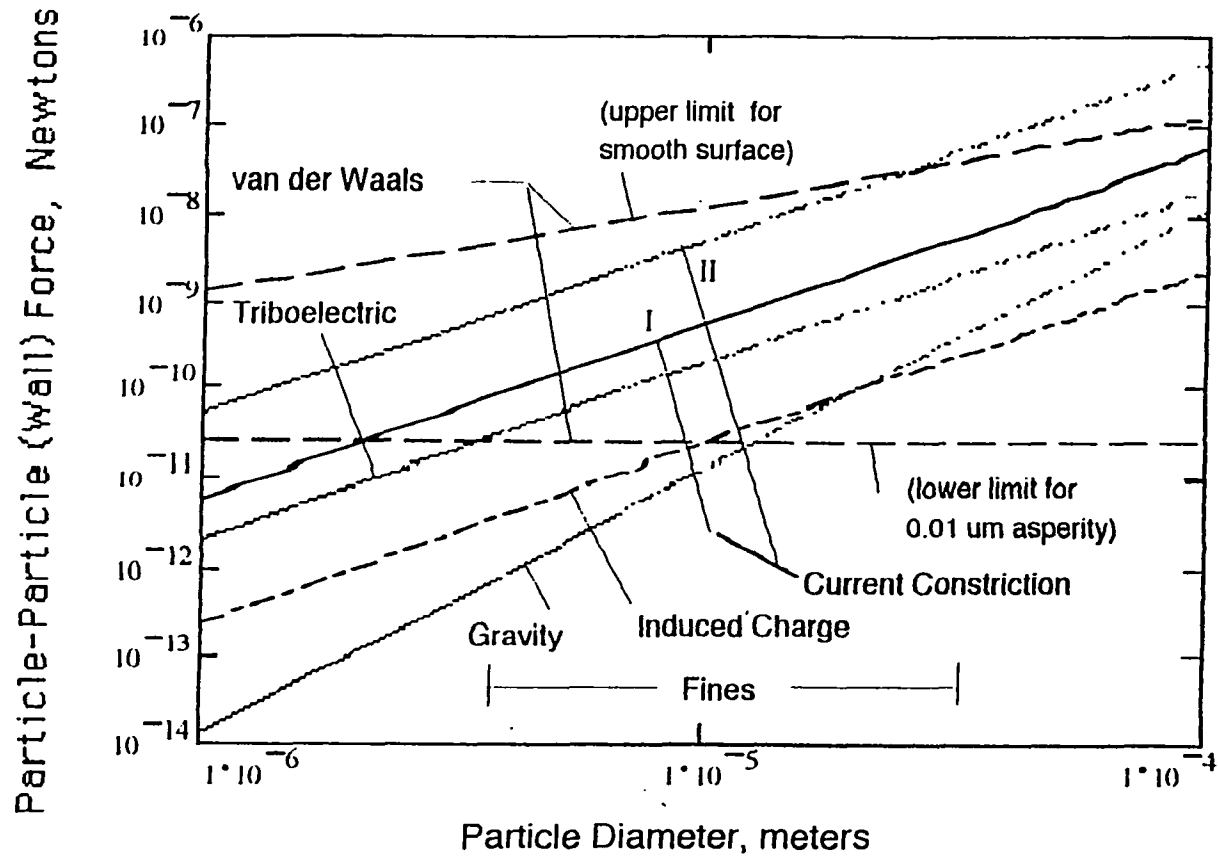


Figure 4.2 Comparison of various particle-particle (wall) in fluidized bed versus particle diameter for effect contact separation 2.23×10^{-9} m

observed to give unrealistically large cohesion forces. This was apparent when the van der Waals and the gravitational forces were made equal in Fig.4.1 (or Fig.4.2), in which case particles of 4000 μm (or 400 μm) could remain attached against the force of gravity. Therefore, it was concluded that the lower limit van der Waals force (i.e., the rough surface model (0.01 μm)) was more acceptable for the calculations. In this case, only the smaller particles of 60 μm (or 13 μm) were calculated to remain attached against the gravitational force.

Figure 4.2 shows that the current constriction forces (I or II) are comparable or could exceed all other forms of adhesion forces. In contrast, the electric field induced charge force was seen only to dominate over the van der Waals force for a portion of the upper size range of the fines greater than approximately 10 μm . In Fig.4.1, the permanent forces increased due to the assumption of closer particle contact where the type I electrostatic forces dominated over the van der Waals, but not the triboelectric forces, for

particle diameters greater than 20 μm , and type II electrostatic forces dominated above diameters of 7 μm .

It can be concluded that the electric current constriction forces, I or II, are the effective forces for both elutriation and bubble control. However, the preliminary experiment result from charge of elutriated fines was 1.0×10^{-4} C/kg, which was nearly three orders of magnitude larger than the above assumed value.

4.1 Extension of Davidson Model (DC)

An extension of the Davidson field-free model was proposed for the hydrodynamic behavior of bubbles formed in the fluidized bed (Colver et al., Dec., 1992). In this model, a spherical bubble was assumed already to be formed in the bed. It was then postulated that electrostatic forces had to be of the same order of magnitude as the particle-fluid forces in order for effective control. For an incipiently fluidized bed, gravitational forces acting on the particles were balanced by the forces of fluid drag. In this regime ($U_{mf} < U < U_{mb}$), the applied electric field had little effect on the overall bed behavior except to induce oscillations if in

the case of an AC field. But in a bubbling bed ($U > U_{mb}$), the mechanism was different. Two bubble models would be incorporated; one for the fluid dynamics and another for the electrostatics. The well-known Davidson model was used for an isolated spherical bubble since it offered a closed form solution of the pressure distribution as well as distributions of fluid and particle velocity around the bubble. For the electrostatic model, the maximum electric field induced particle-particle force was determined by a similar spherical bubble. Bubble control was postulated to be effective when the maximum electrostatic forces became comparable to the maximum fluid dynamic forces. In the case of the hydrodynamic forces, only the electrostatic force was comparable.

The following assumptions and equations describe the Davidson bubble model (Davidson, Clift, and Harrison, 1985).

Assumptions:

- spherical bubble
 - incompressible flow for the particle and fluid phases
 - negligible particle-particle friction (potential flow of particle phase)
-

- pre-determined particle path around the spherical bubble
- uniform pressure inside the bubble
- incipient fluidization far from the bubble (constant pressure gradient)

The equations of motion to be solved were:

The particle continuity:

$$\bar{\nabla} \cdot \varepsilon \bar{v} = \varepsilon \bar{\nabla} \cdot \bar{v} = 0 \quad (4.2)$$

The fluid phase continuity:

$$\bar{\nabla} \cdot \varepsilon \mathbf{u} = \varepsilon \bar{\nabla} \cdot \mathbf{u} = 0 \quad (4.3)$$

The fluid phase momentum:

$$\bar{\nabla} P + \beta_0(\varepsilon)[\bar{u} - \bar{v}] = 0 \quad (4.4)$$

Only the solution for the pressure distribution was needed to determine the force on a particle from Eqn.4.4. The solution of the pressure distribution $P(r)$:

$$P = P_b - \beta_0(\varepsilon)u_0 \cos\theta \left(r - \frac{r_b^3}{r^2} \right) \quad (4.5)$$

where β_0 was the permeability constant, as in a Darcy law type expression for the drag on a particle such that $\beta_0 u_0$ was the pressure gradient $\partial p / \partial y$ (far from the bubble in the vertical direction), p_b was the pressure inside the bubble, r_b was the radius of the bubble, and u_0 was the relative

fluid/particle interstitial fluid velocity far from the bubble. A contour plot of lines of constant pressure gradient (magnitude) is shown in Fig.4.3.

It was obtained using Eqn.4.5 and the definition of ∇P . The maximum pressure gradient was found to be three times greater than the pressure gradient in the far field of the bubble (see Fig.4.4)

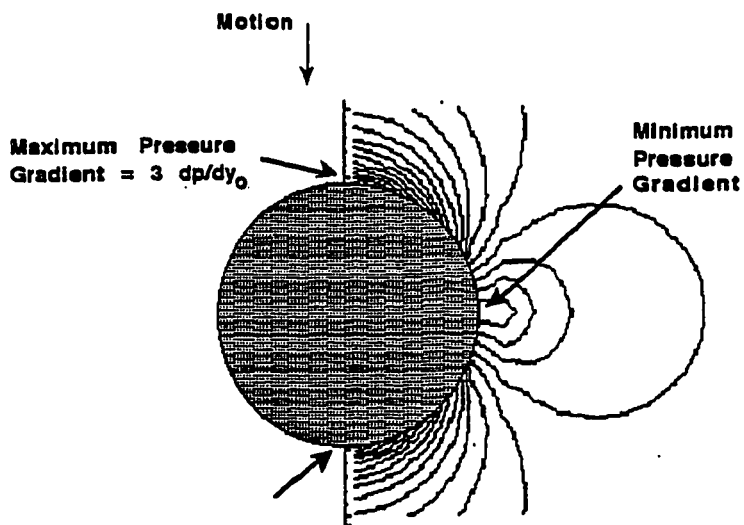


Figure 4.3 Contour plot of constant pressure gradient lines showing maximum pressure gradient on spherical bubble of unit radius

$$\left| \frac{dP}{dy} \right|_{\max} = 3 \left(\frac{\partial P}{\partial y} \right)_o \quad (4.6)$$

The following assumptions and equations were made for the proposed bubble model with electrostatics.

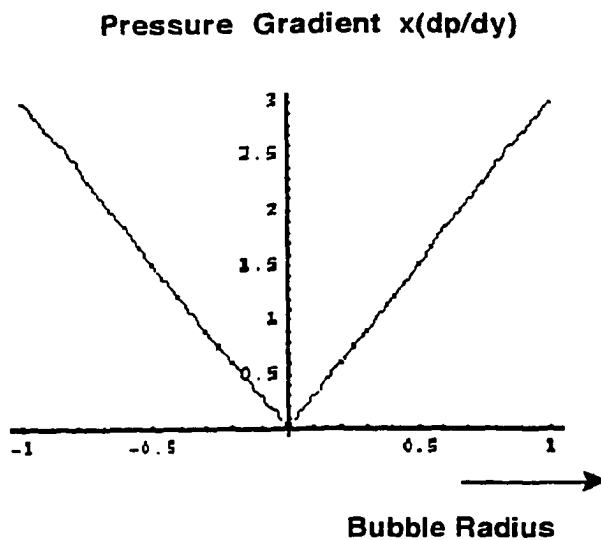


Figure 4.4 Pressure gradient on surface of bubble of unit radius (with the vertical z axis)

Assumptions:

- spherical bubble with field axial symmetry
- uniform electrical conductivity throughout the particle phase (infinite resistivity in the bubble region)

- constant DC (horizontal) electric field far from the bubble
- no free charge
- negligible polarization forces
- negligible magnetic field effect from the current in the bed

The equations of electricity were:

conservation of charge

$$\bar{\nabla} \cdot \bar{J} = 0 \quad (4.7)$$

Ohm's law

$$\bar{J} = \zeta \bar{E} \quad (4.8)$$

Definition of scalar potential

$$\bar{E} = -\bar{\nabla} \phi \quad (4.9)$$

Combining Eqns.4.7-4.9 led to the Laplace equation for constant electrical conductivity ζ outside the bubble as follows (Nayfeh and Brussel, 1985):

$$\nabla^2 \phi = 0 \quad (4.10)$$

The boundary conditions were: $\bar{J}_n = 0$ and $\bar{E}_n = 0$ at bubble interface. Therefore, the solution for the field potential, ϕ , was

$$\phi = -E_0 r \cos\theta \left[1 + \frac{r_b^3}{2r^3}\right] \quad (4.11)$$

The r and θ components of current around the bubble were

$$J_r = \zeta E_0 \cos\theta \left[1 - \frac{r_b^3}{r^3}\right] \quad (4.12)$$

$$J_\theta = -\zeta E_0 \sin\theta \left[1 + \frac{r_b^3}{2r^3}\right] \quad (4.13)$$

Fig.4.5 shows Eqns.4.12 and 4.13 as a vector field plot (the length of the arrow represents the relative magnitude of current density or electric field strength).

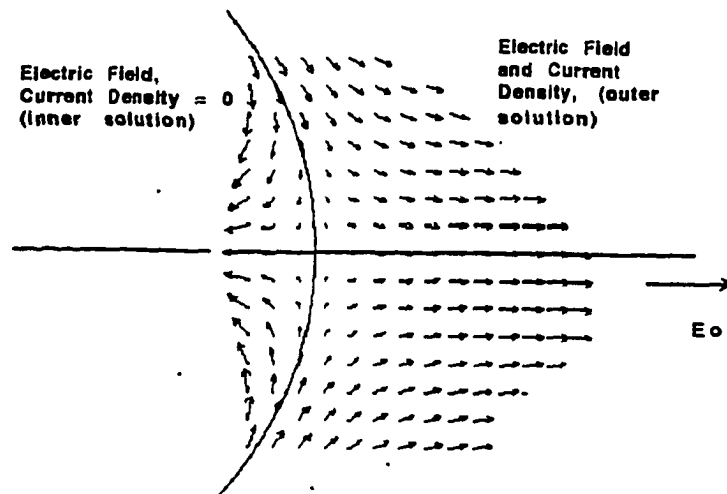


Figure 4.5 Vector field plot of current density magnitude and electric field strength near bubble ($\theta=0$), Current density inside bubble = 0

The current density is zero at the vertical surfaces of the bubble ($\theta=0,\pi$). Inside the bubble, the current was zero while the electric field strength wasn't zero. The tangential component of the electric field needed be continuous through the bubble interface since the free charge was zero. In the likely event of charged particles occurring at the bubble interface, the internal electric field would circulate these particles. Fig.4.6 shows the flow direction of the current around a bubble of unit radius.

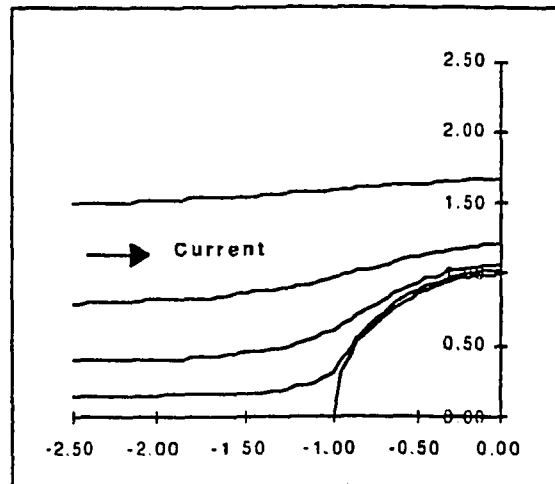


Figure 4.6 Lines of constant ψ showing current path and direction of electric field past bubble of unit radius (largest current concentration at the top of the bubble)

The current density reached its maximum value at the top and bottom of the bubble ($\theta=\pi/2, 3\pi/2$) and was zero at the sides ($\theta=0,\pi$). This meant that the particle-particle forces due to the current were greatest at the top and became zero at the sides of the bubble. As seen in the equations, the maximum current at the interface is 3/2 times the far field current.

The resulting relations for current density and electric field strengths with the far field J_0 and E_0 are

$$J_{\max} = \frac{3}{2}J_0 \quad (4.14)$$

$$E_{\max} = \frac{3}{2}E_0 \quad (4.15)$$

The criteria for bubble control was the ratio of the forces acting on the particles due to the electric field stresses and pressure gradient. This ratio is given as

$$\frac{F_{J-DC}}{F_{f\max}} = \frac{\left(\frac{F_{J-DC}}{d^2}\right)}{\nabla P_{\max}} \left[\frac{6(1-\epsilon)}{\epsilon\pi d} \right] \approx 1 \quad (4.16)$$

The following relationship could be obtained using Eqns.4.6, 4.8, 4.14, and 4.15, the relationship for the far field pressure gradient is

$$\left(\frac{\partial P}{\partial y}\right) = \rho_p(1-\epsilon)g \quad (4.17)$$

Substituting Eqn.4.17 into Eqn.4.16 gives the criteria for bubble control as (Colver and Wang, June, 1993)

$$\frac{F_{J-DC}}{F_f} = \frac{2K_a K_b}{\epsilon(U)\rho_p \pi d g} \left(\frac{3}{2} K_c E_o\right)^\beta \approx 1 \quad (4.18)$$

where the voidage, $\epsilon(U)$, can be found using the Richardson-Zaki equation given in Eqn.3.14. The n and u_s' in Eqn.3.14 can be found from the experimental data.

As a numerical example, consider the Microbeads glass spheres which had the following values: $K_a = \epsilon_{em,o} = 8.85 \times 10^{-12}$, $K_b = \epsilon_{em} / \epsilon_{em,o} = 7.0$, $K_c = 1$ (typically 1-20), $\beta = 2$ (typically 1-2), $\rho_p = 2500 \text{ kg.m}^{-3}$, $g = 9.81 \text{ m.s}^{-2}$, and $d = 62 \mu\text{m}$. From the above equations, the far field strength was calculated to be $E_o = 1.8 \times 10^5 \text{ V/m}$ for bubble control in the fluidized bed. This value was typical of the field strength required for bubble control as measured in the experiment.

Assuming that only the current constriction force was important in the DC electric field, then the force equation which was given by Dietz and Melcher (AIChE Symp., 1978) is

$$F_{J-DC} = K4\pi\epsilon_{em,o} d^2 E_{max}^\gamma E^{2-\gamma} \quad (4.19)$$

where K and γ ($=0 \rightarrow 2$) were experimentally or theoretically derived constants, and $\epsilon_{em,o}$, d , E_{max} , and E were the permittivity of free space, the particle diameter, the breakdown electric field strength between particle contacts, and the average electric field strength in the bed, respectively. Dietz and Melcher (1980) found that $K=0.1$, $\gamma=0.8$ and $E_{max}=30$ kV/cm. From the result of scaling-up parameters (see section 4.4), a further relation can be written as

$$\gamma = 2 - \frac{1}{n} \quad (4.20)$$

where n was a constant of the Richardson-Zaki equation. By substituting Eqn.4.20 into Eqn.4.19, Eqn.4.18 is rewritten as

$$\frac{8K\epsilon_{em,o} E_{max}^{2-\frac{1}{n}} \left(\frac{3}{2} E_o\right)^{\frac{1}{n}}}{\epsilon(U)d\rho_p g} \geq 0(i) \quad (4.21)$$

Eqn.4.21 implies that increasing the superficial velocity, particle diameter, and particle density leads to an increase in the required electric field strength in the far field (E_o) in order to suppress bubbles. These predictions are consistent with experimental results.

4.2 AC Electrical Field Model

A model describing the inter-particle forces with an AC field has been studied. Fig.4.7 shows the two particle model: The capacitance (C_c) between the two particles was determined in large part from the close separation distance of the surfaces, as can be seen from the definition of capacitance (i.e., $C \approx \epsilon_{em}A/x$, where x is the separation distance and A was some appropriate effective area). For AC fields, inter-particle forces would exist between two particles, even if the particles are separated and the contact resistance is infinitely large because of the mutual capacitance. This is in contrast to the usual DC current-related electrostatic particle forces listed in Table 4.1, where electrical contact between the particles was assumed. Thus, particles need not be touching for induced electrostatic forces to exist with AC fields. The differential equation for the voltage across two particles could be obtained by applying Kirchhoff's law (Colver and Wang, June, 1993)

$$\frac{dV_c}{dt} + \frac{V_c}{\tau_c} = \frac{V_o}{\tau_s} e^{(i\omega t)} \quad (4.22)$$

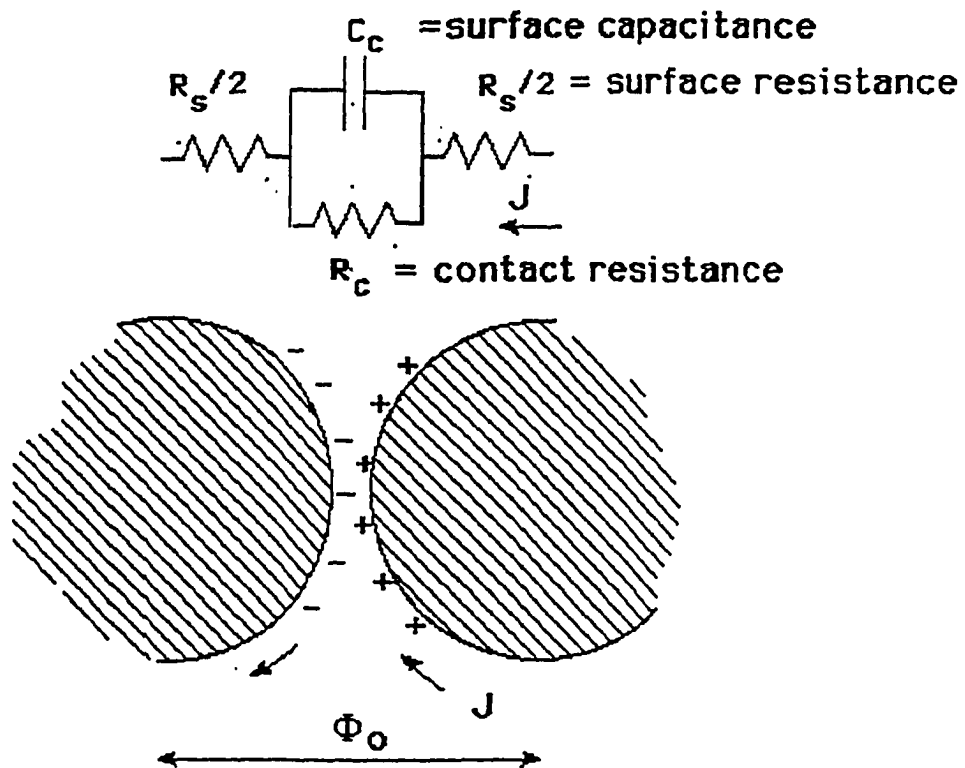


Figure 4.7 Equivalent circuit for particles with mutual capacitance, including contact resistance and surface conductivity

where the time constants for the particle contact (τ_c) and surface contact resistance (τ_s) were

$$\tau_c = \frac{R_s R_c}{R_s + R_c} C_c \quad (4.23)$$

$$\tau_s = R_s C_c \quad (4.24)$$

There were two limiting cases which depended on the relative position of the particles and the magnitudes of the surfaces and contact resistance.

(I) $R_s \gg R_c$ (e.g. particles touching, DC/AC field)

(II) $R_s \ll R_c$ (e.g. particles not touching, AC field only)

The steady periodic solution for Eqn. (4.22) was

$$V_c = \frac{V_o \left(\frac{\tau_c}{\tau_s} \right)}{\left[1 + (\tau_c \omega)^2 \right]^{\frac{1}{2}}} e^{i(\omega t - \delta)} \quad (4.25)$$

where $\tan \delta = \omega \tau_c$. The force magnitude per unit area between the plates of the capacitor was given by the relation

$$\frac{F_{J-AC}}{A} = \frac{\epsilon_{em,o} E_c^2}{2} = \frac{\epsilon_{em,o} \left(\frac{\tau_c}{\tau_s} \right) \left(\frac{V_o}{X} \right)^2}{2 \left[1 + (\tau_c \omega)^2 \right]} \quad (4.26)$$

The value for τ_s could be calculated if the resistivity of the bulk bed was known (Colver, 1980). For the 44-74 μm glass

spheres, $\tau_s=0.44$ s when the bulk bed resistivity was 2×10^{10} Ω -m at 25 °C. For the FCC (2-A), $\tau_s=0.12$ sec when the bulk bed resistivity equaled 5.4×10^9 Ω -m at 25 °C. If it was assumed that $\tau_c=\tau_s=0.44$ sec and the variation in the particle separation distance (x) as the bed volume decreased was ignored, then a plot of F_{J-AC} vs. ω (Fig.4.8) showed good agreement with the experimental result of maximum bed height vs. frequency (Fig.3.13). By comparing Eqn.4.26 with F_{J-DC} (Eqn.4.19), a possible expression for the AC electric force could be written as

$$F_{J-AC} = \frac{K\pi\epsilon_{en.o}d^2E_{max}^\gamma\left(\frac{3}{2}E_o\right)^{2-\gamma}}{1+(\tau_c\omega)^2} \quad (4.27)$$

for which the zero frequency limit was satisfied.

Figure 4.9 shows a plot of E^2 vs. f^2 for the frozen points in Fig.3.16, using FCC (2-A) fluidized with Ar at room temperature. Using Eqn.4.26 and assuming $\tau_c=\tau_s$, τ_c was found to be 0.25 sec. Comparing the calculated values with the result found previously of $\tau_c=0.12$ sec., it can be seen that the calculated value is of the same order. However, the DC limit was not well-fitted to this model. This was possibly due to

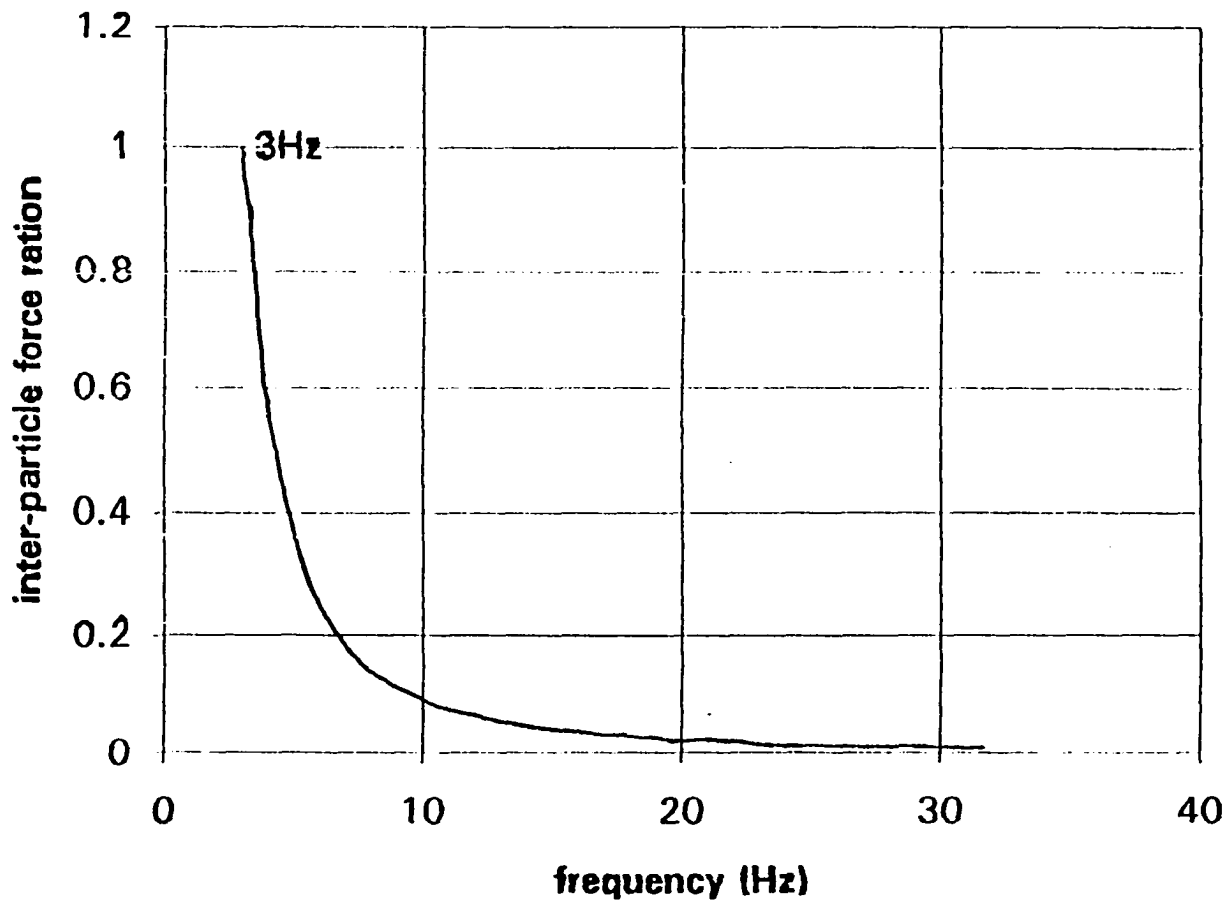


Figure 4.8 Decrease in particle-particle force with increasing frequency of electric field

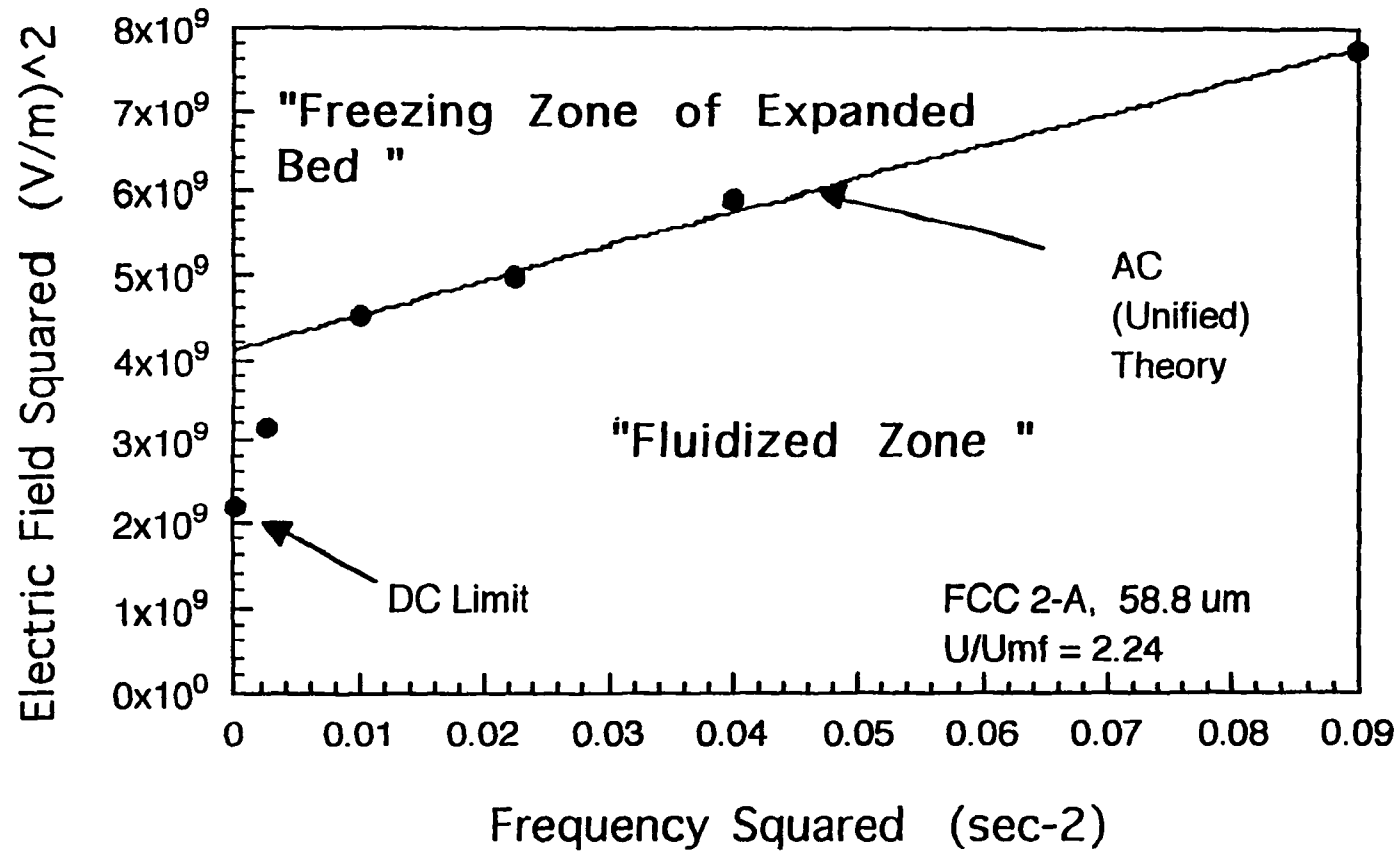


Figure 4.9 Freezing zone of expanded bed for frequency effect on the FCC 2-A with Argon (Ar) and $U/U_{mf} = 2.24$

the different mechanism between the DC and AC electric fields.

4.3 Stability Analysis

The perturbation method was applied to the governing equations of both fluid and dispersed phases, giving the stability analysis of the bed expansion (Rietema, 1991). A bed modulus of elasticity (Y) was proposed to account for observations of cohesive behavior in a field-free bed such as bed expansion and tilting of beds both of which resulted from interparticle forces. As the bed expanded with superficial velocity, particle contact remained, but the number of contacts (k) was reduced as particles shifted into a less dense formation, retaining a chain-like structure.

The procedure for applying the perturbation method was as follows:

1. Added a disturbance to the basic equations.
2. Subtracted out a steady solution from the basic equations.
3. Linearized the disturbance equation (the eigenvalue should be homogenous with homogenous boundary

conditions).

4. Assumed a form for disturbance such as a traveling wave with attenuation/growth term.
5. Solved certain values of parameters (eigenvalues).
6. Examined eigenvalues for growth, neutrality, or decay of disturbance (into bubbles).

The form of the modulus equation is

$$\frac{\partial \sigma_{s,xx}}{\partial x} = -Y \frac{\partial \varepsilon}{\partial x} \quad (4.28)$$

The purpose for extending this continuum concept was to include interparticle forces resulting from electric fields in Y so that $Y=Y(E,k\dots)$. Such a bed structure, as shown in Fig.4.10, allowed for conducting paths of current along chains of contacting particles through the bed. Because Y_{mb} was a measure of the bed interparticle forces, the lower the Y_{mb} , the easier it was for bubbles to form.

The criteria for bubble control was obtained based on perturbation theory utilizing continuum equations for the conservation of mass and momentum of the solids and gas phases was obtained (Appendix B for a detail derivation). The Kozeny-Carman (K&C) (which was used to derive the Ergun

equation) and Richardson-Zaki (R&Z) relationships were used to derive the particle drag force.

Using the Kozeny-Carman relationship, $f(\epsilon) = \epsilon^2/k(1-\epsilon)$ where k was a constant, the theoretical criteria for bubble control was given (Colver and Wang, Dec., 1993) as

$$\frac{\rho_p (\rho_p - \rho_f)^2 g^2 (\phi_s d_p)^4}{\mu^2 Y_{mb}} = \left[\frac{150(1 - \epsilon_{mb})}{(3 - 2\epsilon_{mb}) \epsilon_{mb}^2} \right]^2 \quad (4.29)$$

An experimental relationship for the bubble control criteria was given as

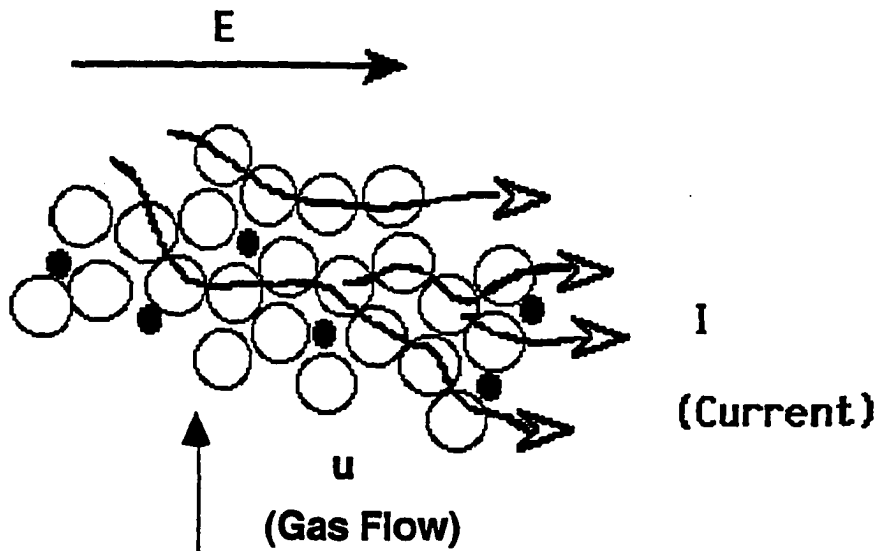


Figure 4.10 Conception of particle contacts during fluidization

$$Y_{mb} = \rho_p \left[(3 - 2\varepsilon_{mb}) \frac{U_{mb}}{\varepsilon_{mb}} \right]^2 \quad (4.30)$$

The Ergun constant, 150, and sphericity ϕ_s in Eqn.4.29 were chosen to fit the bed expansion data. The values also satisfied the momentum equations for the solids and gas phases. It should be noted that in the theoretical derivation of Eqn.4.29, a constant of 180 was obtained (see Eqn.B.26). However, the value of 150 for the constant had also been used by Davidson (1985) and Levenspiel (1991). A way to check the validity of the assumed values for the constants was to compare the drag force to the hydrodynamic force from the momentum equation. The following ratio should yield a constant value of 1:

$$\frac{(\rho_p - \rho_f) g (\phi_s d_p)^2 \varepsilon^3}{150(1 - \varepsilon)\mu U} = 1 \quad (4.31)$$

Fig.4.11 shows a plot of the ratio vs. different bed voidage for the 44.1 μm n.w.p. Microbeads glass particles with the N_2 .

The effect of the electric field needed to be explicitly included in the theory. This could be accomplished by relating Y_{mb} to E_{mb} using either the empirical relationships

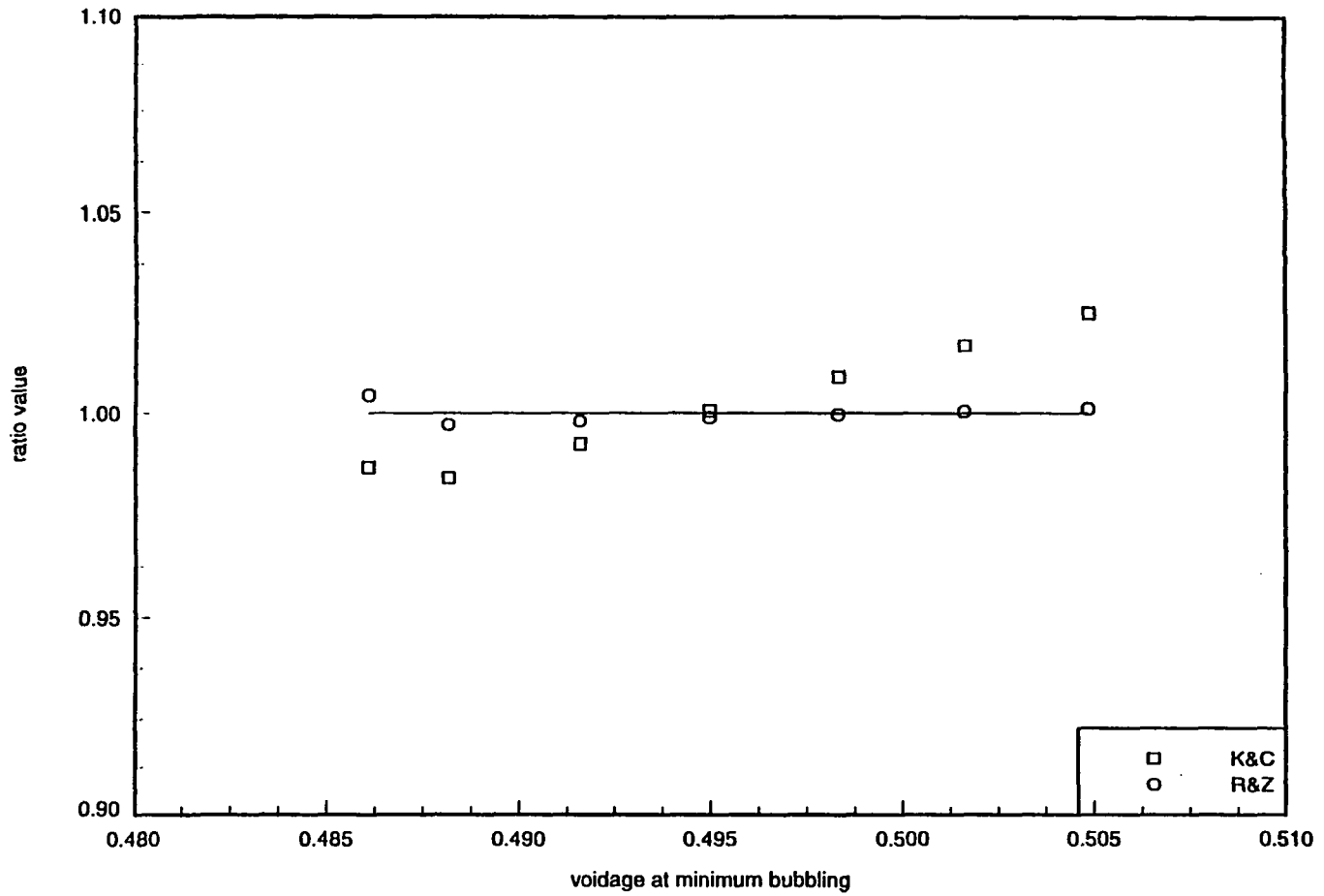


Figure 4.11 Comparison of constant for 44 μ m n.w.p. glass particles with N₂ using R&Z and K&C approaches

or particle force theory. An empirical relationship from the experimental data was given as

$$Y_{mb} \text{ (N/m)} = Y_{vdw,el} + cE_{mb} \text{ (kV/m)} \quad (4.32)$$

where $Y_{vdw,el}$ was the van der Waals and electronic contribution to the modulus and c was a constant. Eqns.4.29-4.32 form a complete set of relationships for the bed stability analysis. Fig.4.12 and 4.13 show the theoretical and experimental K&C elasticity modulus for the 44.1 μm n.w.p. Microbeads glass particles in a different electric field with Ar and N_2 , respectively.

The Richardson-Zaki type relationship was used for bed expansion,

$$f(\epsilon) = k\epsilon^n \quad (4.33)$$

the theoretical result was given as

$$\frac{\rho_p (\rho_p - \rho_f)^2 g^2 (\phi_s d_p)^4}{\mu^2 Y_{mb}} = \left[(1+n)(1-\epsilon_{mb}) \epsilon_{mb}^n \frac{k}{18} \right]^{-2} \quad (4.34)$$

and the experimental result was given as

$$Y_{mb} = \rho_p \left[(1-\epsilon_{mb})(1+n) \frac{U_{mb}}{\epsilon_{mb}} \right]^2 \quad (4.35)$$

in these equations, the values of k and n were derived from experimental data using superficial velocity and voidage at

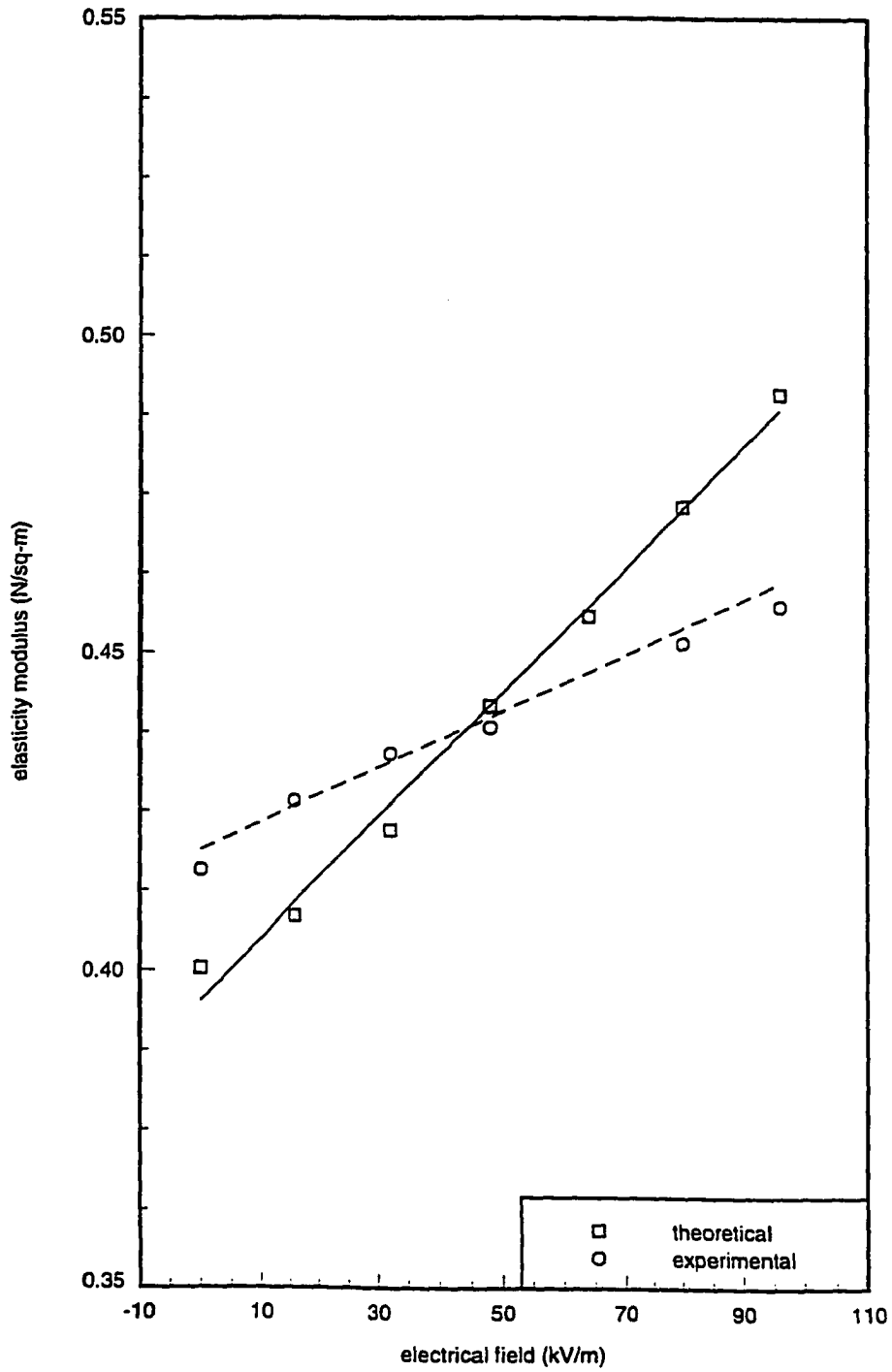


Figure 4.12 Experimental and theoretical Y_{mb} vs. E (K&C).
44 μ m, n.w.p. glass beads with Ar and AC-20Hz,
half p-p electric field

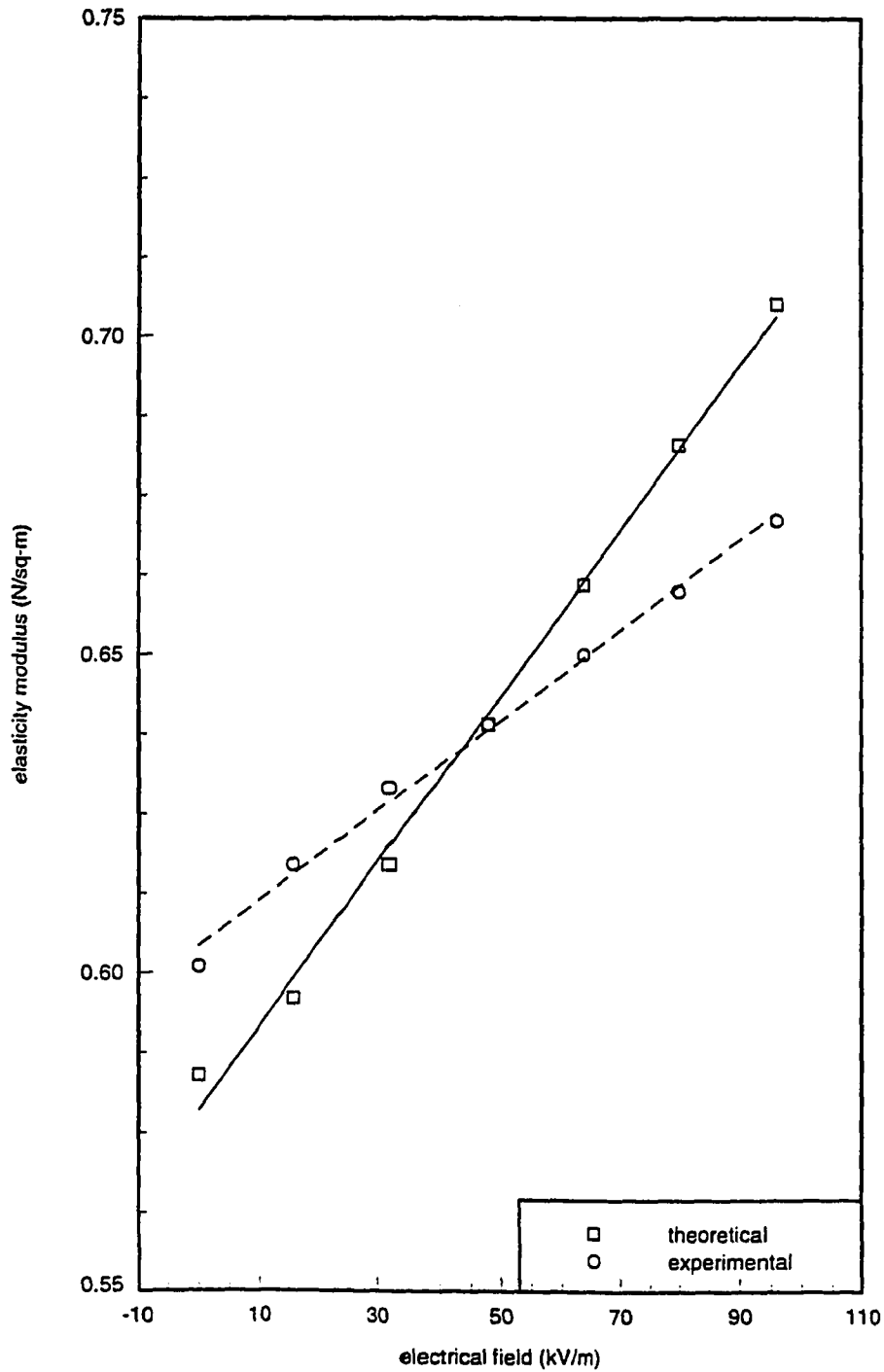


Figure 4.13 Experimental and theoretical Y_{mb} vs. E (K&C).
 44 μ m n.w.p. glass beads with N_2 and AC-3Hz,
 half p-p electric field

minimum bubbling and were chosen to fit the bed expansion data $f(\epsilon)$ and to satisfy the momentum equation for the solids and gas phases. k and n could be calculated from the plot of $\log(U)$ vs. $\log(\epsilon)$, where the interception of the first order regression fit was coordinated to k and the value of the first order of regression was coordinated to n . A way to check the validity of the assumed values for the constants was to compare the drag force to the hydrodynamic force from the momentum equation. The following ratio should yield a constant value of unity,

$$\frac{(\rho_p - \rho_f)g(\phi_s d_p)^2 \epsilon f(\epsilon)}{18\mu U} = 1 \quad (4.36)$$

Fig.4.11 shows the plot of this ratio vs. different bed voidage for the 44.1 μm non-water-proof (n.w.p.) Microbeads glass particles were fluidized with N_2 . Eqns.4.34-4.36 and Eqn.4.32 formed a complete set of relationships for the bed stability analysis. Figs.4.14, 4.15, 4.16, and 4.17 show the theoretical and experimental Richardson-Zaki elasticity modulus in different electrical field strength for the n.w.p. 44 μm Microbeads glass particles, FCC Kaolin (1-B), FCC Zeolitic (spent) (1-A), and FCC Zeolitic (fresh) (2-A) with

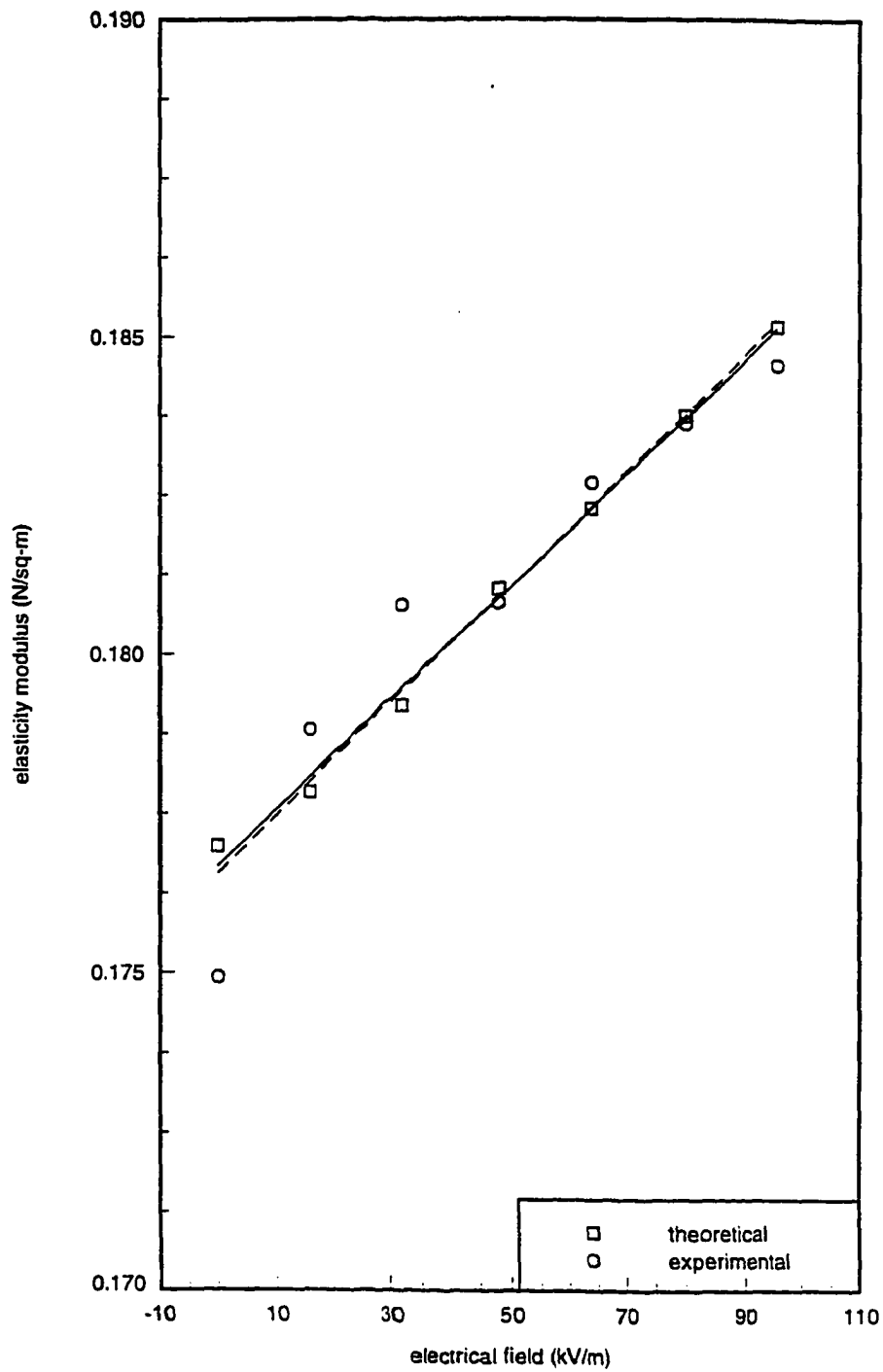


Figure 4.14 Experimental and theoretical Y_{mb} vs. E (R&Z).
44 μ m n.w.p. glass beads with Ar and AC-20Hz,
half p-p electric field

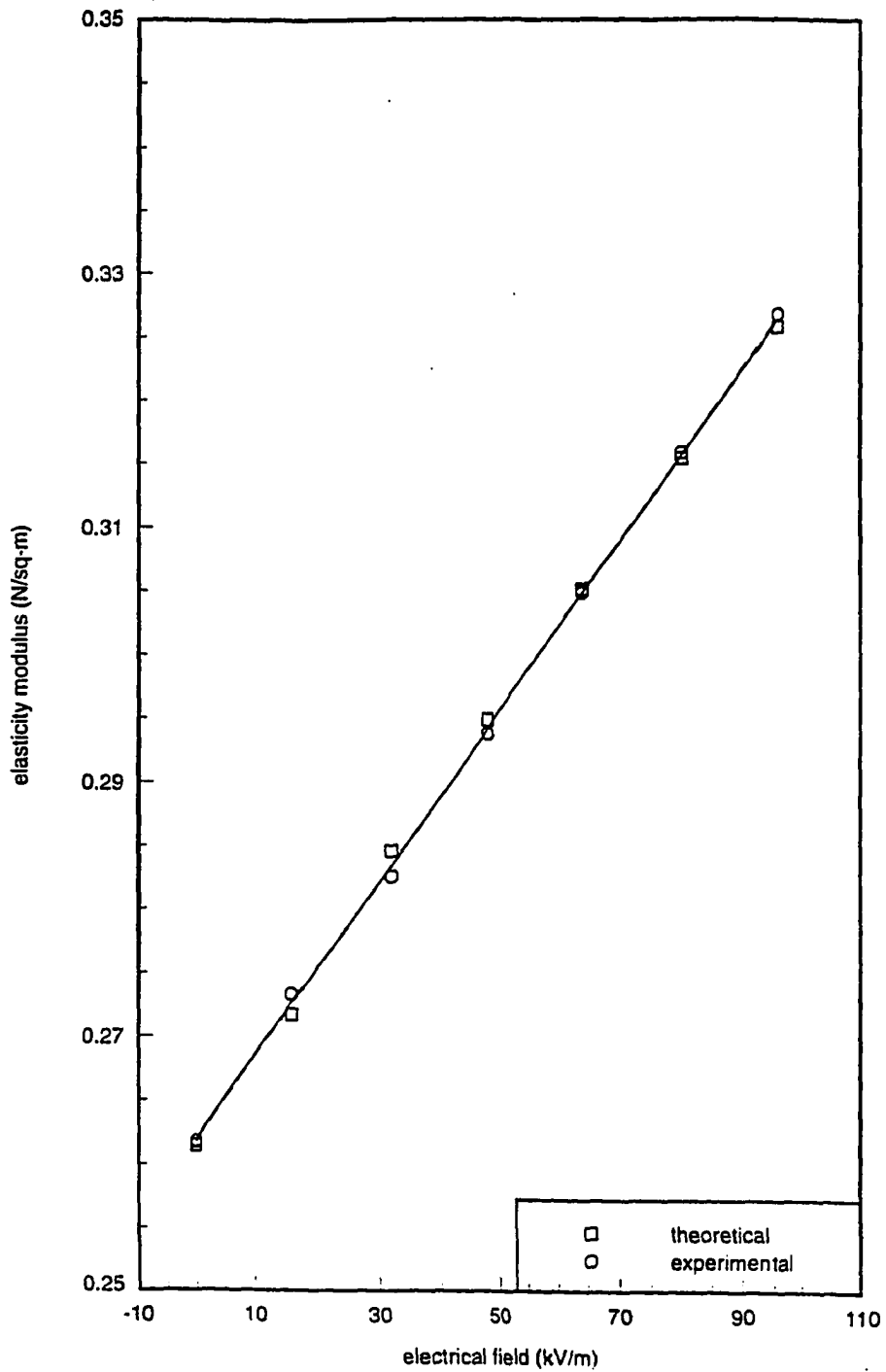


Figure 4.15 Experimental and theoretical Y_{mb} vs. E (R&Z).
FCC 1-B (Kaolin clay) with Ar and AC-1Hz, half
p-p electric field

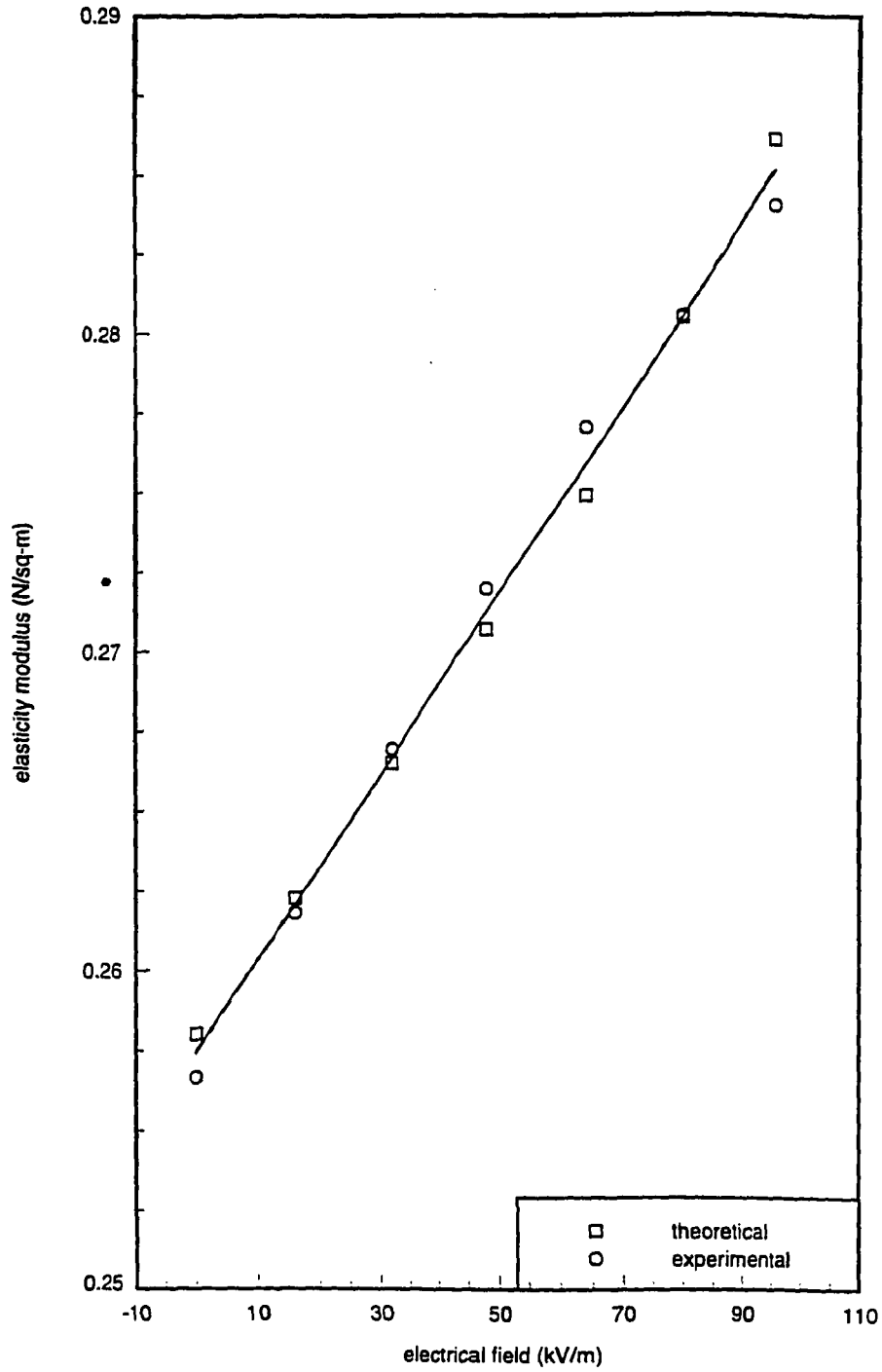


Figure 4.16 Experimental and theoretical Y_{mb} vs. E (R&Z).
FCC 1-A (Zeolitic, spent) with Ar and AC-1.5Hz,
half p-p electric field

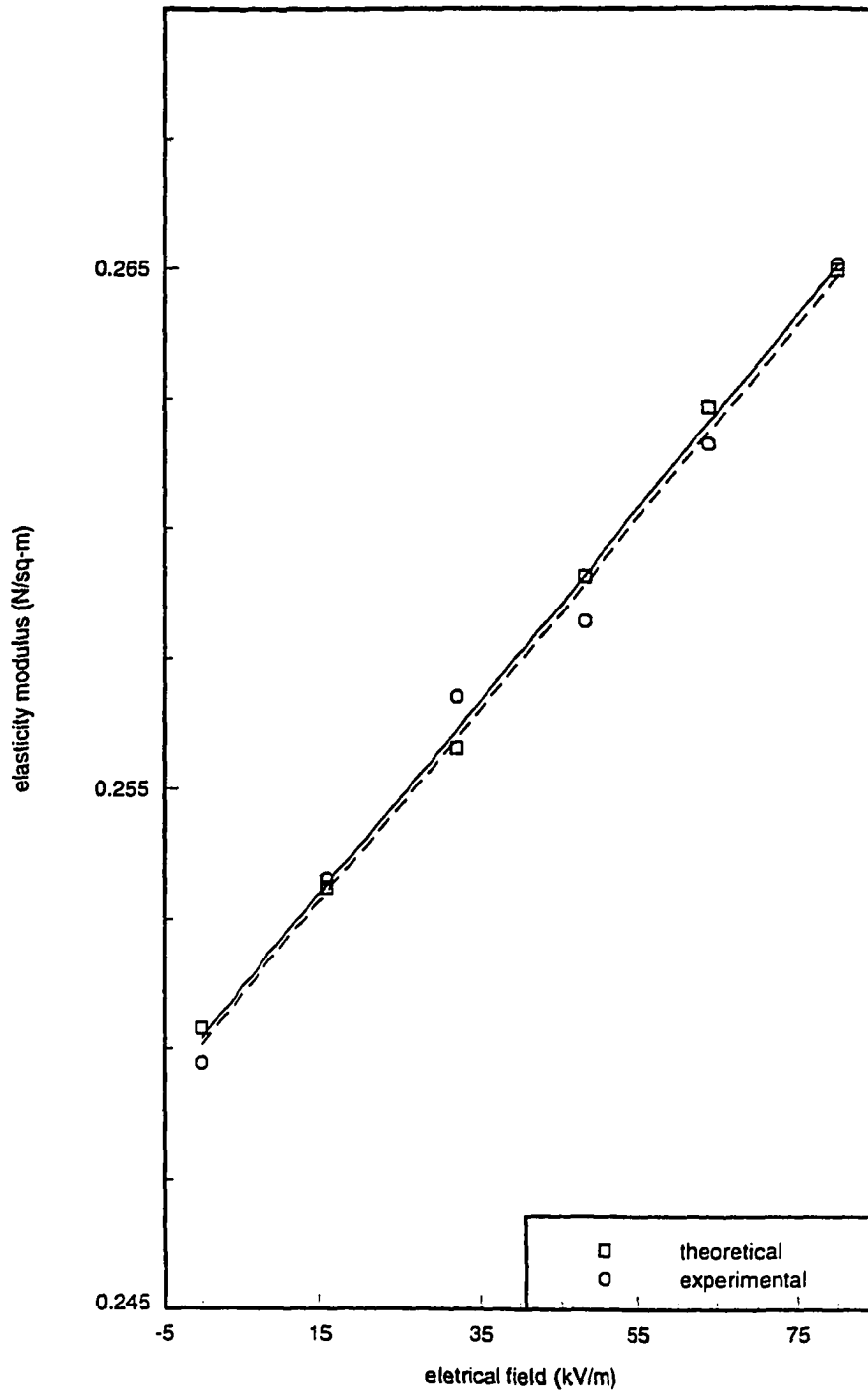


Figure 4.17 Experimental and theoretical Y_{mb} vs. E (R&Z). FCC 2-A (Zeolitic, fresh) with Ar and AC-1Hz, half p-p electric field

Ar, respectively (Colver and Wang, June, 1994). The summary results for the bed modulus and the Richardson-Zaki fit for different materials used in the tests are listed in Table 4.2.

The effect of the viscosity of the fluid was studied using four different gases, Ar, Air, N₂, and CO₂. Figs.4.13, 4.18, 4-19, and 4.20 show the theoretical and experimental results using the R&Z method. Fig.4.21 shows the result of Y_{mb} vs. voidage at U_{mb} . The trend is similar to that reported by Rietma (1991). Figs.4.22 and 4.23 show the effect of gas viscosity on the U_{mb} and voidage at U_{mb} , respectively. It agrees with the results reported by Xie and Geldart (1992).

The diameter effect on the U_{mb} is shown in Fig.4.24. The relation between the particle diameter and U_{mb} was shown as linear. It agrees with the result of Geldart (1986), $U_{mb}=2.07\exp(0.716F)d_p\rho^{0.06}\mu^{0.347}$, where F is the mass fraction of the powder less than 45 μm , and ρ and μ are gas density and gas viscosity. The effect of Y_{mb} on various diameters is shown in Fig.4.25. A relation between the Y_{mb} and the particle diameter will be found in the future study.

Table 4.2 Summary Results for Bed Modulus and Richardson-Zaki fit for Different Materials

Material Fluidized in Argon (Waddle diameter)	Bed Modulus of elasticity $Y_{mb}=A+B \times E_{mb}$ Y_{mb} (N/m ²) E_{mb} (kV/m)	n and k	Bulk Powder Resistivity Ohm-m (packed)	Comment on particle fluidization
Glass beads 44 μ m	A=0.177 B=8.854x10 ⁻⁵	n=1.585 k=0.0101	2.5x10 ¹⁰	Good fluidized (spherical,) large expansion
FCC Kaolin (1-B) 45.5 μ m	A=0.262 B=6.753x10 ⁻⁴	n=5.287 k=0.0272	2.2x10 ⁸	Moderate fluidized (irregular;) will channel; small expansion
FCC Zeolitic (spent) (1-A) 35 μ m	A=0.258 B=2.891x10 ⁻⁴	n=4.304 k=0.0357	1.1x10 ⁹	Moderate fluidized (near spherical;) will channel; small expansion
FCC Zeolitic (fresh) (2-A) 58.8 μ m	A=0.250 B=1.860x10 ⁻⁴	n=3.891 k=0.0099	5.4x10 ⁹	Good fluidized (near spherical,) moderate expansion
FCC Aluminum oxide (3-A) 66.7 μ m (Avg. large size)	can not be calculated	can not be calculated	7.5x10 ⁶	Poorly fluidized, channeling, irregular (many fines)

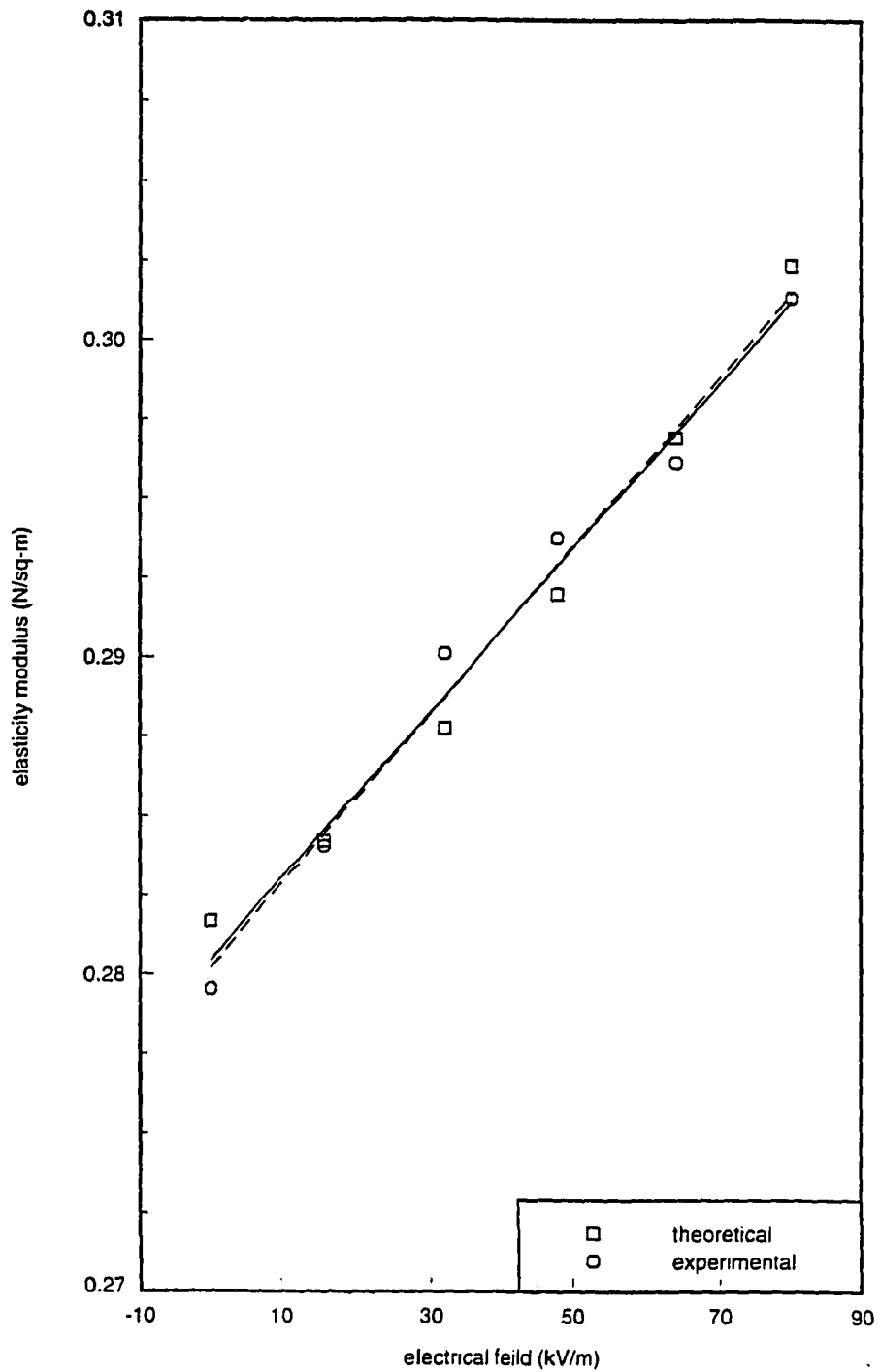


Figure 4.18 Experimental and theoretical Y_{mb} vs. E (R&Z).
44 μ m n.w.p. glass beads with Air and AC-3Hz,
half p-p electric field

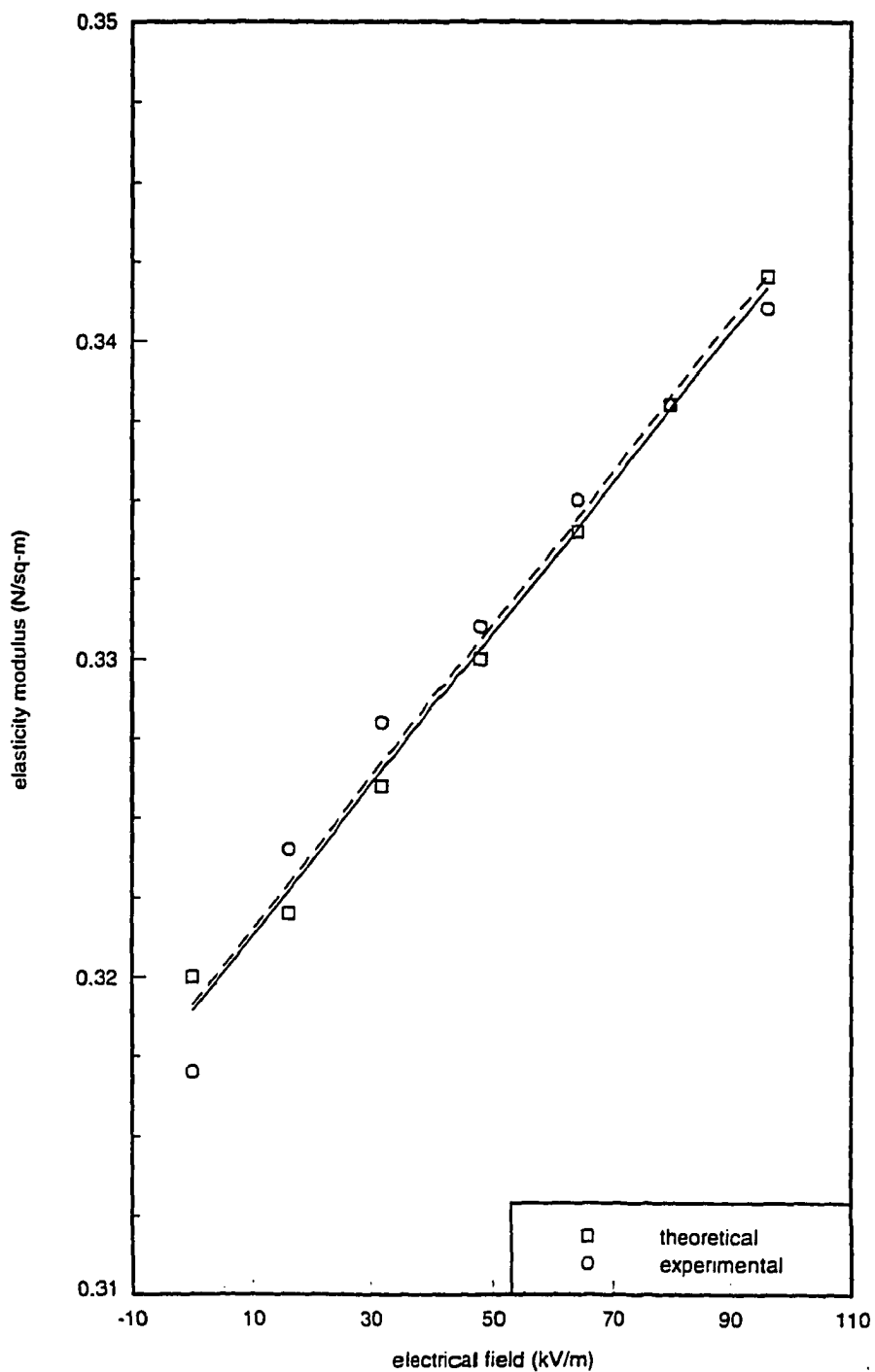


Figure 4.19 Experimental and theoretical Y_{mb} vs. E (R&Z).
44 μ m n.w.p. glass beads with N_2 and AC-3Hz,
half p-p electric field

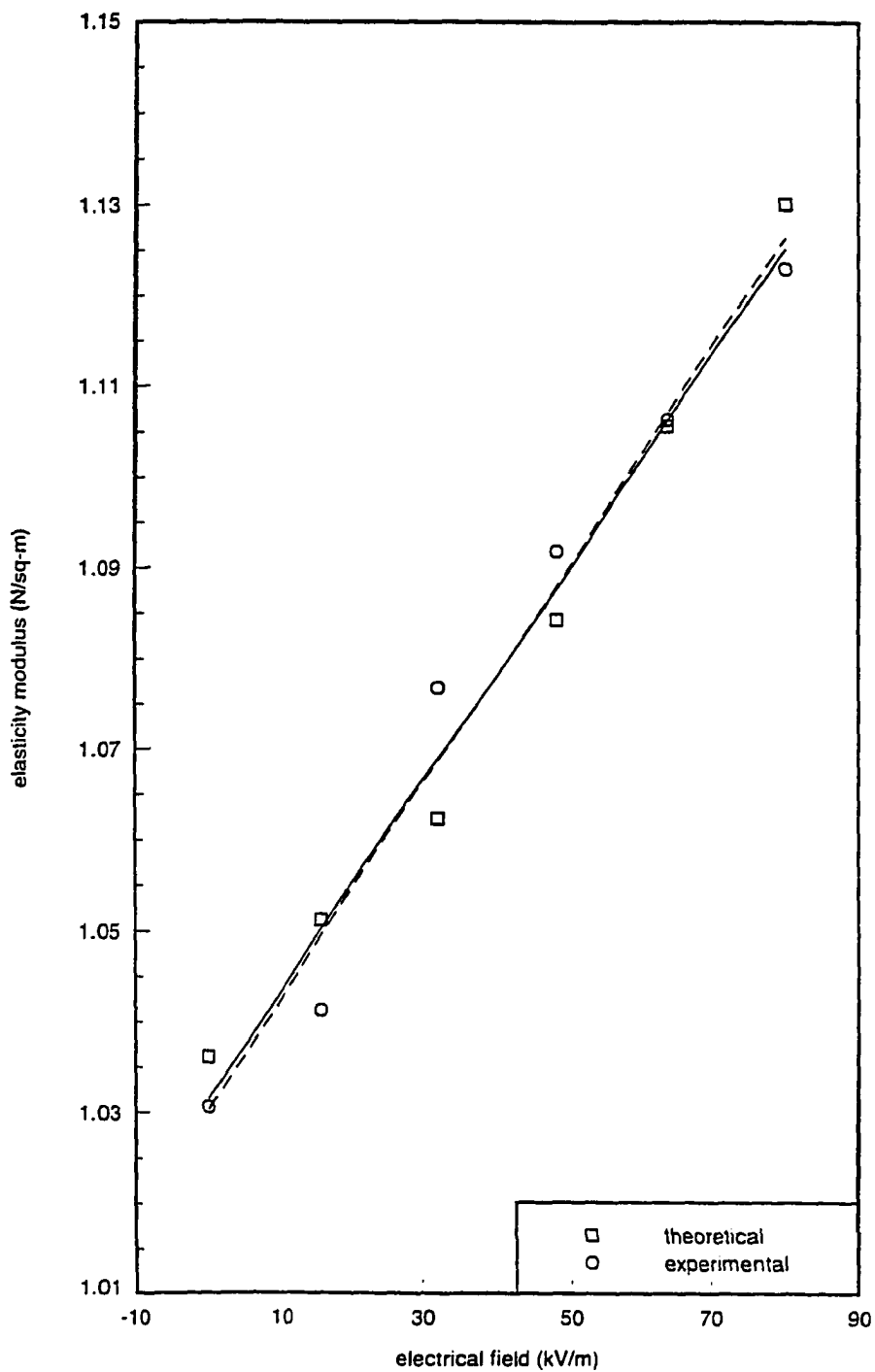


Figure 4.20 Experimental and theoretical Y_{mb} vs. E (R&Z).
44 μ m n.w.p. glass beads with CO_2 and AC-1.5Hz,
half p-p electric field

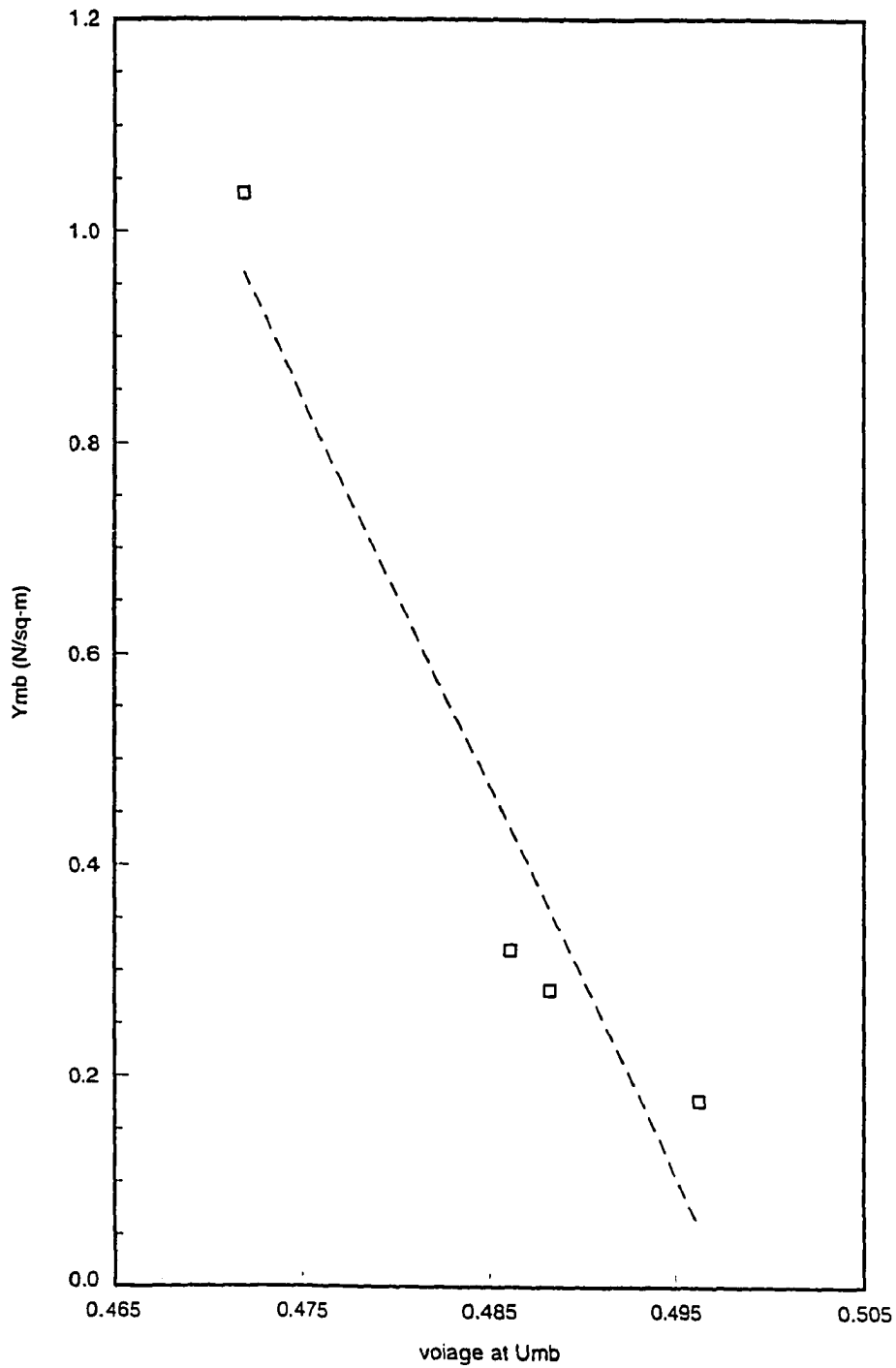


Figure 4.21 Y_{mb} vs. voidage at U_{mb} of different gas, $44.1 \mu\text{m}$, n.w.p. Microbeads glass, 24°C , 0 kV

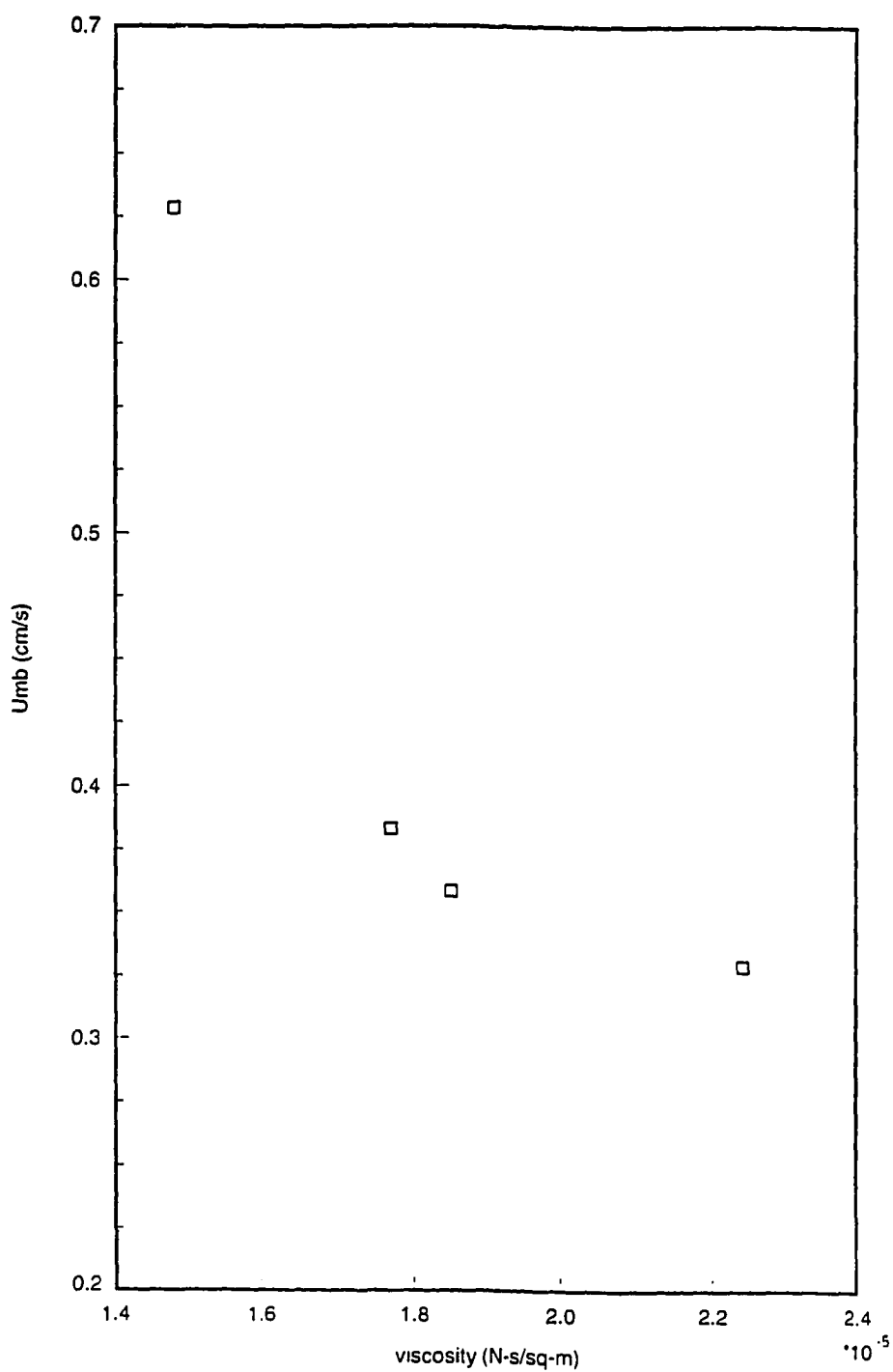


Figure 4.22 U_{mb} vs. gas viscosity, 44.1 μm ,
n.w.p. Microbeads glass,
24 °C, 0 kV

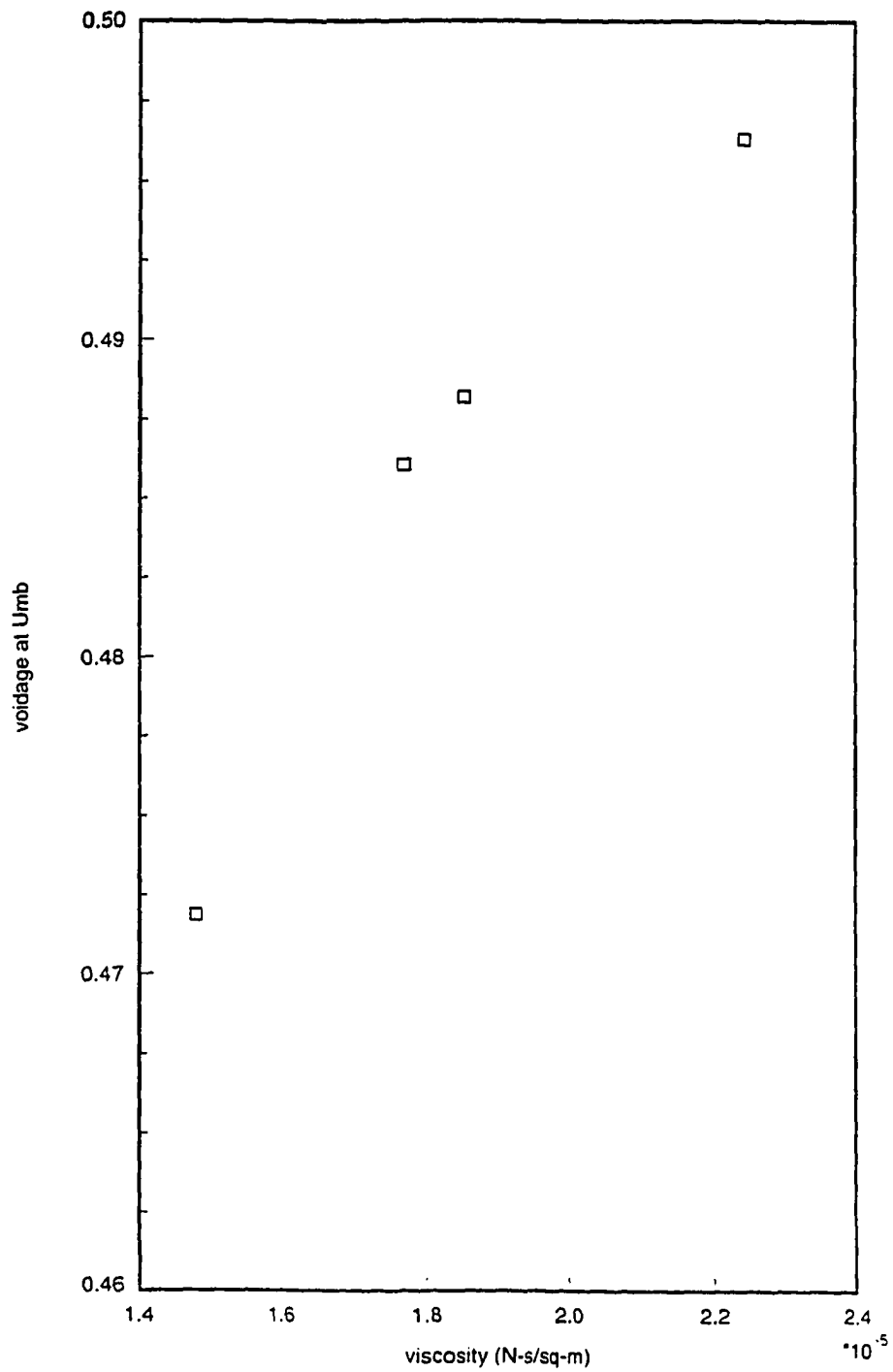


Figure 4.23 ϵ_{mb} vs. gas viscosity 44.1 μm ,
n.w.p. Microbeads glass,
24 °C, 0 kV

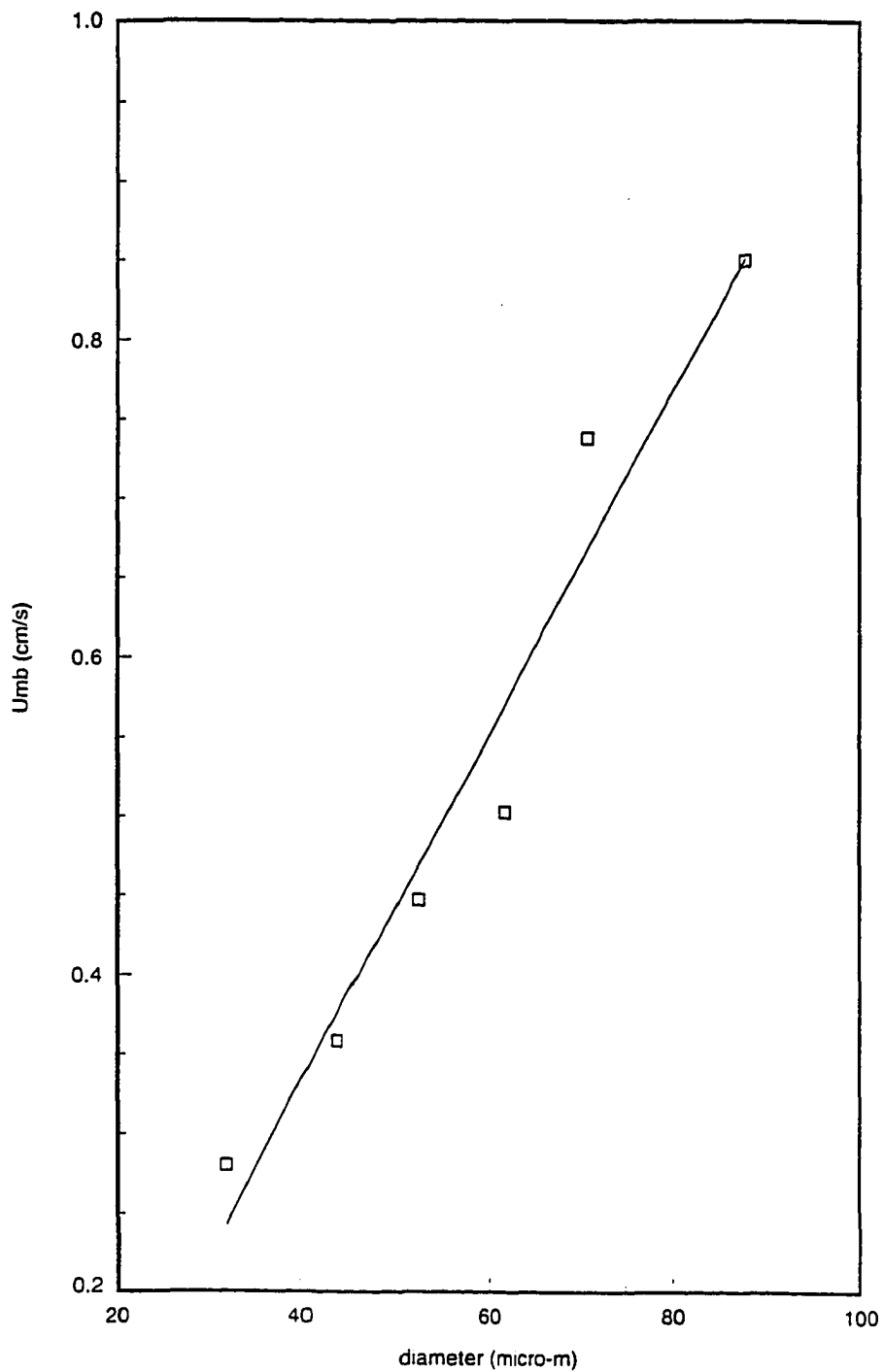


Figure 4.24 U_{mb} vs. particle diameters, n.w.p.
Microbeads glass, 24 °C, 0 kV
R.H.=9.8%, Air

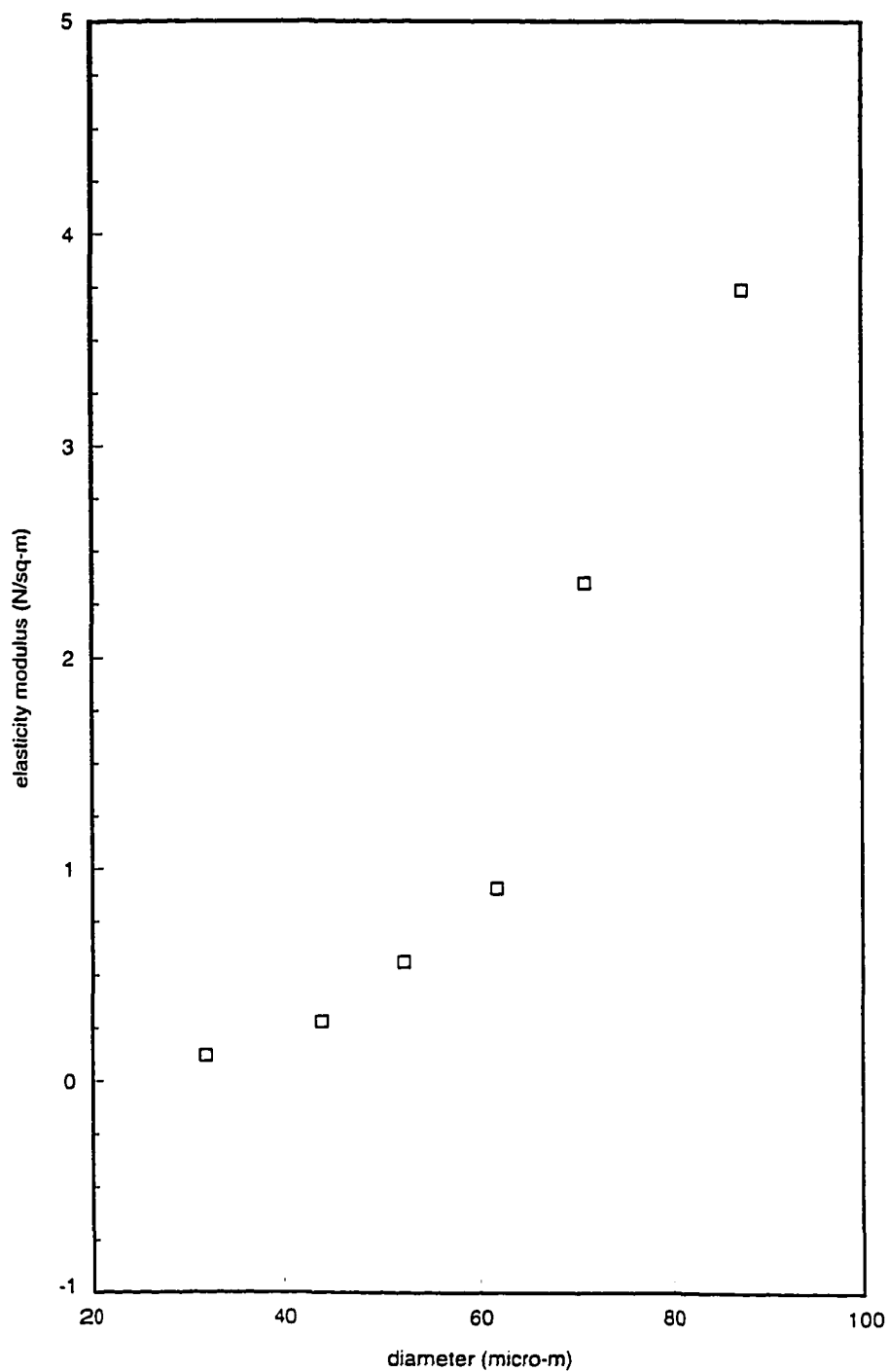


Figure 4.25 Y_{mb} vs. particle diameter,
n.w.p. Microbeads glass, 24 °C,
0 kV, R.H.=9.8%, Air

Figs.4.26 and 4.27 show the elasticity modulus vs. frequency for the n.w.p. Microbeads glass particles with N_2 using the K&C and R&Z methods, respectively. The result is similar to the bed height vs. frequency given in Fig.3.10.

Figure 4.28 show Y_{mb} at various relative humidities with and without an electric field. The increase in relative humidity would decrease the Y_{mb} in the case of both 0 kV and 4 kV.

The effect of temperature was also tested. The results are shown in Figs.4.29 and 4.30 for ϵ_{mb} vs. T and U_{mb} vs. T , respectively. It has the same trend as reported by Xie and Geldart (1993). It was found that the distributor did not uniformly distribute the gas flow across the bed. A discrepancy of U_{mb} at room temperature was found between the high temperature quartz bed and room temperature Pyrex bed. A change of distributor will be considered in future research. However, the trends in the data are probably correct.

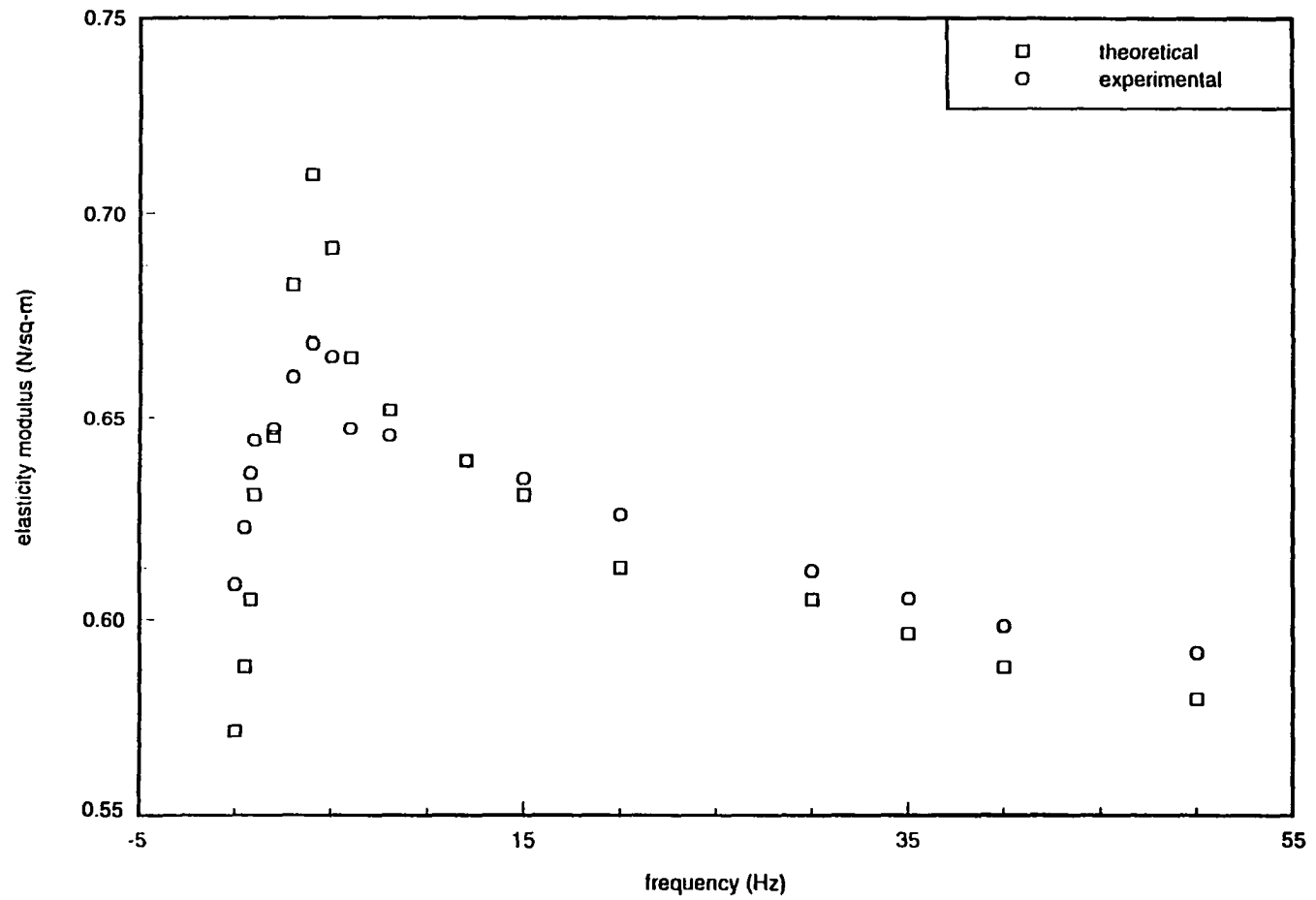


Figure 4.26 Experimental and theoretical bed elasticity modulus for various frequency at constant electric field strength using K&C relation. 44 μ m n.w.p. glass beads with N₂

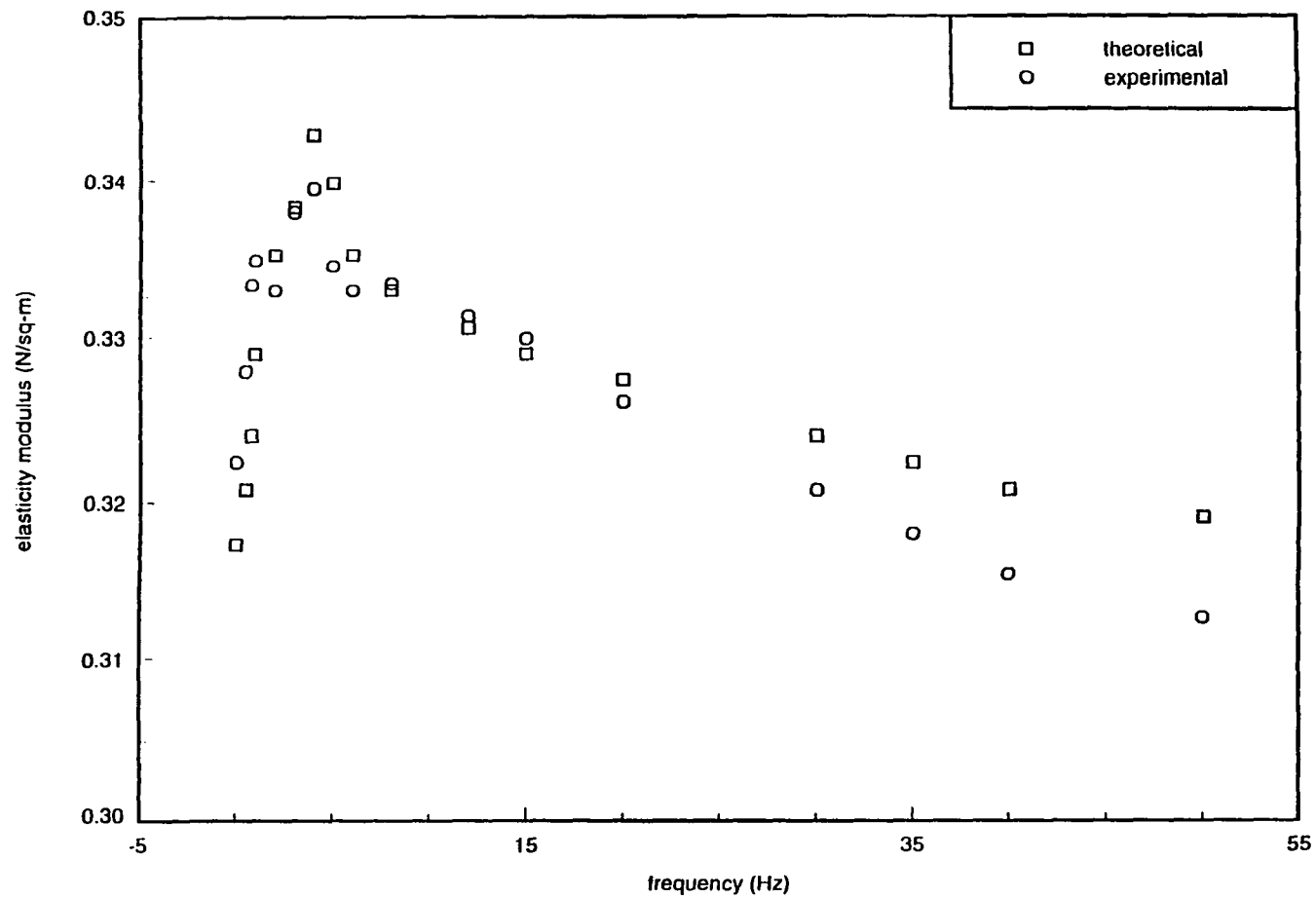


Figure 4.27 Experimental and theoretical bed elasticity modulus for various frequency at constant electric field strength using R&Z relation. 44 μ m n.w.p. glass beads with N₂

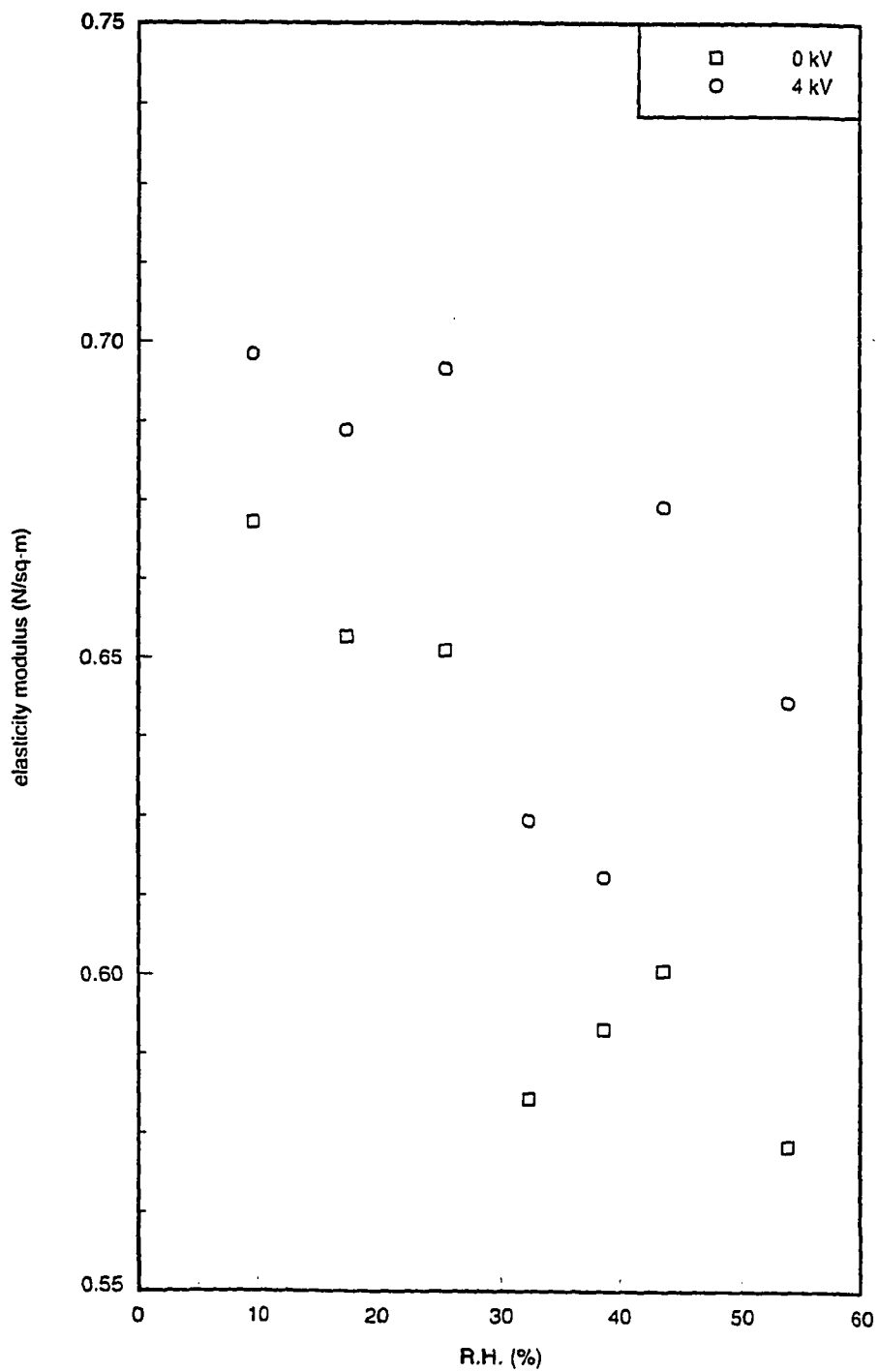


Figure 4.28 Y_{mb} with and without electric field (AC, 4 kV, p-p) v.s. R.H., n.w.p. 44 μ m Microbeads glass, 24 °C, Air

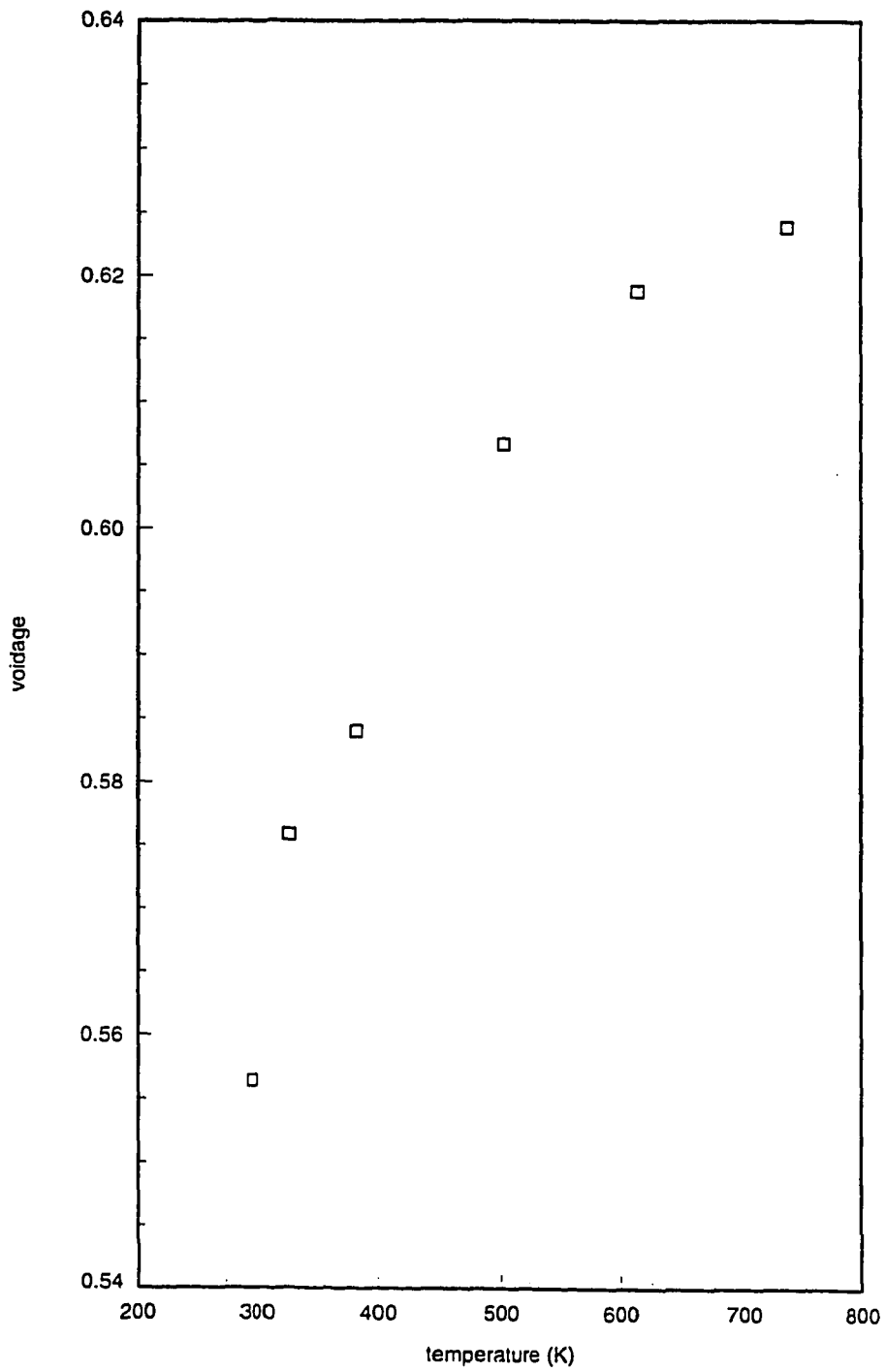


Figure 4.29 Voidage at U_{mb} vs. temperature, FCC (2-A), Ar, 0 kV

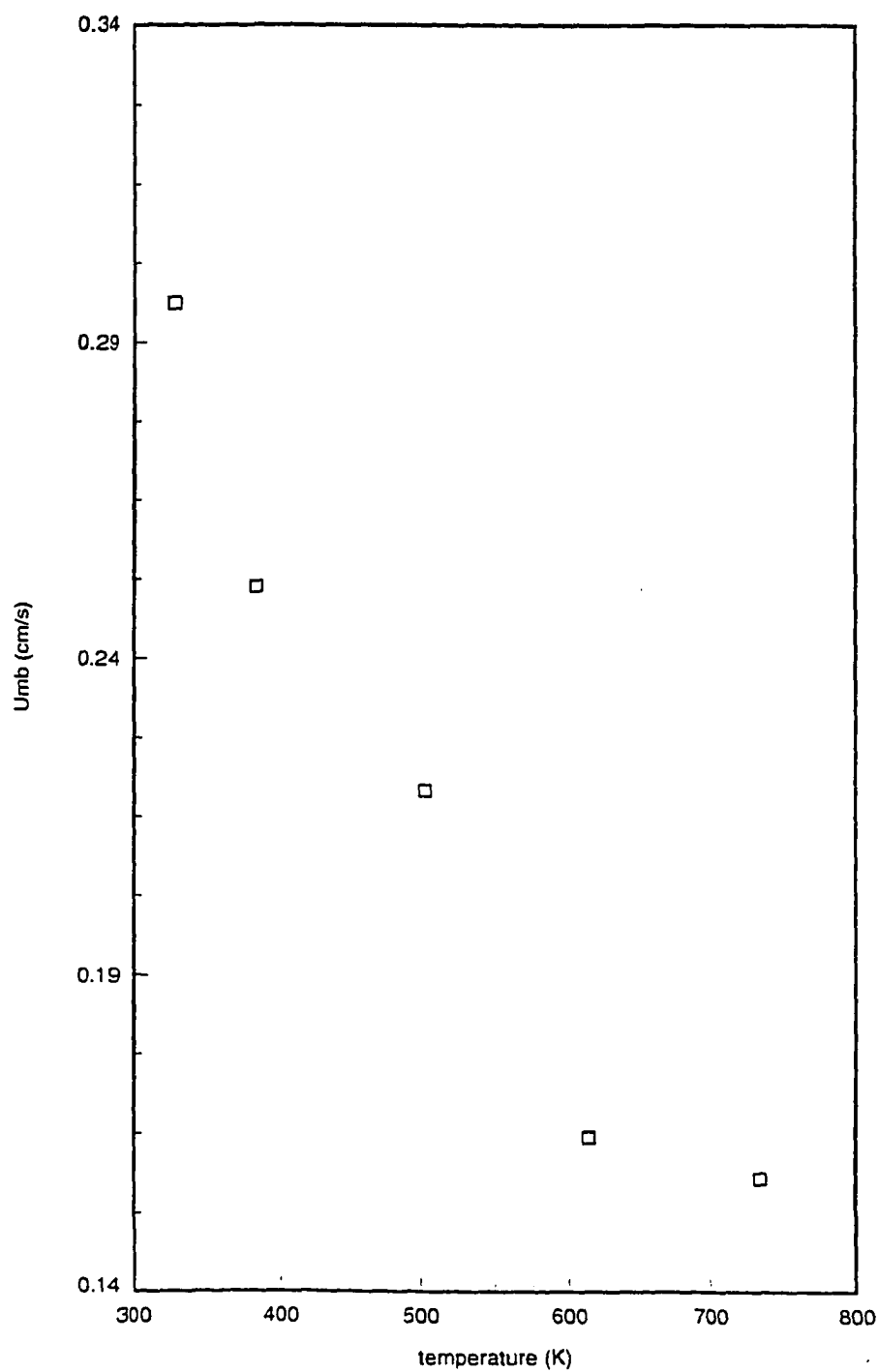


Figure 4.30 U_{mb} vs. temperature, FCC (2-A),
Ar, 0 kV

4.4 Scale-up Analysis

Scale-up relationships were developed using the method following Glicksman (Glicksman, 1984) by adding the electrical field term into the governing equations. Utilizing the dispersed phase differential equation and the characteristic scaling boundary dimensions, the following possible dimensionless groups for a fluidized bed were obtained (see Appendix C):

$$\frac{\beta d_p}{\rho_p u_o}, \frac{g d_p}{u_o^2}, \frac{H}{d_p}, \frac{D}{d_p}, \frac{\rho_f}{\rho_p}, \frac{p_o}{\rho_p u_o^2}, \frac{Y}{\rho_p u_o^2}$$

The last term includes the elasticity modulus relating the inter-particle forces and can be expressed with the electric field (Eqn.4.32).

An alternative form of the inter-particle force or bed modulus term was found by dividing the last term in the list by the second term, or $Y/(\rho_p g d_p)$. Using the inter-particle force relation derived from Colver's (1993) DC and AC models (based on Davidson's field-free model), the elasticity modulus term for the AC and DC fields were defined as

$$\frac{F_{vdw,el} + F_{J-AC/DC}}{F_s} \approx \frac{Y_{vdw,el}}{\varepsilon(U_{mb})d_p\rho_p g} + \frac{8K\varepsilon_{em/o}E_{max}^\beta \left(\frac{3}{2}E_o\right)^{2-\beta}}{\varepsilon(U_{mb})d_p\rho_p g[1+(\tau_s\omega)^2]} \quad (4.37)$$

If we chose $\beta=1$, a linear relationship between Y_{mb} and E was obtained. Dropping all constants and references to U_{mb} , our scaling list for the AC and DC fields (Colver and Wang, Dec., 1994) and permanent forces becomes

$$\frac{\beta d_p}{\rho_p u_o}, \frac{g d_p}{u_o^2}, \frac{H}{d_p}, \frac{D}{d_p}, \frac{\rho_f}{\rho_p}, \frac{p_o}{\rho_p u_o^2}, \frac{Y_{vdw,el}}{\varepsilon(U) \rho_p d_p g}, \frac{\varepsilon_{em/o} E_{max} E_o}{\varepsilon(U) d_p \rho_p g [1 + (\tau_s \omega)^2]} \quad (4.38)$$

The bed voidage ε was related to other variables (e.g. H , D), as was the frequency ω , showing our list of dimensionless groups describing the bed as,

$$\frac{\beta d_p}{\rho_p u_o}, \frac{g d_p}{u_o^2}, \frac{H}{d_p}, \frac{D}{d_p}, \frac{\rho_f}{\rho_p}, \frac{p_o}{\rho_p u_o^2}, \frac{d_p \omega^2}{g}, \frac{Y_{vdw,el}}{\rho_p d_p g}, \frac{\varepsilon_{em/o} E_{max} E_o}{d_p \rho_p g}, \tau_s \omega \quad (4.39)$$

The last three terms are the three additional independent variables apparently needed to characterize the behavior of the fluidized bed; namely, permanent forces, electric field strength and frequency. The additional parameter, 7th term, represents a ratio of radial particle acceleration to gravitational forces. This final grouping in Eqn.4.39 could have been derived by adding the terms $Y_{vdw,el}$, $\varepsilon_{em/o}$, E , τ_s , and ω into the original list. However, only our modeling permitted us to formulate specific dimensionless terms as given in Eqns.4.38 and 4.39. These parameters can be used to

obtain the characteristic of a fluidized bed during the scale-up.

5. CONCLUSIONS

The effect of an electric field on a fluidized bed has been studied both experimentally and theoretically. Various parameters affecting the dynamics of the electrofluidized bed, such as the electric field strength, electric field frequency, relative humidity, gas viscosity, and particle diameter and temperature, have been examined.

Experimental results indicate that bubble formation and elutriation are controlled simultaneously. Bubble formation was retarded and bed expansion was achieved with the electric field. However, it was also shown that bed freezing was possible. Correlations and criteria for bed expansion using the two phase theory were obtained. A map of the electric field effect on a fluidized bed was presented to give a more general view of bubble control.

Up to 96% reduction in elutriation was achieved with an applied electric field acting on the fluidized bed. It was confirmed that the elutriation control was due to the electric field action on the bed and a precipitation effect

in the freeboard. The charge of elutriated fines was also measured.

Various interparticle forces were examined to help understand the mechanism of the fluidized bed. From the results of bubble control, it was shown that the current constriction force has a major influence on the particles. The electric force acting on the particles was studied using an extension of Davidson field-free bubble model (DC) and a two-particle AC model. Results showed agreement between experimental data and theoretical results.

A stability analysis using the bed elasticity modulus to predict bubble formation using both Kozeny-Carman and Richardson-Zaki relations was studied. The elasticity modulus at minimum bubbling for different conditions was investigated both theoretically and experimentally. Good agreement was found between the theoretical and experimental results. The bed elasticity modulus was affected by various parameters, such as particle diameter, gas viscosity, field frequency, and relative humidity. It was shown that bubbles could easily form with a lower bed elasticity modulus. Therefore, with high temperature, high relative humidity and high gas

viscosity, the bed was very unstable. However, with an electric field of suitable frequency, the bed elasticity modulus was increased and the formation of bubbles was suppressed.

The scale-up parameters of a fluidized bed with an electric field were also derived based on a non-dimensional analysis. Three new parameters, related to bed elasticity modulus, electric field strength and field frequency, were added to include the effect of an applied electric field.

BIBLIOGRAPHY

- Colver, G.M., "Dynamic and Stationary Charging of Heavy Metallic and Dielectric Particles Against a Conducting Wall in the Presence of a DC Applied Electric Field", *J. Applied Physics* 47, no. 11 (1976): 4839-4849.
- Colver, G.M., "Bubble Control in Gas-Fluidized Beds with Applied Electric Fields", *J. Powder Technology*, no. 17 (1977a): 9-18.
- Colver, G.M., "Bubble Control in Gas-Fluidized Beds with Applied Electric Fields, Analogies and Mechanisms", 2nd Powder and Bulk Solids Conf., Chicago, May 10-12, 1977b.
- Colver, G.M., "Electric Suspensions above Fixed, Fluidized and Acoustically Excited Beds", *J. Powder & Bulk Solids Technology*, no.4 (1980): 21-31.
- Colver, G.M., "The Influence of Electric and Magnetic Fields on Air-Fluidized Beds", NSF Workshop, Fluidization and Fluid-Particle System Research Needs and Priorities, Rensselaer Polytechnic Inst., Troy, NY, (17-19) Oct., 1979.
- Colver, G.M., and Bosshart, G.S., "Heat and Charge Transfer in an AC Electrofluidized Beds", *Multiphase transport: Fundamentals, Reactor Safety, Applications*, Vol. 1-5 (1980): 2215-2243.
- Colver, G.M., and Donahoe, T.S., "Bubble-Rise Velocity in AC and DC Electrofluidized Beds", *IEEE Trans. Industry Applications* 20, no. 2 (1984): 259-266.
- Colver, G.M., and Liu, X.M., "Capture of Fine Particles on Charged Moving Spheres: A New Electrostatic Precipitator", *IEEE Trans. Industry Applications* 27, no. 5 (1991): 807-815.

- Colver, G.M., and Wang, J.S., "Bubble and Elutriation Control in Fluidized Beds with Electric Fields", IFPRI Annual Report, AAR 24-02, Dec. 31, 1992.
- Colver, G.M., and Wang, J.S., "Bubble and Elutriation Control in Fluidized Beds with Electric Fields", IFPRI Annual Report, AAR24-03, Dec. 31, 1993.
- Colver, G.M., and Wang, J.S., "Electrostatics in Powders and Related High Temperature Phenomena: Fluidized beds and Elutriation", IFPRI Annual Meeting, Pasadena, California, June 27-30, 1993.
- Colver, G.M., and Wang, J.S., "Bubble and Elutriation Control in Fluidized Beds with Electric Fields", IFPRI Annual Report, ARR24-04, Dec. 31, 1994.
- Colver, G.M., and Wang, J.S., "Bubble Stability Modeling in Fluidized Beds Utilizing Electric Fields", 1st. International Particle Technology Forum, Denver, Colorado, August 17-19, 1994.
- Colver, G.M., and Wang, J.S., "Electric Field Control of Powders", IFPRI Annual Meeting, Goslar Germany, June 12-16, 1994.
- Colver, G.M., Tucholski, D.R., Soetomo, F., and Wang, J.S., "Electrostatics in Powders and Related High Temperature Phenomena", IFPRI Annual Meeting, Harrogate England, May 31-June 5, 1992.
- Davidson, J.F., Clift, R., and Harrison, D., *Fluidization*, London: Academic Press, 1985.
- Dietz, P.W., "Fields and Forces of a Macroscopic Sphere above a Ground Plane in a Sinusoidally Varying Electric Field", *J. Applied Physics* 48, no. 3 (1977): 1036-1040.
- Dietz, P.W., and Melcher, J.M., "Interparticle Electrical Forces in Packed and Fluidized Beds", *Ind. Eng. Chem. Fundam.* 17, no. 1 (1978a): 28-32.
-

- Dietz, P.W., and Melcher, J.M., "Momentum Transfer in Electrofluidized Beds", *AIChE Symposium of Air Pollutants-NO_x and Particulate Emissions* 74, no.175 (1978b), 166-174.
- Geldart, D., *Gas Fluidization Technology*, New York: John Wiley & Sons, 1986.
- Gidaspow, D., *Multiphase Flow and Fluidization*, San Diego: Academic Press, 1994.
- Glicksman, L.R., "Scaling Relationships for Fluidized Beds", *Chem. Eng. Sci.* 39, no.9 (1984): 1373-1379.
- Johnson, T.W., and Melcher, J.M., "Electromechanics of Electrofluidized Beds", *Ind. Eng. Chem. Fundam.* 14, no. 3 (1975): 146-153.
- Katz, H., and Sears, J.T., "Electric Field Phenomena in Fluidized and Fixed Beds", *Canadian J. Chem. Eng.* 47, Feb. (1969): 50-53.
- Kunii, D., and Levenspiel, O., *Fluidization Engineering*, Stoneham: Butterworth-Heinemann, 1991.
- Marangoni, R.D., Beckwith, T.G., and Lienhard, J.H., *Mechanical Measurements*, 5th edition, Reading, Massachusetts: Addison Wesley, 1993.
- Moissis, A.A., and Zahn, K., "Electrofluidized Bed Responses to Small Signal Excitations", *IEEE Trans. Industry Application* 22, no. 6 (1986): 1396-1403.
- Nayfeh, M.H., and Brussel, M.K., *Electricity and Magnetism*, New York: John Wiley & Sons, 1985.
- Reitema, K., *The Dynamics of Fine Powders*, Essex: Elsevier Science, 1991.
- Xie, H.Y., and Geldart, D., "The Role of Interparticle Forces in the Gas Fluidization of Fine Powders", IFPRI Annual Report, ARR15-07, 1993.
-

Xie, H.Y., and Geldart, D., "Interparticle Forces in Fine Particle Fluidization", IFPRI Annual Report, ARR15-06, Dec. 1992.

Zahedi, K. and Melcher, J.R., "Electrofluidized Beds in the Filtration of Submicron Aerosols", *APCA Journal*, Vol. 26 (1976): 345-351.

ACKNOWLEDGEMENTS

I would sincerely like to thank Dr. Colver, my advisor, for providing me with the opportunity to further my education. I was indebted to him for his professional guidance and invaluable advice and time, from the initiation to the final conclusion of the project.

I would like to express my appreciation to Mr. Robert D. Steed (Hap), Mr. James J. Dautremont and Mr. Gaylord N. Scandrett for helping in establishing the apparatus and setting up the instruments. I also like to thank Mr. Trond L. Forre, a glass blower in the glass blowing shop, for constructing the pyrex and quartz fluidized beds.

This work was supported by the International Fine Particle Research Institute(IFPRI). Thanks also to Mr. David R. Tucholski, a former student of Dr. Colver, for his help and advice throughout this project.

Finally, I would sincerely like to thank my family, especially my wife, Huey-Lin Huang, for their constant support and encouragement.

APPENDIX A: ERROR ANALYSIS

A.1 Propagation of Uncertainty

When data are gathered experimentally, there existed the possibility for three types of errors: systematic, illegitimate, and random. Systematic errors were consistent errors which occur from improper testing procedures. This type of error may be eliminated by calibration. Illegitimate errors could be considered as human error. This type of error may be eliminated through proper experimental procedures and repetition of the experiment. Random errors are accidental errors that were present in every measurement. They are inconsistent by nature and arise from a variety of sources. Random errors could not be eliminated, but they can be determined by statistical methods.

For a experimental variable which was not measured directly and derived from other experimental values, the uncertainty (or random error) must be estimated using the propagation of uncertainty which involved all the uncertainties of the dependent experimental values. The method assumes the following: (1) the measured quantities are

determined independently, (2) the uncertainties are measured at the same level (e.g., one standard deviation), and (3) the distribution in the uncertainties are symmetrical. The overall uncertainty of a calculated experimental variable was determined by the following equation (Marangoni, Bechwith, and Lienhard, 1993):

$$u_f = \left[\left(u_{x_1} \frac{\partial f}{\partial x_1} \right)^2 + \left(u_{x_2} \frac{\partial f}{\partial x_2} \right)^2 + \dots + \left(u_{x_n} \frac{\partial f}{\partial x_n} \right)^2 \right]^{\frac{1}{2}} \quad (\text{A.1})$$

where x_i was the nominal values of variables, u_{x_i} is the discrete uncertainties associated with the variables x_i , and u_f is the overall uncertainty in the calculated quantity f . In general, discrete uncertainties were taken to be half the resolution of the instrument used to measure the value x_i . For a function f given as

$$f = x_1^a x_2^b \dots x_n^m \quad (\text{A.2})$$

Eqn.(A.1) could be reduced to the following form

$$\frac{u_f}{f} = \left[a^2 \left(\frac{u_{x_1}}{x_1} \right)^2 + b^2 \left(\frac{u_{x_2}}{x_2} \right)^2 + \dots + m^2 \left(\frac{u_{x_n}}{x_n} \right)^2 \right]^{\frac{1}{2}} \quad (\text{A.3})$$

For a function f given as

$$f = x_1^a \ln(x_2) \quad (\text{A.4})$$

Eqn. (A.1) could be reduced to the following form

$$\frac{u_f}{f} = \left[a^2 \left(\frac{u_{x_1}}{x_1} \right)^2 + \left(\frac{1}{\ln(x_2)} \right)^2 \left(\frac{u_{x_2}}{x_2} \right)^2 \right]^{\frac{1}{2}} \quad (\text{A.5})$$

For multiple samples for which n was the total number of samples, the uncertainty was given as

$$s_x = \frac{s}{\sqrt{n}} \quad (\text{A.6})$$

where, s was the standard deviation.

A.2 Results

The estimation of uncertainty for the experimental results was given for three major tests.

A.2.1 Elutriation constant

Combining Eqn. (3.15) and Eqn. (3.19), it was shown that K_i was a function of t and $I_r = -\ln(I/I_0)$. Using Eqn. (A.5), the uncertainty of K_i is given as

$$\frac{u_{K_i}}{K_i} = \left[\left(\frac{u_t}{t} \right)^2 + \left(\frac{1}{\ln(I_r)} \right)^2 \left(\frac{1}{I_r} \right)^2 \left(\frac{u_{I_r}}{I_r} \right)^2 + \left(\frac{1}{\ln(I_r)} \right)^2 \left(\frac{1}{I_r} \right)^2 \left(\frac{1}{I_0} \right)^2 \left(\frac{u_{I_0}}{I_0} \right)^2 \right]^{\frac{1}{2}} \quad (\text{A.7})$$

The following data could be used to estimated u_{K_i}/K_i : $u_t=0.5$ s (second), $t=180$ s, $I=0.538$ mW, $I_o=0.544$ mW, $I_r=-\ln(I/I_o)=0.0111$ and $\ln(I_r)\approx-4.5$ (which made the $\ln(I_r)\times I_r$ the smallest), and $u_I=u_{I_o}=0.005$ mW (due to the fluctuating reading). Thus, the value for u_{K_i}/K_i is 0.28 (=28%).

A.2.2 Correlation of bed expansion

From Eqn.(3.7), $(H-H_{mf})/H$ was a function of constant a , b , $C(U)$, E (electric field strength), and $(U-U_{mf})/U_{mf}$. Eqn.(A.1) could be used to calculated the uncertainty of $(H-H_{mf})/H$. It is given as

$$\frac{u_{\frac{H-H_{mf}}{H}}}{\frac{H-H_{mf}}{H}} = \left[\left(\frac{u_{C(U)}}{C(U)} \right)^2 + \left(\frac{u_U}{U-U_{mf}} \right)^2 + \left(\frac{u_{U_{mf}} U}{U_{mf}(U-U_{mf})} \right)^2 + (u_b E \cdot \ln(10))^2 + (u_E b \cdot \ln(10))^2 + \left(u_a \cdot \ln \left(\frac{U-U_{mf}}{U_{mf}} \right) \right)^2 \right]^{\frac{1}{2}} \quad (A.8)$$

where the u_b , u_a , and $u_{C(U)}$ were the standard deviation of the experimental data of b , a , and $C(U)$, respectively. The following data could be used to estimated the uncertainty of $(H-H_{mf})/H$: $u_b=0.167 \times 10^{-6}$, $u_a=0.403$, $u_{C(U)}=0.0083$, $u_U=u_{U_{mf}}=0.0014$ cm/s $u_E=3125$ V/m, $C(U)=0.0750$, $b=0.953 \times 10^{-6}$, $a=0.603$, $E=312500$

V/m, $U=1.1$ cm/s, $U_{mf}=0.606$ cm/s. Thus, the value for $u_{(H-H_{mf})/H} / [(H-H_{mf})/H] = 0.18$ (=18%).

Another way to estimate the uncertainty of b was following the experimental procedure. From the experimental procedure, b was a function of E and $(H-H_{mf})/H$. The u_b was given as

$$\frac{u_b}{b} = \left[\left(\frac{u_E}{E} \right)^2 + \left(\frac{H_{mf}/(H-H_{mf})}{\log\left(\frac{(H-H_{mf})}{H}\right)} \right)^2 \left(\frac{u_H}{H} \right)^2 + \left(\frac{H_{mf}/(H-H_{mf})}{\log\left(\frac{(H-H_{mf})}{H}\right)} \right)^2 \left(\frac{u_{H_{mf}}}{H_{mf}} \right)^2 \right] \quad (A.9)$$

Given the following data, $H=11.4$ cm, $H_{mf}=9.9$ cm, $u_E/E=0.05$, and $u_H=u_{H_{mf}}=0.05$ cm, the value for u_b/b was 0.071 (=7.1%).

A.2.3 Elasticity modulus of the bed

From Eqn. (4.30), Y_{mb} (K&C) is a function of ρ_p , $(3-2\varepsilon_{mb})/\varepsilon_{mb}$, and U_{mb} . The uncertainty of Y_{mb} is given as

$$\frac{u_{Y_{mb}}}{Y_{mb}} = \left[\left(\frac{u_{\rho_p}}{\rho_p} \right)^2 + 4 \left(\frac{u_{(3-2\varepsilon_{mb})/\varepsilon_{mb}}}{(3-2\varepsilon_{mb})/\varepsilon_{mb}} \right)^2 + 4 \left(\frac{u_{U_{mb}}}{U_{mb}} \right)^2 \right]^{1/2} \quad (A.10)$$

where $\varepsilon_{mb}=1-M_p/(\rho_p gh)$ and M_p is the total mass in the fluidized bed. The density of particles, ρ_p , is given or measured from the experimental procedure 2.2, where $V_{\text{powder}} = V_{s-i} - V_i$ and M was

the mass of particles used for measuring the packed voidage.

Therefore, $\rho_p = M/V_{\text{powder}}$ and the uncertainty of ρ_p is given as

$$\frac{u_{\rho_p}}{\rho_p} = \left[\left(\frac{u_M}{M} \right)^2 + \left(\frac{V_{s+1}}{V_{s+1} - V_1} \right)^2 \left(\frac{u_{V_{s+1}}}{V_{s+1}} \right)^2 + \left(\frac{V_1}{V_{s+1} - V_1} \right)^2 \left(\frac{u_{V_1}}{V_1} \right)^2 \right]^{\frac{1}{2}} \quad (\text{A.11})$$

The uncertainty in ϵ_{mb} is given as

$$\frac{u_{\epsilon_{mb}}}{\epsilon_{mb}} = \left[\left(\frac{u_{M_p}}{M_p} \right)^2 + \left(\frac{u_{\rho_p}}{\rho_p} \right)^2 + \left(\frac{u_h}{h} \right)^2 \right]^{\frac{1}{2}} \quad (\text{A.12})$$

where h was the bed height, M_p was the mass of particles in the fluidized bed. Eqns. (A.10), (A.11), and (A.12) could be used to calculate the uncertainty of Y_{mb} . In the test of FCC (1-A) with Ar, $u_{M_p} = 0.5$ gm, $M_p = 339$ gm, $u_{\rho_p}/\rho_p = 0.005/2.19$, $u_h/h = 0.005/14.30 = 0.35\%$, and $u_{U_{mb}}/U_{mb} = 0.25/37 = 0.7\%$. Therefore, $u_{Y_{mb}}/Y_{mb} = 0.015 = 1.5\%$.

From Eqn. (4.35), the Y_{mb} (R&Z) is a function of ρ_p , $(1 - \epsilon_{mb})/\epsilon_{mb}$, n , and U_{mb} . Therefore, the procedure for estimating the uncertainty of Y_{mb} (R&Z) is the same as for Y_{mb} (K&C), except the second term of the right hand side of Eqn. (A.10) was $(1 - \epsilon_{mb})/\epsilon_{mb}$ and an $(1+n)$ term was added. The uncertainty of Y is given as

$$\frac{u_{Y_{mb}}}{Y_{mb}} = \left[\left(\frac{u_{\rho_p}}{\rho_p} \right)^2 + 4 \left(\frac{u_{(1-\epsilon_{mb})/\epsilon_{mb}}}{(1-\epsilon_{mb})/\epsilon_{mb}} \right)^2 + 4 \left(\frac{u_{|+n}}{1+n} \right)^2 + 4 \left(\frac{u_{U_{mb}}}{U_{mb}} \right)^2 \right]^{\frac{1}{2}} \quad (\text{A.13})$$

where the n was calculated from the first regression fit of $\ln(U)$ v.s. $\ln(\epsilon)$. Using the same data in the K&C method and adding the $u_{n+1}/(n+1)=0.005/4.30$, $u_{Y_{mb}}/Y_{mb}=0.016=1.6\%$. The summary results of error analysis is listed in Table A.1.

Table A.1: Summary results of error analysis

	u_{K_i}/K_i	u_b/b	$u_{Y_{mb}}/Y_{mb}$	$u_{(H_{mf}-H)/H} / [(H-H_{mf})/H]$
%	28	7.1	1.5	18

APPENDIX B: PERTURBATION THEORY

The perturbation theory follows the work of Rietema (Rietema, 1991). There are four equations and four unknowns: p , ε , u , and v . The four equations are:

Continuity equation for the solid phase

$$\frac{\partial \varepsilon}{\partial t} + v \frac{\partial \varepsilon}{\partial x} + (1 - \varepsilon) \frac{\partial v}{\partial x} = 0 \quad (\text{B.1})$$

Continuity equation for the gas phase (constant fluid density)

$$\frac{\partial \varepsilon}{\partial t} + u \frac{\partial \varepsilon}{\partial x} + \varepsilon \frac{\partial u}{\partial x} = 0 \quad (\text{B.2})$$

Momentum equation for the solids phase (neglect particle fluctuations)

$$(1 - \varepsilon) \rho_p \left\{ \frac{\partial v}{\partial t} + v \frac{\partial v}{\partial x} \right\} + (1 - \varepsilon) \frac{\partial P}{\partial x} + (1 - \varepsilon) \rho_p g - Y \frac{\partial \varepsilon}{\partial x} + W + F_s = 0 \quad (\text{B.3})$$

Momentum equation for the gas phase (neglected shear stress, tortuous flow effect and acceleration terms)

$$-\varepsilon \frac{\partial P}{\partial x} + \varepsilon \rho_f g + F_s = 0 \quad (\text{B.4})$$

Two voidage functions were used to derive the particle force drag:

$$\text{Kozeny \& Carman (K\&C)} \quad f(\varepsilon) = \frac{1}{10} \frac{\varepsilon^2}{(1-\varepsilon)} \quad (\text{B.5})$$

$$F_s = \frac{180\mu(1-\varepsilon)^2}{\varepsilon d_p^2} (v-u) \quad (\text{B.6})$$

$$\text{Richardson \& Zaki (R\&Z)} \quad f(\varepsilon) = \varepsilon^n \quad (\text{B.7})$$

$$F_s = \frac{18\mu}{d_p^2} \frac{1-\varepsilon}{\varepsilon^{n-1}} (v-u) \quad (\text{B-8})$$

Perturbations ($'$) were added to the steady state condition ($^{\circ}$):

$$\frac{F_s}{\varepsilon} = \left(\frac{F_s}{\varepsilon}\right)^{\circ} + \frac{d}{d\varepsilon} \left(\frac{F_s}{\varepsilon}\right) \varepsilon' + \frac{d}{dv} \left(\frac{F_s}{\varepsilon}\right) v' + \frac{d}{du} \left(\frac{F_s}{\varepsilon}\right) u' \quad (\text{B.9})$$

$$\varepsilon = \varepsilon^{\circ} + \varepsilon' \quad (\text{B.10})$$

$$v = v^{\circ} + v' \quad (\text{B.11})$$

$$u = u^{\circ} + u' \quad (\text{B.12})$$

After simplification, the resulting (linear) differential equation in ε' was

$$\frac{\partial^2 \varepsilon'}{\partial t^2} - C_d^2 \frac{\partial^2 \varepsilon'}{\partial x^2} + A \left(C_c \frac{\partial \varepsilon'}{\partial x} + \frac{\partial \varepsilon'}{\partial t} \right) = 0 \quad (\text{B.13})$$

Eqn. (B.13) was the solved for ε' .

The definitions of the wave velocities are:

$$\text{dynamic wave} \quad C_d = \sqrt{\frac{Y}{\rho_p}} \quad (\text{B.14})$$

continuity wave $C_c = (3 - 2\varepsilon^0)\mu^0$ (K&C) (B.15)

$$C_c = (n+1)(1 - \varepsilon^0)\mu^0 \quad (\text{R\&Z}) \quad (\text{B.16})$$

The value of A are:

$$A = \frac{180(1 - \varepsilon^0)\mu}{(\varepsilon^0)^3 d_p^2 \rho_p} \quad (\text{K\&C}) \quad (\text{B.17})$$

$$A = \frac{18\mu}{d_p^2} \frac{1}{(\varepsilon^0)^{n+1}} \quad (\text{R\&Z}) \quad (\text{B.18})$$

A perturbation solution was assumed in the form of a Fourier Series terms (perturbation grows or was damped with $\pm a$):

$$\varepsilon' = e^{at} e^{i\omega(t-x/C)} \quad (\text{B.19})$$

a and C are examined for bed stability (bubble formation).

One

finds that the bed is stable against formation of bubbles if

$$a = \frac{A}{2} \left(\frac{C_d}{C} - 1 \right) < 0 \quad (\text{B.20})$$

and

$$C_d > C > C_c \quad \text{leaves } \omega \text{ real} \quad (\text{B.21})$$

$$\omega^2 = \frac{A^2}{4} \left[\frac{C_c^2 - C^2}{C^2 - C_d^2} \right] \quad (\text{B.22})$$

At minimum bubbling, $a \rightarrow 0$ and all wave velocities are equal

$$C_{mb} = C = C_d = C_c \quad (\text{B.23})$$

this result follows since C_d decreases with increasing ϵ , [decreasing coordination number k (=number of particle contacts)]; where C_c decreased with ϵ as,

$$C_c = \frac{d_p^2 g(\rho_p - \rho_f)}{180\mu} (3 - 2\epsilon) \frac{\epsilon^2}{(1 - \epsilon)} \quad (\text{K\&C}) \quad (\text{B.24})$$

$$C_c = \frac{d_p^2 g(\rho_p - \rho_f)}{18\mu} (n + 1)(1 - \epsilon)\epsilon^n \quad (\text{R\&Z}) \quad (\text{B.25})$$

The criteria for bed stability from Perturbation theory for K&C [Eqns. (B.15), (B.21) and (B.24)] and for R&Z [Eqns. (B.16), (B.21) and (B.25)], respectively, are:

$$\frac{\rho_p (\rho_p - \rho_f)^2 g^2 d_p^4}{\mu^2 Y} \leq \left[\frac{180(1 - \epsilon)}{(3 - 2\epsilon)\epsilon^2} \right]^2 \quad (\text{K\&C}) \quad (\text{B.26})$$

$$\frac{\rho_p (\rho_p - \rho_f)^2 g^2 d_p^4}{\mu^2 Y} \leq \left[\frac{18}{(n + 1)(1 - \epsilon)\epsilon^n} \right]^2 \quad (\text{R\&Z}) \quad (\text{B.27})$$

When the bed elasticity reaches to a value that the above inequality, Eqn. (B.26) or Eqn. (B.27), is established, bubbles will form.

APPENDIX C: SCALE-UP PARAMETERS

Based on the fluid phase and particle phase momentum equations, scale-up parameters for the fluidized bed could be found using the non-dimensionalization method along with the boundary conditions of the bed (Glicksman, 1986). Rewriting the continuity and momentum equations and using ε (bed voidage) as the major parameter, the equations were given as follow

continuity equation:

$$\text{gas:} \quad \frac{\partial \varepsilon}{\partial t} + v_d \frac{\partial \varepsilon}{\partial h} - (1-\varepsilon) \frac{\partial v_d}{\partial h} = 0 \quad (\text{C.1})$$

$$\text{particles:} \quad \frac{\partial \varepsilon}{\partial t} + v_c \frac{\partial \varepsilon}{\partial h} + \varepsilon \frac{\partial v_c}{\partial h} = 0 \quad (\text{C.2})$$

momentum equation of gas phase and particle phase:

$$\text{gas:} \quad -\varepsilon \frac{\partial p}{\partial h} - \varepsilon \rho_f g + F_s = 0 \quad (\text{C.3})$$

particles:

$$(1-\varepsilon) \rho_p \left\{ \frac{\partial v_d}{\partial t} + v_d \frac{\partial v_d}{\partial h} \right\} + (1-\varepsilon) \frac{\partial p}{\partial h} + (1-\varepsilon) \rho_p g - Y \frac{\partial \varepsilon}{\partial h} + W + F_s = 0 \quad (\text{C.4})$$

where h is the bed height, w is the wall effect, F_s is the slip force between the gas and the particles, p is the

pressure drop of the bed, g was the gravity, ρ_f and ρ_p are density of gas and particle phase, respectively, and v_c and v_d velocities of particles respectively. The inter-particle force term was included in the fourth term of the momentum equation of the particle phase (Eqn.(C.4)). The non-dimensional parameters were

$$v'_d = \frac{v_d}{u_o}, v'_c = \frac{v_c}{u_o}, h' = \frac{h}{d_p}, t' = \frac{u_o}{d_p} t, p' = \frac{p}{p_o} \quad (C.5)$$

also assuming $w = 0$ and $F_s = \beta_s(v_d - v_c)$, where β_s is the drag coefficient defined by Glicksman and u_o is the superficial gas velocity. Substituting the above non-dimensional parameters into Eqn.(C.4) and multiplying by $[d_p/(\rho_p u_o^2)]$ given the non-dimensional form of Eqn.(C.4) as

$$(1-\varepsilon) \left\{ \frac{\partial v'_d}{\partial t'} + v'_d \frac{\partial v'_d}{\partial h'} \right\} + (1-\varepsilon) \frac{p_o}{\rho_p u_o^2} \frac{\partial p'}{\partial h'} + (1-\varepsilon) \frac{g d_p}{u_o^2} - \frac{Y}{\rho_p u_o^2} \frac{\partial \varepsilon}{\partial h'} + \frac{\beta_s d_p}{\rho_p u_o} (v'_c - v'_d) = 0 \quad (C.6)$$

The boundary conditions could be rewritten in terms of non-dimensional length scale as H/d_p , D/d_p , and ρ_f/ρ_p , where H is the bed height and D was the bed diameter. Therefore, the scale-up parameters of the fluidized bed are

$$\frac{p_o}{\rho_p u_o^2}, \frac{g d_p}{u_o^2}, \frac{Y}{\rho_p u_o^2}, \frac{\beta_s d_p}{\rho_p u_o}, \frac{H}{d_p}, \frac{D}{d_p}, \frac{\rho_f}{\rho_p} \quad (C.7)$$

APPENDIX D: PROPERTIES OF MATERIALS

The minimum fluidization velocity of the fluidized bed could be calculated using the Ergun equation or be determined by the plot of pressure drop of the fluidized bed versus the superficial velocity. From Fig.D.1, U_{mf} is 1.504 cm/s for the 74-144 μm non-water-proof Microbeads glass particles. The Ergun equation is given as

$$\frac{\rho_f (d_p \varphi_s)^3 (\rho_p - \rho_f) g}{\mu^2} = \frac{150(1 - \varepsilon_{mf}) \rho_f (d_p \varphi_s)}{\varepsilon_{mf}^3 \mu} U_{mf} + \frac{1.75 \rho_f^2 (d_p \varphi_s)^2}{\varepsilon_{mf}^3 \mu^2} U_{mf}^2 \quad (\text{D.1})$$

where ε_{mf} is the voidage of the minimum fluidization which was substituted by the $\varepsilon_{\text{packed}}$ during the calculation, d_p is the average particle diameter (110 μm for the 74-144 μm glass particles), φ_s is the particle sphericity (0.86 for the round particles or 1.0 for the spherical particles), ρ_p is particle density (2500 kg/m^3 for the glass particles), μ is the viscosity of the fluid (1.846×10^{-5} $\text{N}\cdot\text{s/m}^2$ for the air at room temperature), and ρ_f is the density of the fluid (1.1614 kg/m^3 for the air at room temperature). The calculated U_{mf} was 1.75

cm/s. Table D.1 shows the U_{mf} and U_{mb} for the glass particles at different temperatures.

Table D.2 shows the basic data of different bed materials which were used in tests. Figs. D.2, D.3, and D.4 showed the different bed materials taken from an SEM Kevex automated image analyzer. The Waddle diameter of fines in the ordinary sand was also measured. The definition was given as

$$d_{\text{waddle}} = \sqrt{\frac{4A_t}{\pi N}} \quad (\text{D.2})$$

where A_t was the total projected area of all particles analyzed and N was the sample size.

Table D.1 The U_{mf} and U_{mb} of glass particles at different temperatures

	25 °C (cm/s)		75 °C (cm/s)		125 °C (cm/s)				
	U_{mf}		U_{mb}	U_{mf}		U_{mb}	U_{mf}		U_{mb}
	exp.	cal.	exp.	exp.	cal.	exp.	exp.	cal.	exp.
44-53 μm	0.42	0.41	0.45	0.38	0.35	0.42	0.42	0.32	0.40
44-74 μm	0.56	0.49	0.61	0.56	0.44	0.59	0.53	0.39	0.56
105-125 μm	1.52	1.91	1.59	1.36	1.75	1.41	1.26	1.58	1.31
74-144 μm	1.50	1.74	1.55	1.33	1.54	1.38	1.26	1.32	1.30

the fluid was air, the relative humidity=7.6%, the particle density=2500 kg/m³, and $\epsilon_{mf}=\epsilon_{packed}$. The experimental data are measured by the plot of pressure drop across the bed verses the superficial velocity using the parallel copper bed placed in the oven. The glass beads were non-water-proof glass spheres (Microbeads). The volume resistivity was 2×10^{13} ohm-cm at 17 °C. Dielectric constant at 1 KHz and 23 °C was 12.1. Minimum 70% true spheres and not less than 80% in the specific range.

Table D.2 The properties of different materials

Material	ρ (density) g/cm^3	d (average) μm	ε (packed)	U_{mf} cm/sec (by air)
FCC kaolin(1B)	2.06	45.5	0.625	
FCC Zeolitic (spent) (1A)	2.19	35.0	0.611	
FCC Zeolitic (fresh) (2A)	2.1	58.8	0.621	
FCC Aluminum Oxide (3A)	3.5	66.7	0.496	
river sand	2.79	190	0.476	7.6
44-74 μm (W.P.)	2.5	59	0.450	0.644
74-144 μm (W.P.)	2.5	110	0.461	1.960
44-53 μm	2.5	49	0.471	0.496
63-74 μm	2.5	67.5	0.457	0.516
74-88 μm	2.5	81	0.445	0.768
88-105 μm	2.5	96.5	0.438	0.873
105-125 μm	2.5	110	0.424	1.522
125-147 μm	2.5	136	0.417	1.784
44-74 μm	2.5	59	0.451	0.558
74-144 μm	2.5	110	0.459	1.504

Where U_{mf} was measured at room temperature, d_p was the average particle diameter, the relative humidity was 9.8%, the fluid was air. Material items (6) to (15) are glass particles. W.P. meant water-proof particles coated with Teflon, which was on the surface of particles.

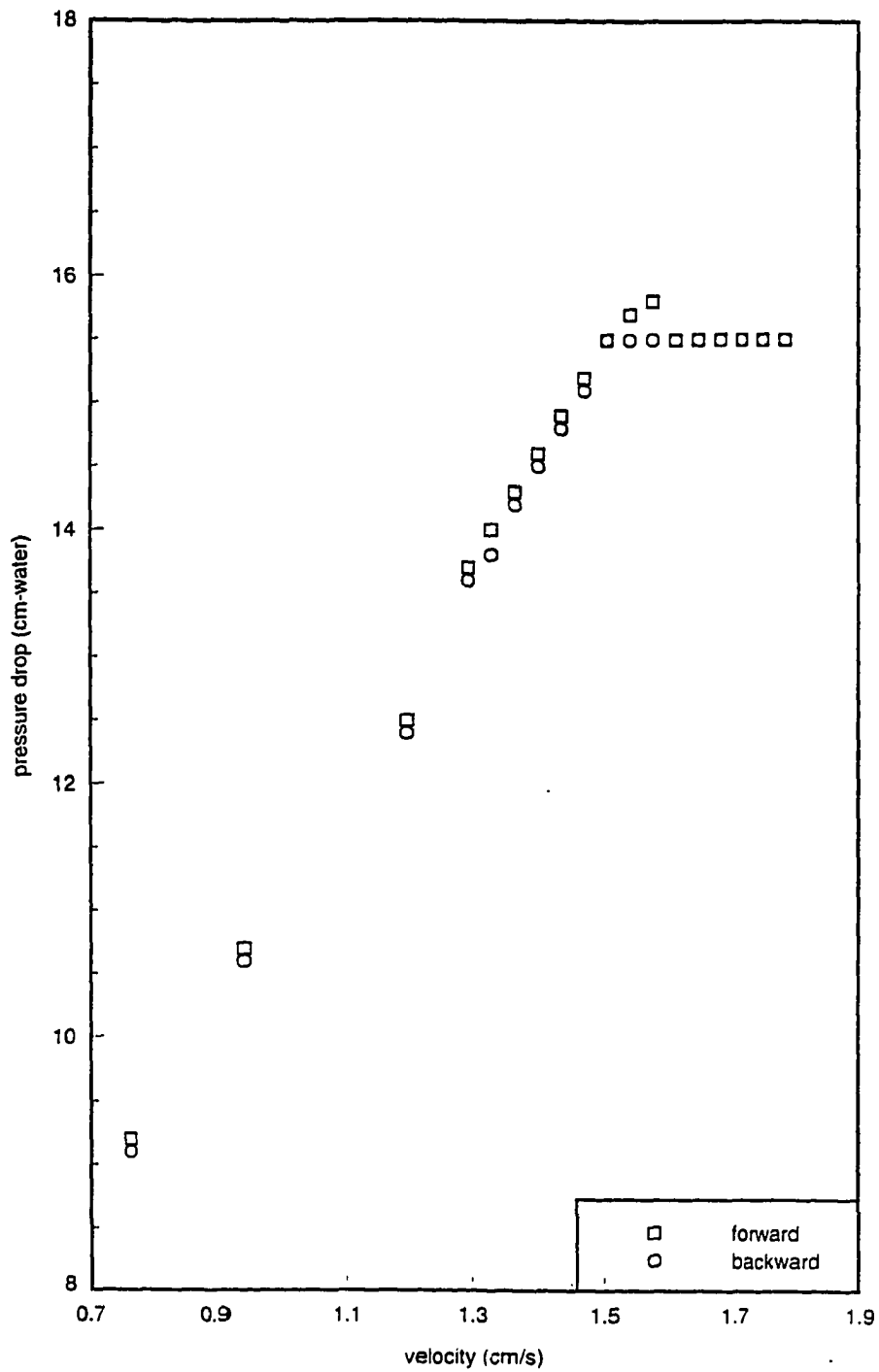
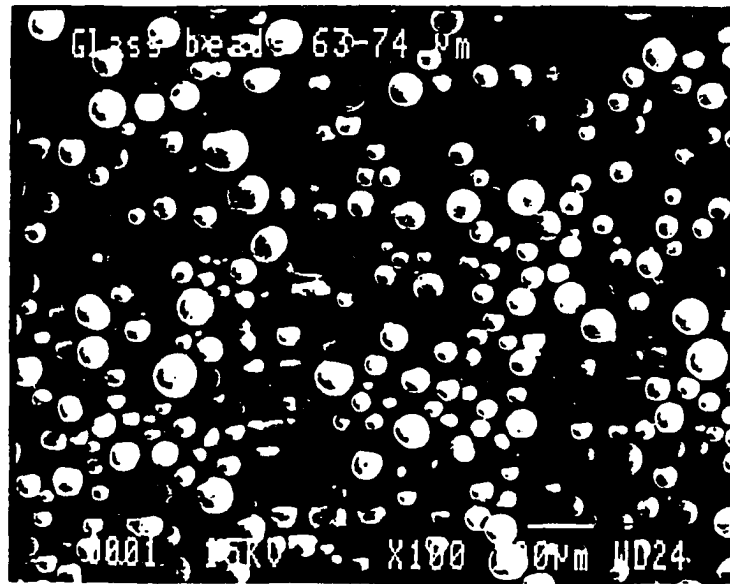
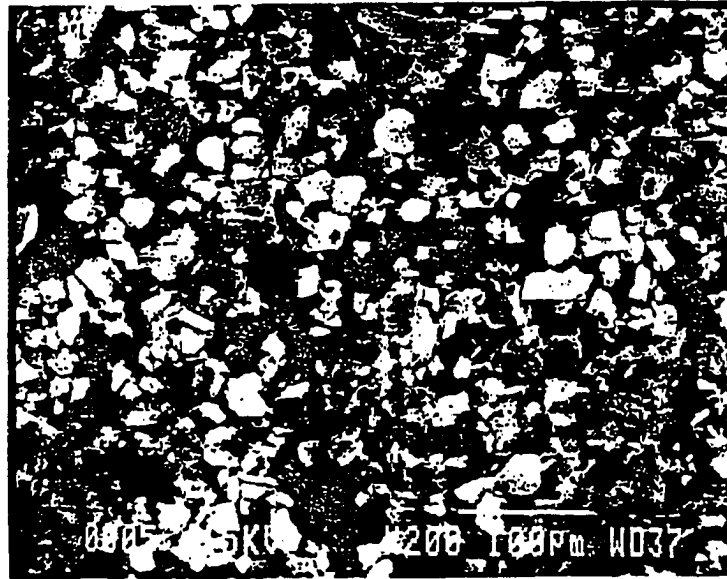


Figure D.1 U vs. pressure drop of the fluidized bed for determining the U_{mf}

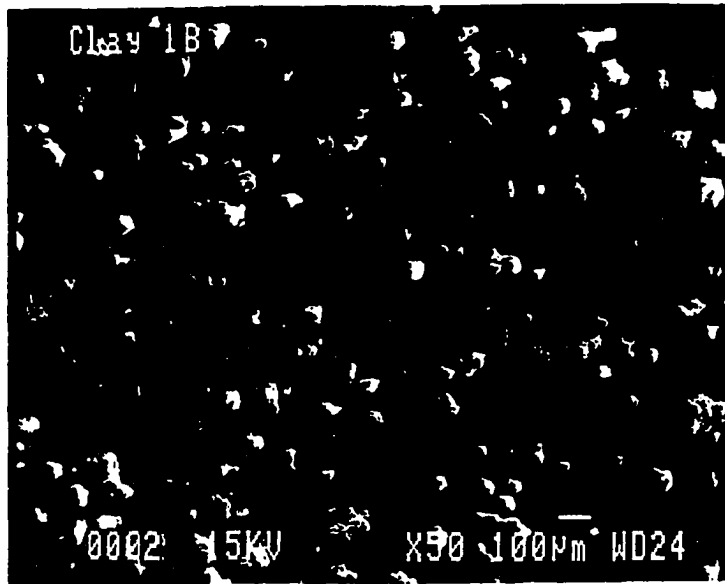


(a)

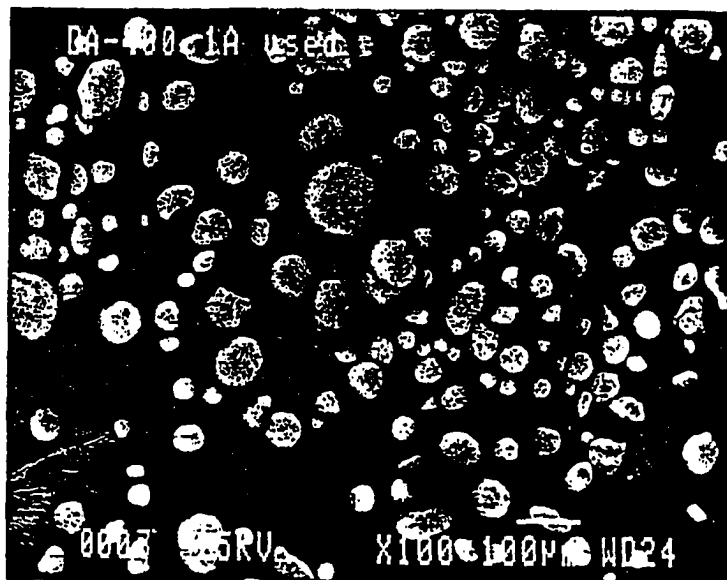


(b)

Figure D.2 (a). Picture of glass beads (marked as 63-74 μ m) taken from SEM, Kevex, automated image analyzer, x100 (b). Picture of sand fines, x200

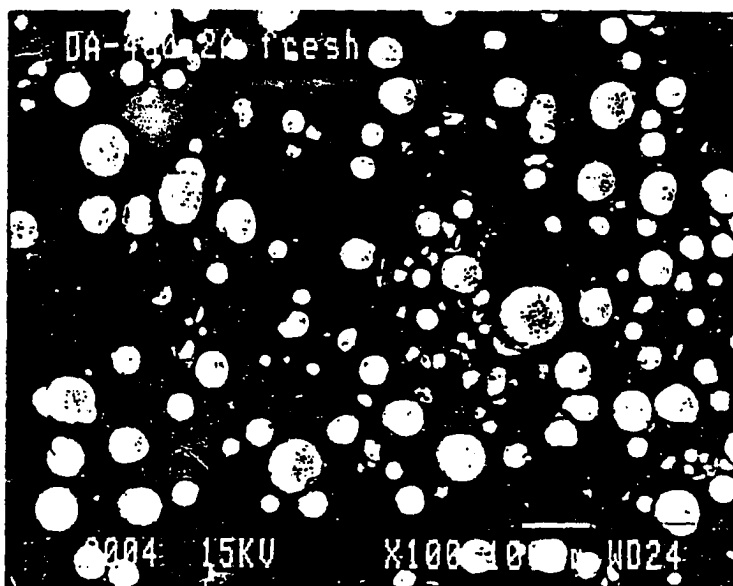


(a)



(b)

Figure D.3 (a). Picture of FCC 1-B (Kaolin clay) taken from SEM, Kevex, automated image analyzer, x50 (b). Picture of FCC 1-A (Zeolitic, spent), x100



(a)



(b)

Figure D.4 (a). Picture of FCC 2-A (Zeolitic, fresh) taken from SEM, Kevex, automated image analyzer, x100 (b). Picture of FCC 3-A (aluminum oxide) x500

APPENDIX E: CALIBRATION OF ROTAMETERS

A Wet Test Meter (GCA Precision Scientific Co.) and a stop watch were used to calibrate the rotameters.

The calibration of various rotameters used during the test are shown the following Figures. Figs.E.1, E.2, and E.3 showed the Gilmont rotameter SA1, SA2, and SA3 with three different gases (Air, N₂, and AR), respectively. Figs.E.4 and E.5 show the rotameter Lab-crest 450-700 and Devco with air and N₂, respectively. Fig.E.6 shows the calibration of CO₂ with the SA3 rotameter.

The pressure drop across the distributor is shown in Figs.E.7, E.8, E.9, and E.10 for N₂, CO₂, Air, and Ar, respectively. The pressure across the rotameter SA3 for various gases is given in Fig.E.11.

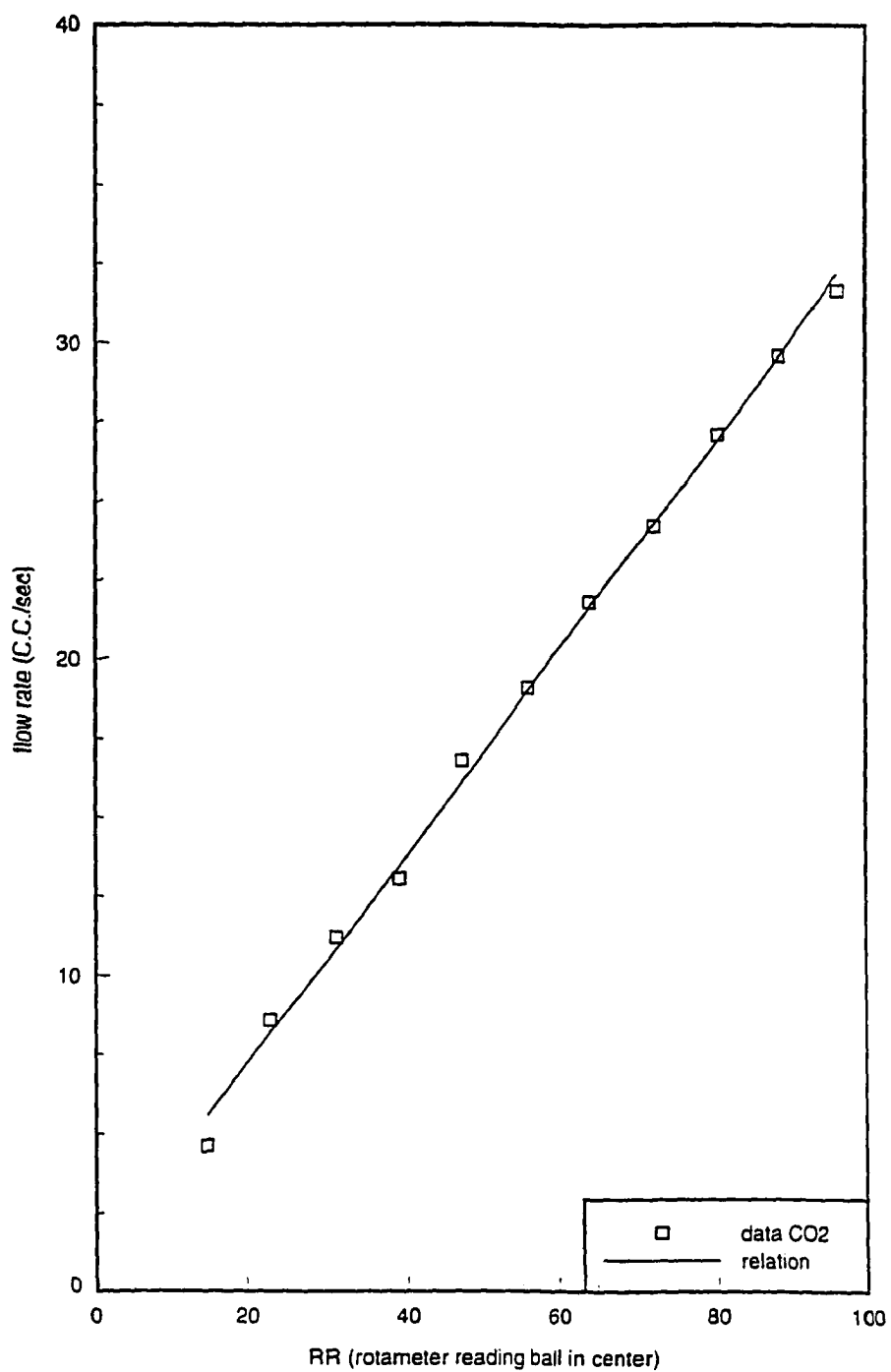


Figure E.1 Calibration of rotameter SA1 with Air, N₂, and CO₂

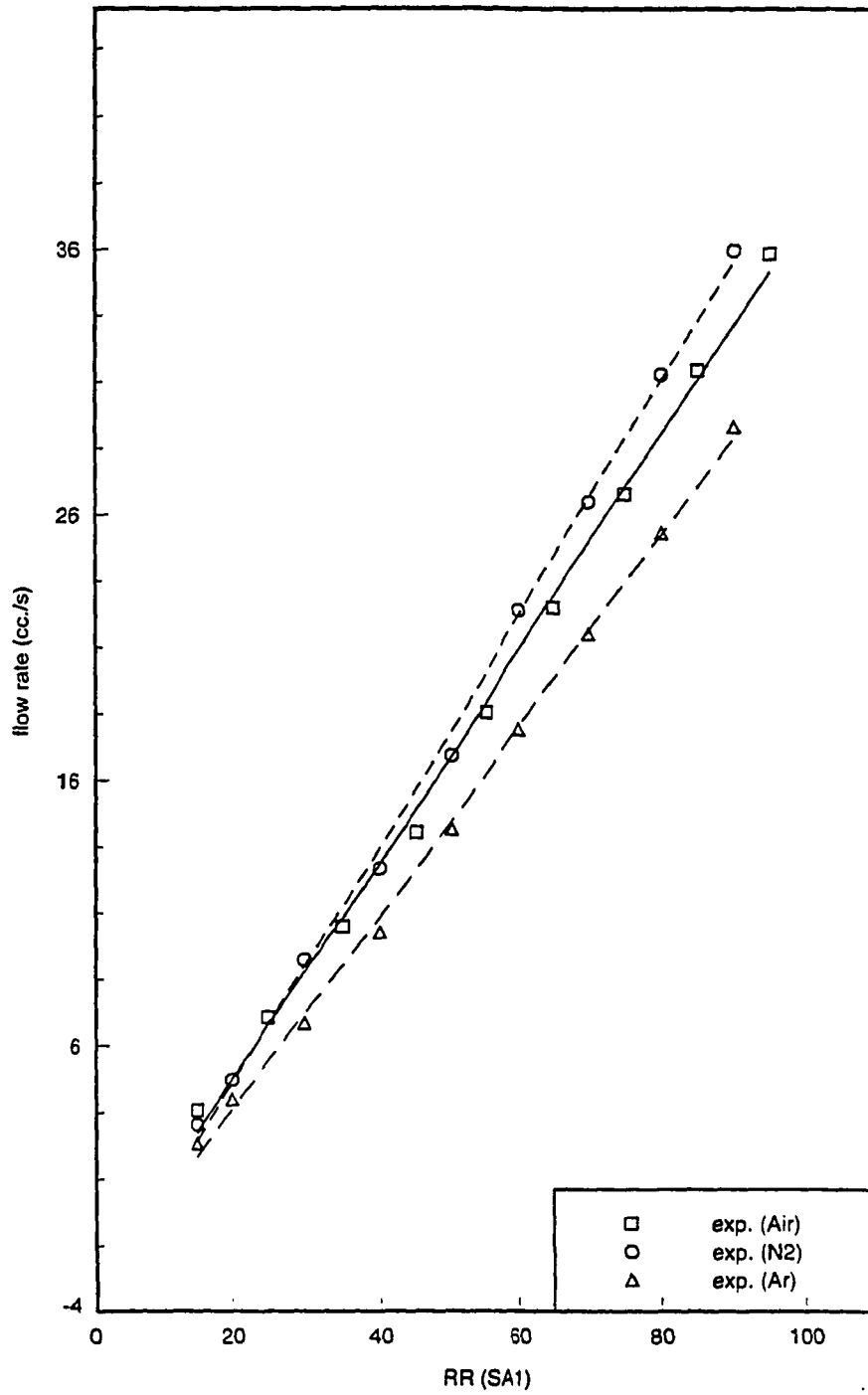


Figure E.2 Calibration of rotameter SA2 with Air, N₂, and CO₂

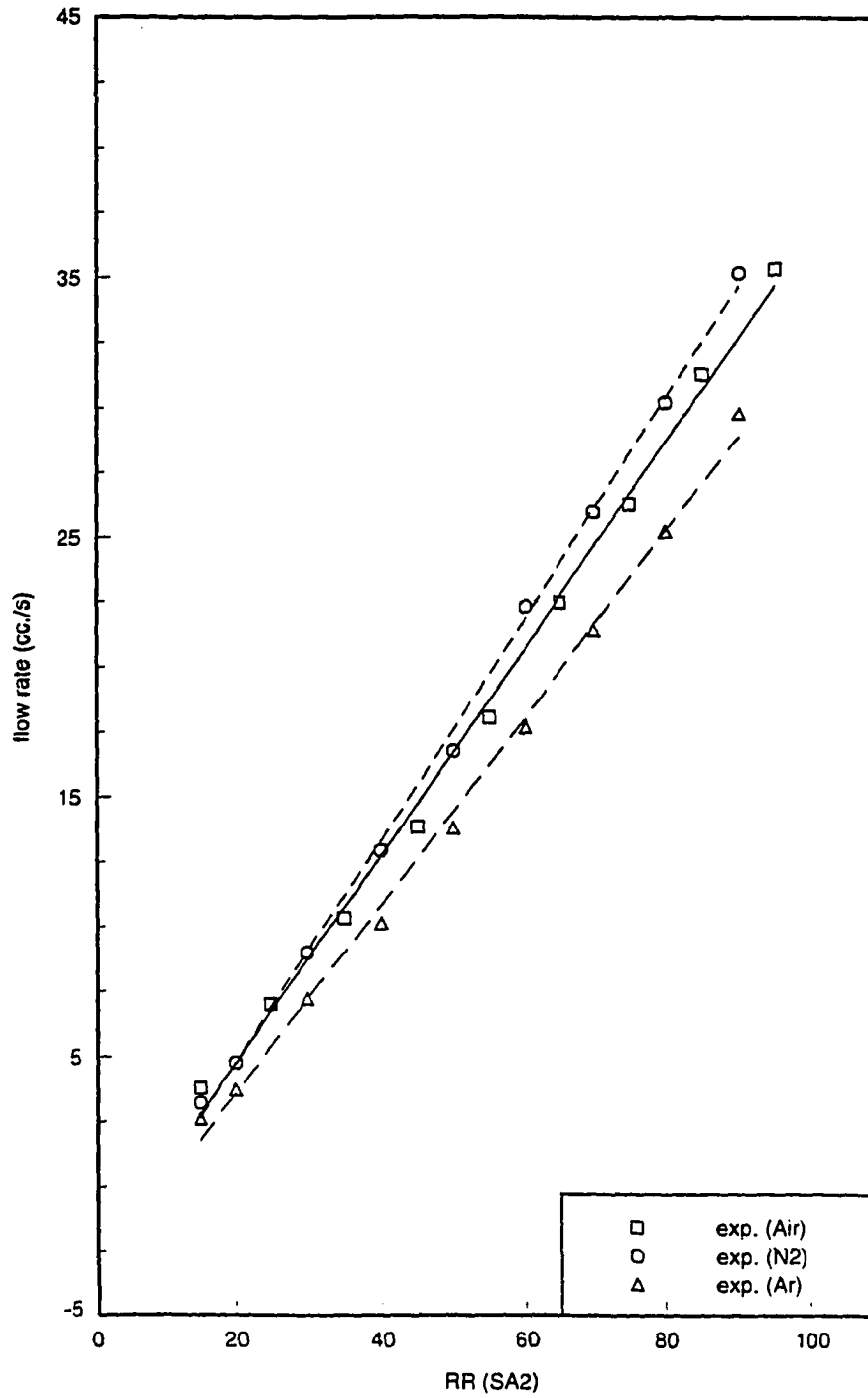


Figure E.3 Calibration of rotameter SA3 with Air, N₂, and CO₂

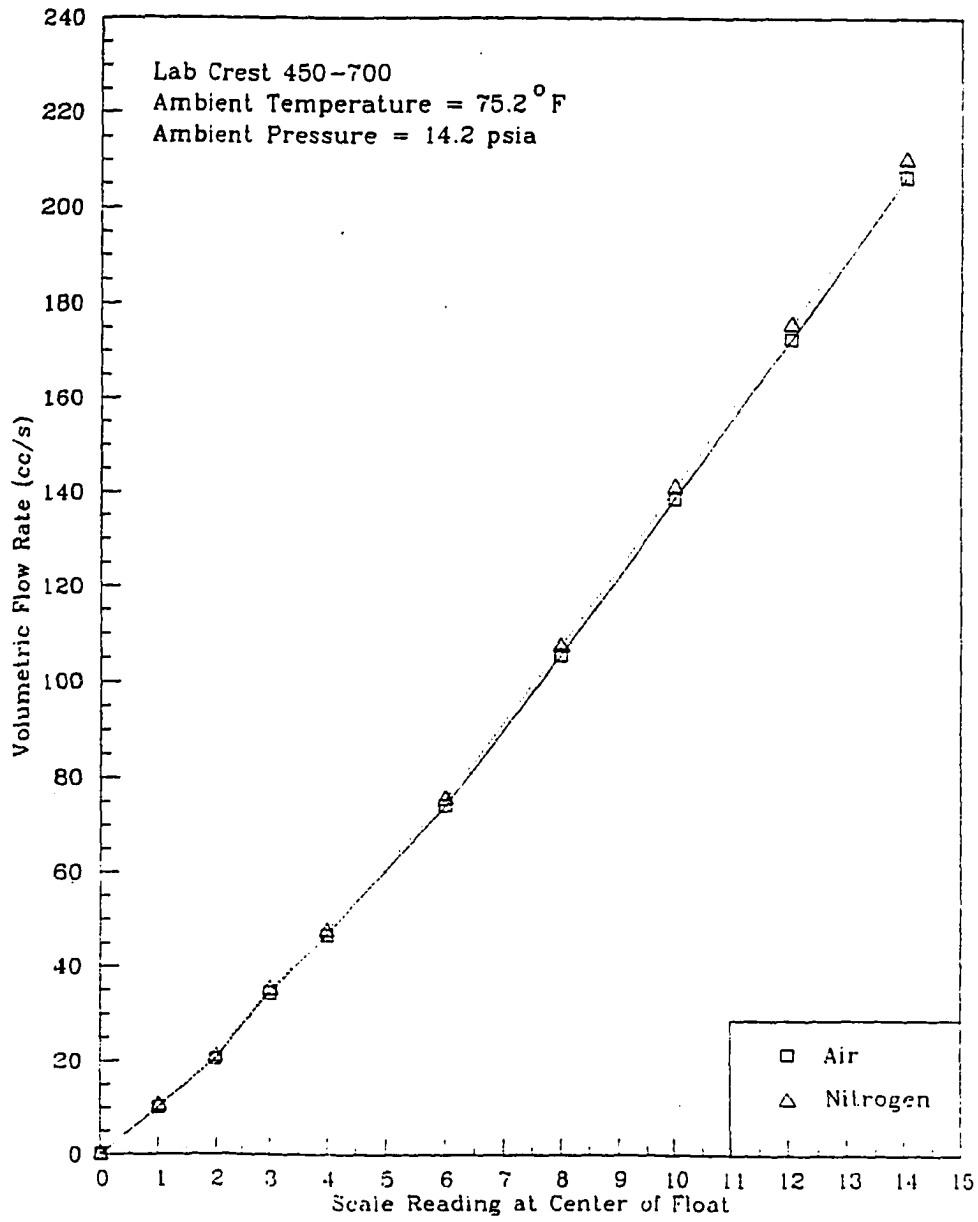


Figure E.4 Calibration of rotameter LabCrest 450-700 with Air

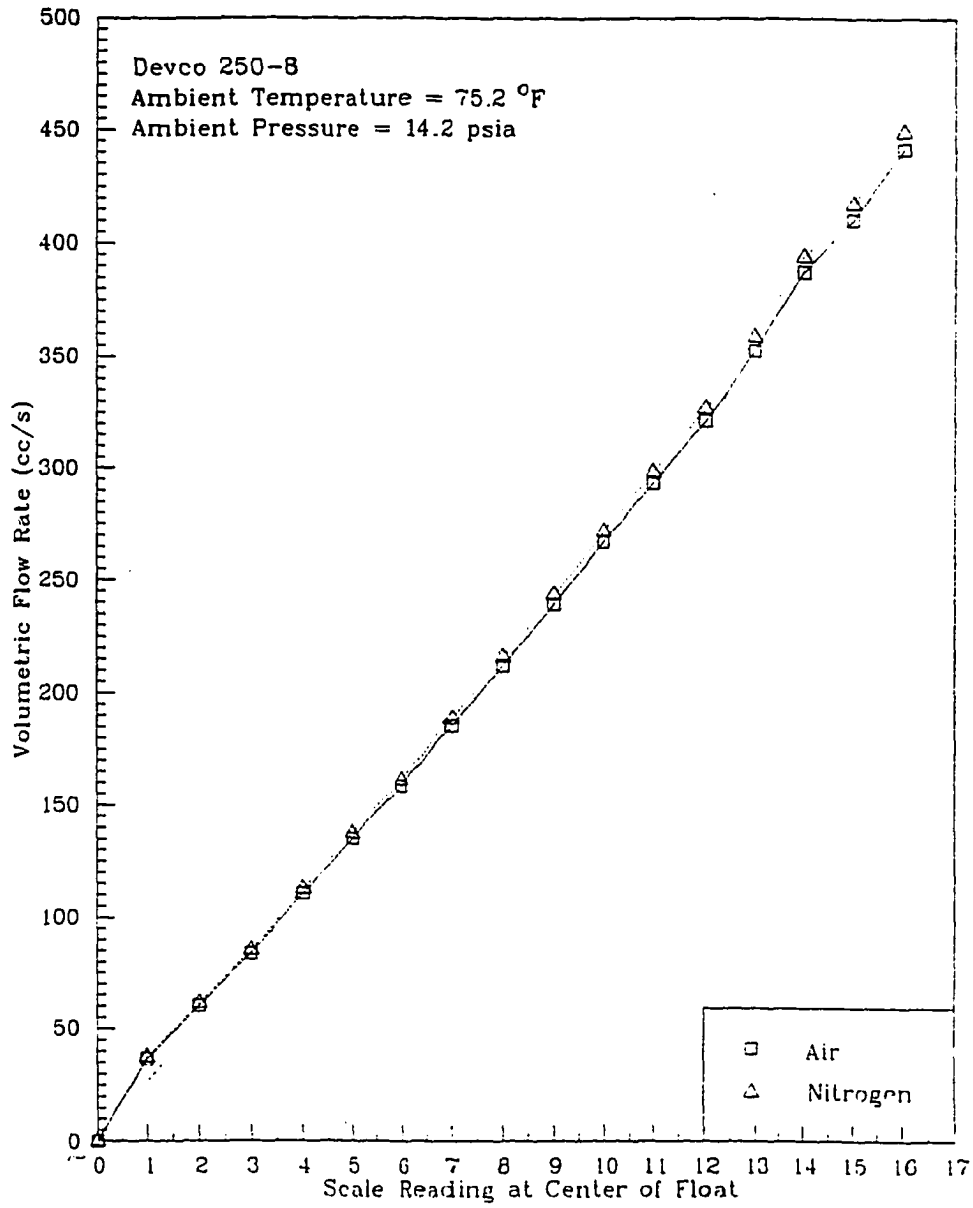


Figure E.5 Calibration of rotameter Devco 250-8 with Air

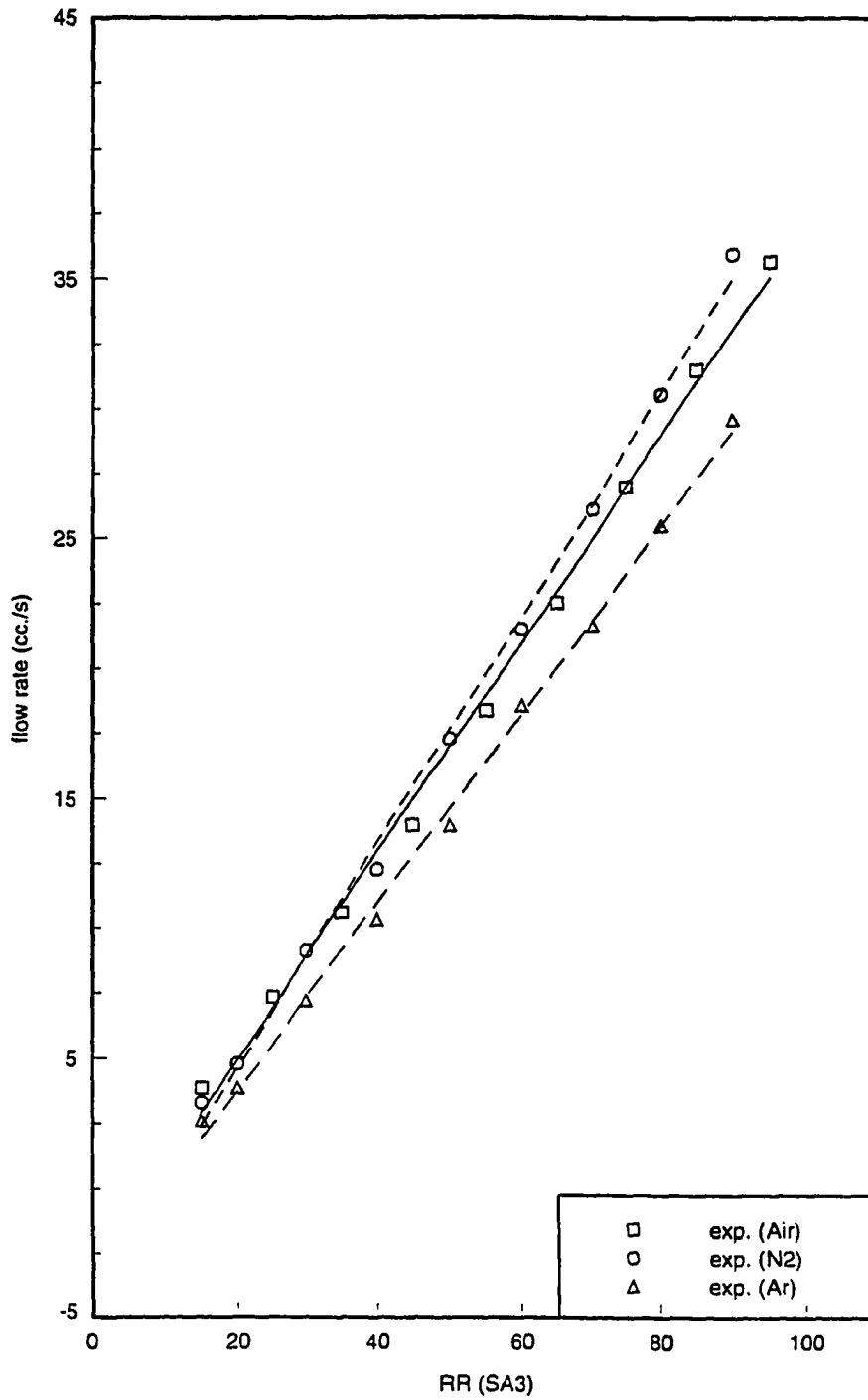


Figure E.6 Calibration of rotameter SA3
with CO₂

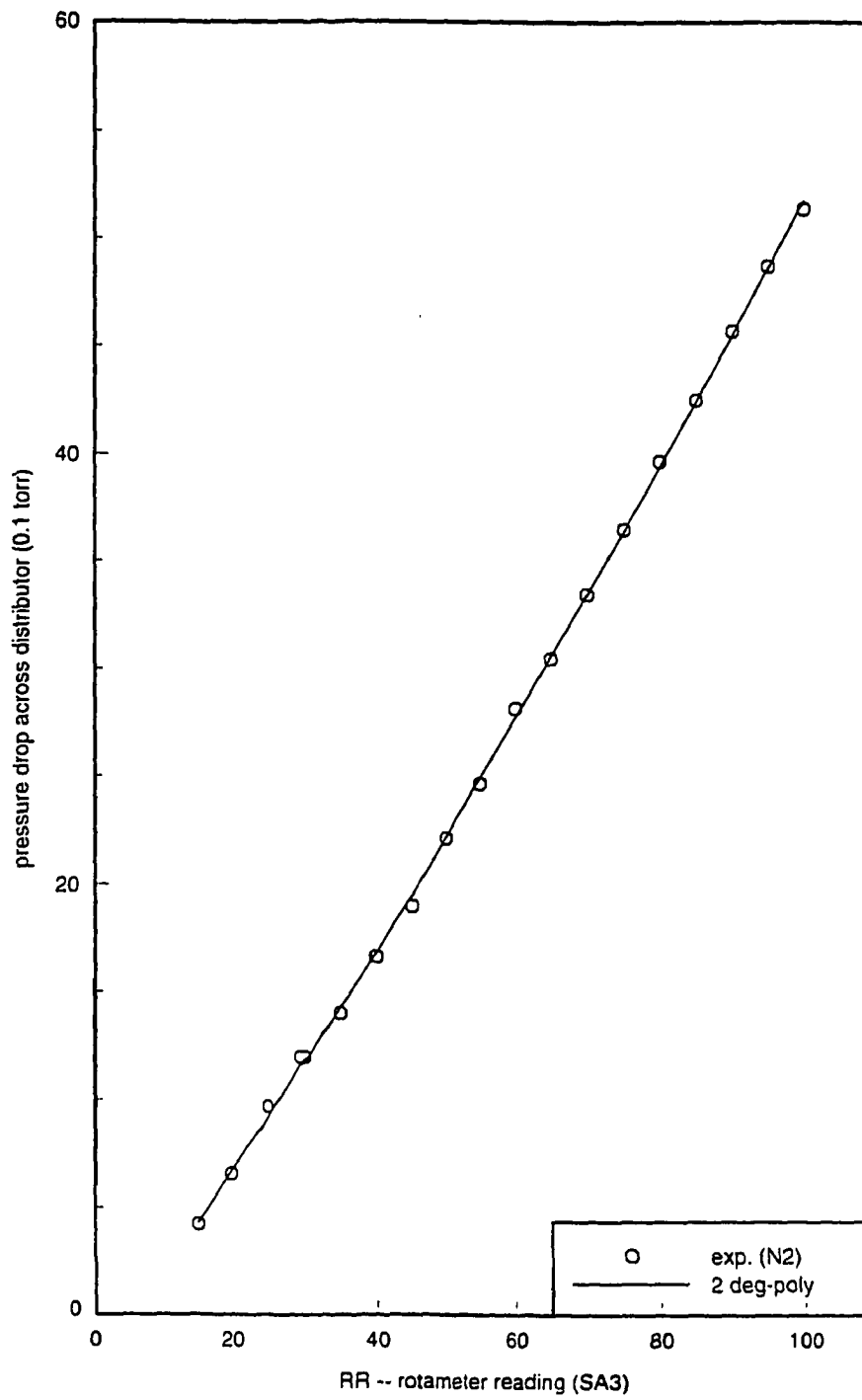


Figure E.7 Pressure drop across distributor
for N₂ at 24 °C, 1 atm

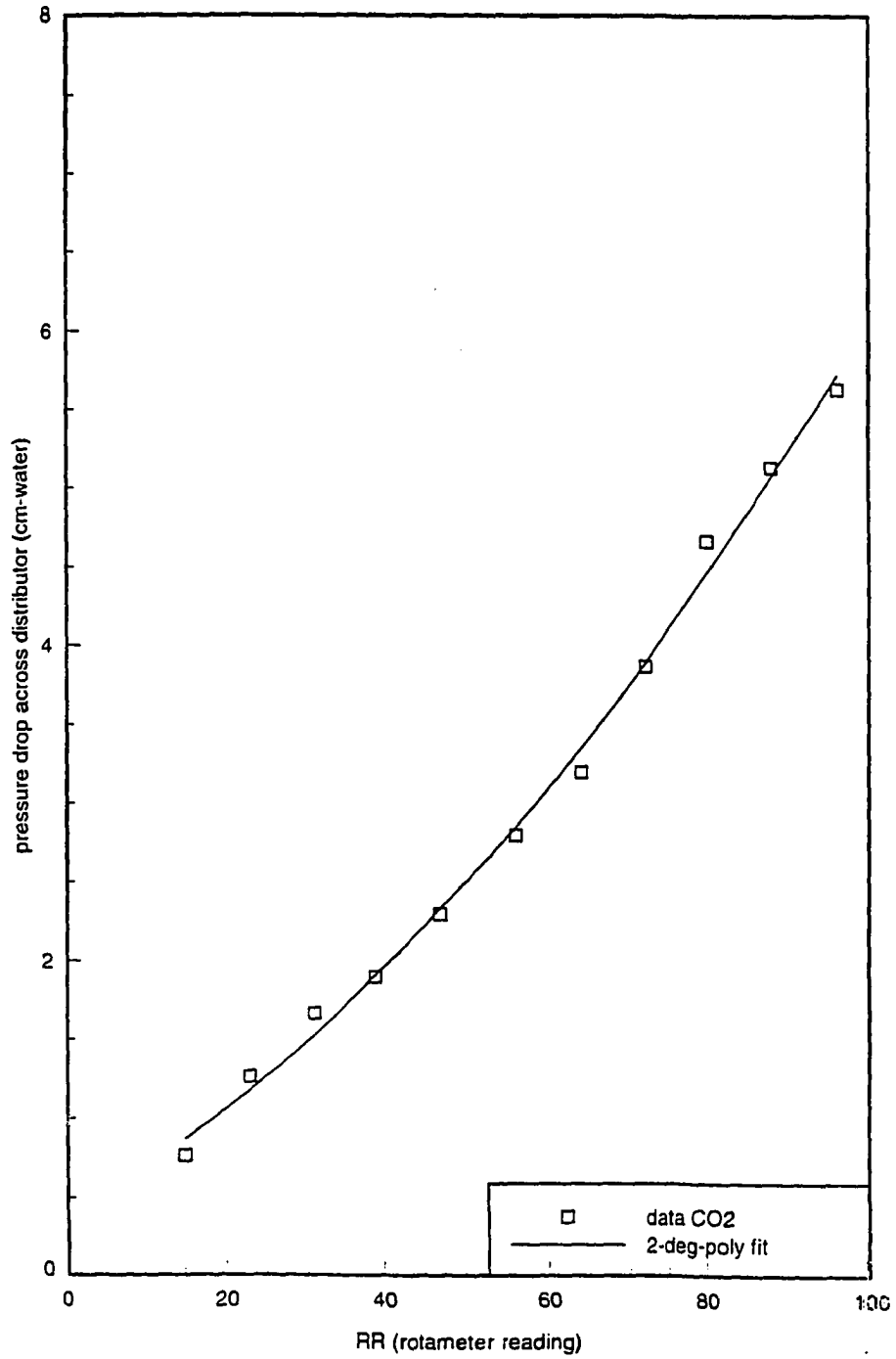


Figure E.8 Pressure drop across distributor
for CO₂ at 24 °C, 1 atm

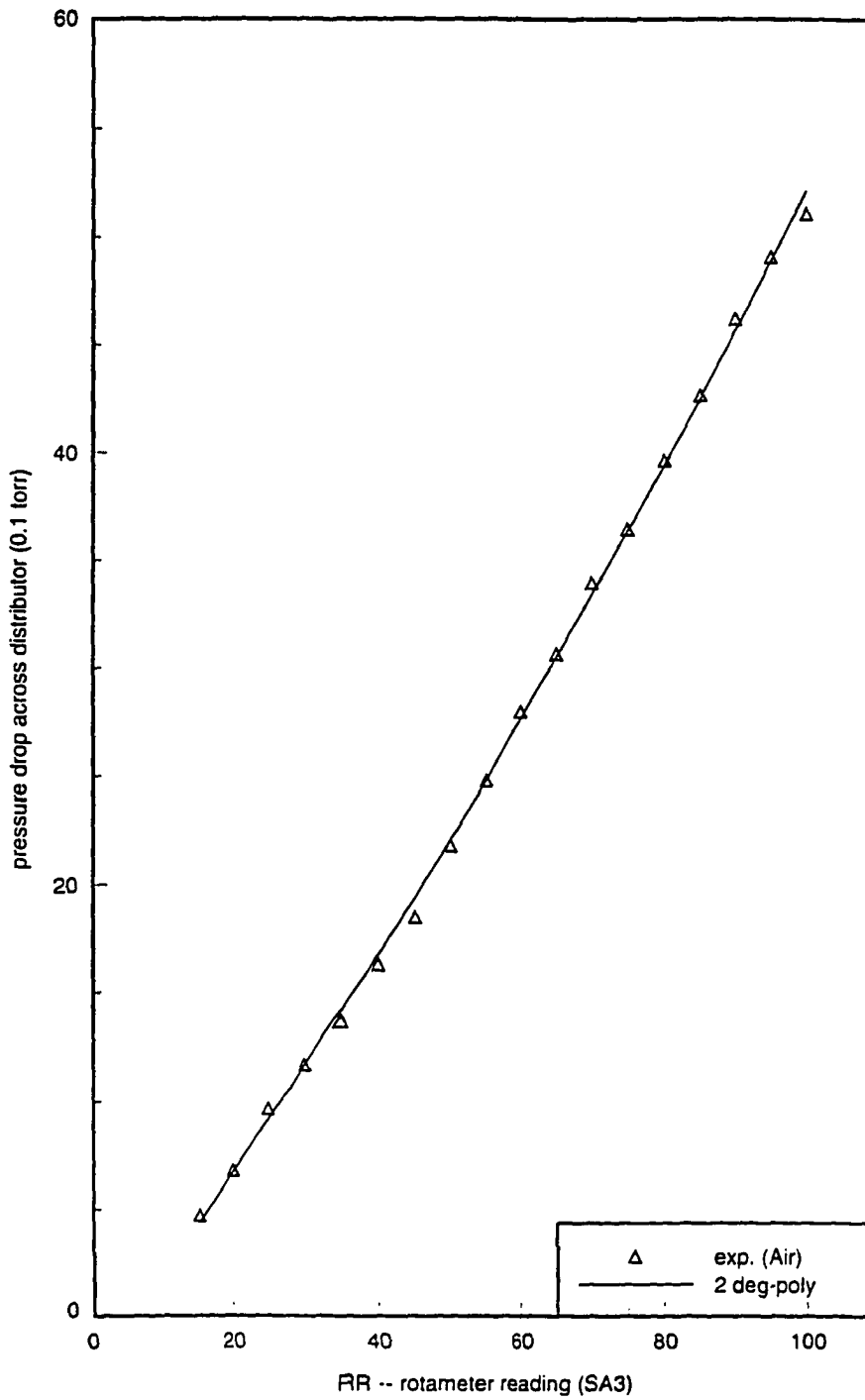


Figure E.9 Pressure drop across distributor
for Air at 24 °C, 1 atm

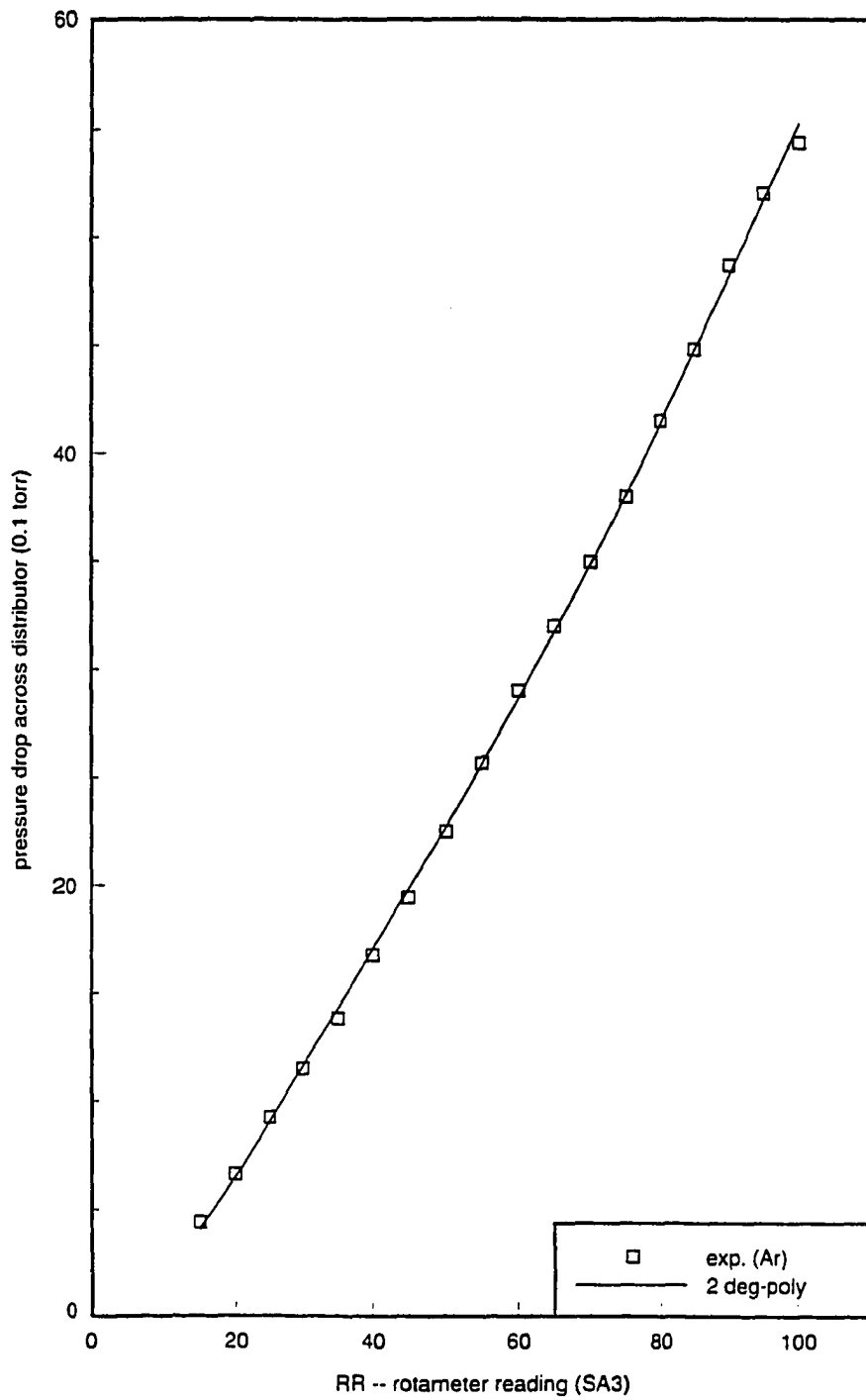


Figure E.10 Pressure drop across distributor
for Ar at 24 °C, 1 atm

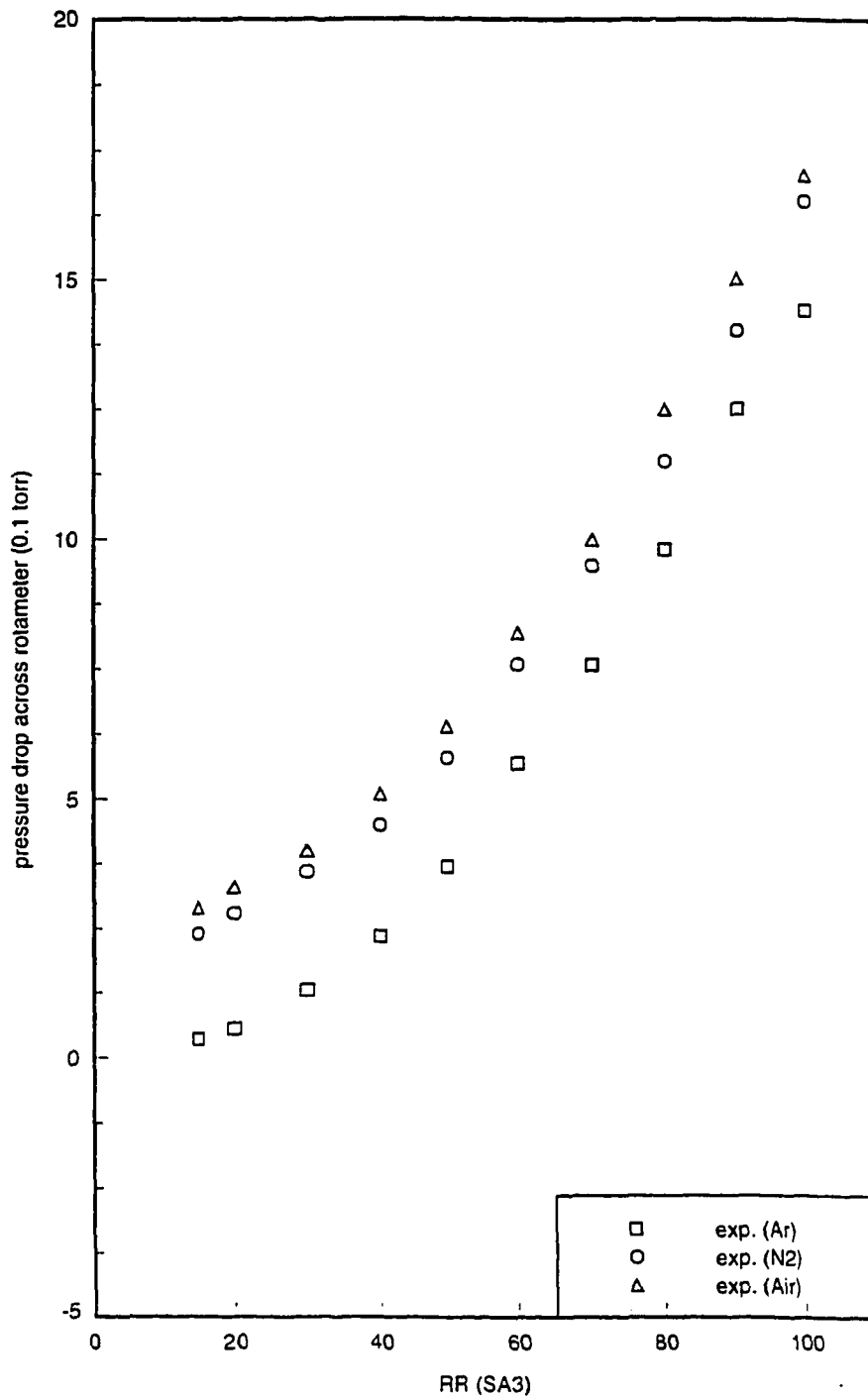


Figure E.11 Pressure drop across rotameter SA3 for various gases at 24 °C, 1 atm

APPENDIX F: PROGRAM AND EXAMPLE DATA

The program for the data acquisition was written with BASIC language. It was used for taking laser intensity reading and charge reading (voltage came from Keithley Electrometer). The program and an example data set are shown in below:

Program: ' This is a program for data acquisition system in particle elutriation measurement

```

=====
device$= "dvm"
call ibfind(device$, dvm%)
device$= "scanner"
call ibfind(device$, scanner%)
call ibclr(dvm%)
call ibclr(scanner%)
call ibwrt(dvm%, "f1 r1 t1 z0")
call ibwrt(scanner%, "com 1")
call ibwrt(scanner%, "slist 100, 101")
open "A:\elut01.dat" for output as #1
cls
print ; "reading      V1      V2      time"
time$= "00:00:00"

' wait for three second to start the sampling pocedure
for k=1 to 60000
next k

' begin sampling the data
for I=1 to 100
  call ibwrt(dvm%)
  vone$= space$(13)
  call ibrd(dvm%, vone$)
  V1#= val(vone$)
  call ibwrt(scanner%, "step")
  call ibtrg(dvm%)
  vtwo$= space$(13)
  call ibrd(dvm%, vtwo$)
  V2#= val(vtwo$)
  t#= timer

```

```
print using "###.##### ": I: V1#. V2#, t#
print #1, using "###.##### ": I: V1#: V2#: t#
```

```
wait for one second
  for j=1 to 50000
  next j
next I
close #1
end
```

example data:

No. data	accumulated charge	laser reading	time (s)	No. data	accumulated charge	laser reading	time (s)
1	0.010302	0.357697	3.46	47	0.030648	0.510411	104.63
2	0.00985	0.263828	5.6	48	0.030578	0.511919	106.83
3	0.00979	0.299848	7.79	49	0.030585	0.508699	109.02
4	0.01009	0.307189	9.99	50	-0.000181	0.513391	111.22
5	0.010178	0.335114	12.19	51	-0.000153	0.511682	113.42
6	0.010244	0.389331	14.39	52	-0.000136	0.515292	115.61
7	0.010664	0.421785	16.58	53	-0.000134	0.517171	117.87
8	0.011211	0.419627	18.78	54	-0.000136	0.515437	120.06
9	0.011802	0.438258	20.98	55	-0.000134	0.513463	122.26
10	0.012489	0.457068	23.17	56	-0.000145	0.510165	124.46
11	0.013137	0.456511	25.37	57	-0.000126	0.511547	126.65
12	0.01379	0.464253	27.57	58	-0.000154	0.514214	128.85
13	0.014485	0.467773	29.76	59	-0.000195	0.516517	131.05
14	0.015067	0.46675	31.96	60	-0.000211	0.516084	133.24
15	0.015656	0.466516	34.16	61	-0.000225	0.514969	135.44
16	0.016314	0.477876	36.36	62	-0.000172	0.517249	137.64
17	0.01691	0.488715	38.55	63	-0.000162	0.512496	139.89
18	0.017452	0.493924	40.75	64	-0.00014	0.51645	142.09
19	0.018112	0.491603	42.95	65	-0.000161	0.510186	144.28
20	0.018773	0.493508	45.14	66	-0.000127	0.51451	146.48
21	0.0194	0.497178	47.34	67	-0.000182	0.514094	148.68
22	0.020167	0.498594	49.59	68	-0.0002	0.516709	150.88
23	0.020804	0.498196	51.79	69	-0.000149	0.516744	153.07
24	0.021365	0.503658	53.99	70	-0.000185	0.515869	155.27
25	0.022098	0.502153	56.18	71	-0.000193	0.512003	157.47
26	0.022798	0.503496	58.38	72	-0.000173	0.518107	159.66
27	0.023512	0.503151	60.58	73	-0.000199	0.516443	161.92
28	0.024176	0.505683	62.77	74	-0.000196	0.518279	164.11
29	0.024876	0.503523	64.97	75	-0.000176	0.517715	166.31
30	0.025644	0.503825	67.17	76	-0.000185	0.517997	168.51
31	0.026294	0.501063	69.37	77	-0.000178	0.51724	170.7
32	0.02693	0.503019	71.62	78	-0.000191	0.519748	172.9
33	0.027541	0.500948	73.81	79	-0.000168	0.520725	175.1
34	0.027954	0.504564	76.01	80	-0.000191	0.518907	177.29
35	0.028152	0.507858	78.21	81	-0.00018	0.515309	179.49
36	0.028378	0.504854	80.41	82	-0.000158	0.518392	181.69
37	0.028797	0.506542	82.6	83	-0.000172	0.516541	183.94
38	0.028919	0.509106	84.8	84	-0.000172	0.515758	186.14
39	0.029137	0.508942	87	85	-0.000137	0.521407	188.33
40	0.029332	0.512387	89.19	86	-0.000184	0.525849	190.53
41	0.029461	0.510461	91.39	87	-0.000173	0.527385	192.73
42	0.029691	0.511761	93.64	88	-0.00012	0.526446	194.93
43	0.029773	0.510211	95.84	89	-0.000148	0.526711	197.12
44	0.029931	0.508555	98.04	90	-0.000159	0.526813	199.32
45	0.03007	0.507585	100.23	91	-0.000192	0.526704	201.52
46	0.030614	0.507298	102.43	92	-0.000179	0.526196	203.71